Efficient Algorithms for Three-Dimensional Near-Field Synthetic Aperture Radar Imaging

PhD Dissertation from

Faculty of Electrical Engineering
University of Karslruhe, Germany

by

Joaquim Fortuny

Efficient Algorithms for Three-Dimensional Near-Field Synthetic Aperture Radar Imaging

Zur Erlangung des akademischen Grades eines

DOKTOR-INGENIEURS

von der Fakultät für
Elektrotechnik
der Universität Karlsruhe

genehmigte

DISSERTATION

von

ING. JOAQUIM FORTUNY
aus Tarragona (Spanien)

Preface

This Thesis arises from the work done at the European Microwave Signature Laboratory (EMSL), a large scale facility of the Directorate General Joint Research Center (JRC) of the European Commission (EC) located in Ispra, Northern Italy. The whole project started when two members of the EMSL Advisory Committee (Prof. Dr.-Ing. Werner Wiesbeck, Director of the Institute for Microwaves and Electronics, Karlsruhe University, Germany, and Prof. Dr.-Ing. Martti Hallikainen, Head of the Laboratory of Space Technology, Helsinki University of Technology, Finland) encouraged me to initiate this PhD Thesis.

Foremost I want to express my gratitude to my supervisor, Prof. Dr.-Ing. Werner Wiesbeck, who offered me the opportunity to defend this Thesis at his faculty. His continuous assistance and encouragement has been crucial to the successful completion of this work. I also thank the Board of the Faculty of Electrical Engineering, Karlsruhe University, for allowing me to write and defend this Thesis in English.

I should also express my thanks to Prof. Dr.-Ing. Martti Hallikainen, for critically reviewing this work, and for the many constructive comments.

Sincere thanks in particular are due to my unit head at JRC, Dr. Alois Sieber, for his active involvement and guidance throughout this project.

A very special mentioning is reserved for Dr.-Ing. Juan-Manuel López-Sánchez, Alicante University, Spain, for his friendship, in the first instance, and then for the significant contribution given to the development of the imaging techniques presented in Chapter 3.

I am deeply grateful to all my colleagues in the Humanitarian Security Unit at JRC for the successful preparation of the radar experiments presented in this Thesis. In particular, I want to thank Dott. Giuseppe Nesti and Dipl.-Ing. Eggert Ohlmer for the continuous support and excellent advise. Special thanks are due to Dott. Dario Tarchi and Dott. Ing. Davide Leva for the preparation of the experiment with the ground based SAR system of the unit. I am very grateful to Elena di Gioia, secretary of the Humanitarian Security Unit, for her constant assistance. Yet, I want to thank Dr. Gareth Lewis for the proofreading of the Thesis.

I want to express my gratitude to Dr.-Ing. Hans Rudolf and Dipl.-Ing. Björn Dietrich for their help, encouragement and friendship.

Sincere thanks are due to Dipl.-Ing. Christian Fischer from the Institut for Microwaves and Electronics at Karlsruhe University for his continual assistance during my series of visits to Karlsruhe.

Finally, I would also like to thank my parents for their sacrifice, encouragement, and support throughout my studies. Last but not least, since this was an effort mostly allocated outside the normal working hours at JRC and during my holidays, I thank my wife, María José, and my children, Carlos and Marta, for their inspiration, encouragement and endless patience.

Executive Summary

The availability of indoor three-dimensional (3-D) synthetic aperture radar (SAR) systems operating in a controlled environment offers a unique opportunity to define optimally the operational parameters (e.g., the frequency, the polarization and the viewing geometry) of future SAR systems for a given application. The scanning geometries commonly used with indoor 3-D SAR systems are planar, cylindrical, and spherical. For these scanning geometries, a set of efficient near-field algorithms especially suited for these systems is presently missing.

In this thesis, a set of five 3-D near-field imaging algorithms is introduced, each satisfying different requirements in terms of computational cost, quality of the resulting imagery, type of the scanning geometry, and implementation complexity. These algorithms are all tested by means of numerical simulations and, most important, radar measurements in the European Microwave Signature Laboratory (EMSL).

At first, a novel 3-D near-field radar imaging technique based on the range migration algorithm (RMA), which requires frequency domain backscatter data acquired on a two-dimensional (2-D) planar aperture, is presented. The formulation of this algorithm is derived by using the method of stationary phase (MSP). The 3-D RMA cannot be directly applied with cylindrical and spherical scanning geometries. For these scanning geometries, a new imaging algorithm based on the backpropagation of the backscattered data onto a planar aperture followed by the 3-D RMA is introduced.

The use of the proposed backpropagation technique with targets electrically very large is computationally costly. Two alternative solutions are suggested. First, a space-variant matched filter imaging algorithm especially tailored for spherical scanning geometries, which accounts precisely for the wavefront curvature and the free space propagation loss. Second, a polar format algorithm (PFA) with an image rectification. This solution allows the use of FFT-based focusing algorithms normally used under the far-field condition. The resulting geometric distortion due to the short observation distance is successfully corrected by applying a rectification algorithm.

Finally, a subsurface sensing algorithm that corrects for the effects of refraction and dispersion is outlined. This imaging algorithm is especially tailored for a forward-looking stand-off platform. In addition, a simple and effective characterization technique is used to retrieve the dielectric permittivity of the medium surrounding the subsurface objects.

List of Acronyms

1-D:	One-Dimensional
2-D:	Two-Dimensional
3-D:	Three-Dimensional
APL:	Anti-Personnel Landmine
CCRS:	Canada Centre for Remote Sensing
CW:	Continuous Wave
dBsm:	dB Square Meter
DFT:	Discrete Fourier Transform
EC:	European Commission
EMSL:	European Microwave Signature Laboratory
FFT:	Fast Fourier Transform
FT:	Fourier Transform
GPR:	Ground Penetrating Radar
HF:	High Frequency
HSU:	Humanitarian Security Unit
IFFT:	Inverse Fast Fourier Transform
IPSC:	Institute for the Protection and Security of the Citizen
ISAR:	Inverse Synthetic Aperture Radar
JRC:	Directorate General Joint Research Centre
LISA:	Linear SAR System
MF:	Matched Filter
MSP:	Method of the Stationary Phase
NF:	Near Field
PFA:	Polar Format Algorithm
PFA-IR:	Polar Format Algorithm with Image Rectification
RCS:	Radar Cross Section
RF:	Radio Frequency
RMA:	Range Migration Algorithm
RMA-FReD:	Frequency Domain Replication and Down-Sampling
RMA-FT:	Range Migration Algorithm with Fields Translation
SAFT:	Synthetic Aperture Focusing Technique
SAR:	Synthetic Aperture Radar

SNR:	Signal to Noise Ratio
SVMFIA:	Space-Variant Matched Filter Imaging Algorithm
SVMF-SSA:	A Space-Variant Matched Filter Subsurface Sensing
Tx/Rx:	Transmit/Receive
UXO:	Unexploded Ordnance
VNA:	Vector Network Analyzer

Contents

List of Figures

List of Tables

Introduction

1.1 Background

The formation of synthetic aperture radar (SAR) images was first accomplished by analog optical processing in the early 1960's at the Willow Run Laboratories [1, 2]. This effort was part of a study concerned with the fine resolution imaging of rotating objects sponsored by the US Air Force. The SAR data required formatting and photographic recording to produce the appropriate input to the optical processor. Digital computers were not used because of their inadequateness to handle the quantity of data and the required computational load.

The first coherent ground-based radar was built in the late 1970's under the US Army sponsorship. Within the framework of this project, Walker [3] designed an experimental setup to simulate an airborne radar flying around a stationary ground patch. This was the first attempt to characterize the requirements for optically processing coherent radar data collected from targets placed on a rotating platform. Contemporaneously, Bojarski [4] showed theoretically that coherent multi-aspect monostatic or bistatic measurements of the far field scattered by a non-dispersive object, as a function of the frequency, can be used to reconstruct a three-dimensional (3-D) reflectivity image. A group led by Mensa [5] at the Pacific Missile Test Center and Wehner [6] at the Naval Ocean Systems Center worked extensively on the radar imaging of rotating objects, as did Chen [7] and Ausherman [8]. A group under Farhat [9, 10] formed the first 3-D radar images of a complex shaped target from actual microwave scattering data. Mensa [11, 12] and Munson [13] analyzed the relation between techniques used in classical tomography and range-Doppler imaging. Some years later, this analysis was further developed by Jakowatz [14, 15] and Lawton [16]. The establishment of this relation greatly boosted the development of the radar processing techniques presently in use [17].

In the late 1980's, a group led by Rocca [18, 19, 20] at the Politecnico di Milano (Italy) introduced the use of the wave equation formulation in SAR, applying the method of wave backpropagation in seismic data processing [21]. This result represented a breakthrough in the field of SAR because of the low computationally cost and the superb image reconstructions produced. Furthermore, as opposed to the classical range-Doppler focusing algorithms used at that time, this technique incorporated the wavefront curvature into the imaging model [22, 23, 24].

Recently, the development of SAR systems providing full 3-D capability (e.g., a multibaseline interferometric or tomographic SAR) has become a field of intensive research [25]. A great extent of the experimental work in this area has been carried out using SAR facilities operating in a controlled environment. Examples of SAR facilities operating in a controlled environment can be found in France [26], Sweeden [27], the US [28, 29, 30, 31, 32, 33], Belgium [34], Spain [35], the UK [36], and Germany [37, 38]. Near-field radar cross section (RCS) measurements have also been used to obtain the far-field scattering signature of targets [39, 40, 41].

One of the latest developments in the field of near-field radar imaging is the use of fast multi-level domain decomposition algorithms [42, 43]. These algorithms were previously exploited in complex integral-equation solvers. Moreover, it is worth mentioning the recent formulation of tomographic imaging in its full vector form by Langenberg [44, 45, 46]. This technique has been successfully proven both in SAR and ultrasonics. Finally, the recent work by Smith [47] assessing the role that the evanescent electromagnetic waves can play in the detection and identification of a buried object deserves special attention.

Today, SAR has become a well developed technique for producing high resolution images [48, 49, 50]. According to their working principle the existing radar imaging algorithms can be divided into four general groups:

Polar Format Algorithm: (also known as range-Doppler algorithm) This algorithm was the first one to be developed and originates from optical signal processing. It is based on the polar nature of the frequency domain backscatter data, works with motion compensation to a point and as such needs to be used under the far field condition, requires an interpolation prior to the Fourier transform, and compensates only partially the range curvature. Both the 2-D and 3-D versions of this algorithm are easy to implement and have been used extensively.

Range Migration Algorithm: (in its 2-D version it is also known as $\omega - k$ algorithm [19]) This algorithm originates from geophysics. It works with motion compensation to

a line, requires a 1-D interpolation (known as Stolt interpolation [21]) and compensates completely the curvature of the wavefront. To date, in the radar remote sensing domain, it has only been used in its 2-D version. The RMA was firstly introduced to focus 2-D SAR data acquired from a space-borne platform in the strip-map mode. Later it was adapted to be used in the spotlight mode [20, 51, 52]. Results showing that the RMA can also focus 2-D SAR data acquired in an anechoic chamber using the strip-map mode are reported in [53]. Both the 2-D and 3-D versions of the RMA basically require a 1-D interpolator and FFT codes. As a result, their implementation on a massively parallel supercomputer becomes fairly straightforward [54, 55].

Chirp Scaling Algorithm: It has the original characteristic of not requiring any interpolation [56]. It works with motion compensation to a line and corrects approximately the range curvature. It is widely used to focus 2-D space- and air-borne SAR data sets.

Space-Variant Matched-Filter Imaging Algorithm: This is a near-field imaging technique which accounts precisely for the wavefront curvature and the free space propagation loss. The core of the algorithm resides in the calculation of a near-field focusing operator, which is convoluted with the backscatter data. It is highly accurate and can be used with different types of scanning geometries. An important feature of this algorithm is that, in addition to the imaging of targets in free-space, it can also form subsurface radar images taking into account both the refraction and dispersion of the wavefield. Implementation examples of this algorithm are presented in [57, 58, 59].

1.2   Scope and objectives of the Thesis

The research presented in this Thesis has been carried out while working at the European Microwave Signature Laboratory (EMSL) [60]. This laboratory is one of the experimental facilities of the Humanitarian Security Unit (HSU), Institute for the Protection and Security of the Citizen (IPSC), Directorate General Joint Research Center (JRC) of the European Commission. As shown in Figure 1.1, the overall structure of the anechoic chamber of the EMSL is formed by the conjunction of a hemispherical and a cylindrical part, both with radius 10 m. In the gap between the two parts, a circular rail is mounted where two sleds carrying the antennas can move independently. The radar system is wideband, fully polarimetric and can be operated in both imaging and scatterometric modes. A unique feature of this facility is that it allows the synthesis of 2-D apertures, which can be either spherical or cylindrical.
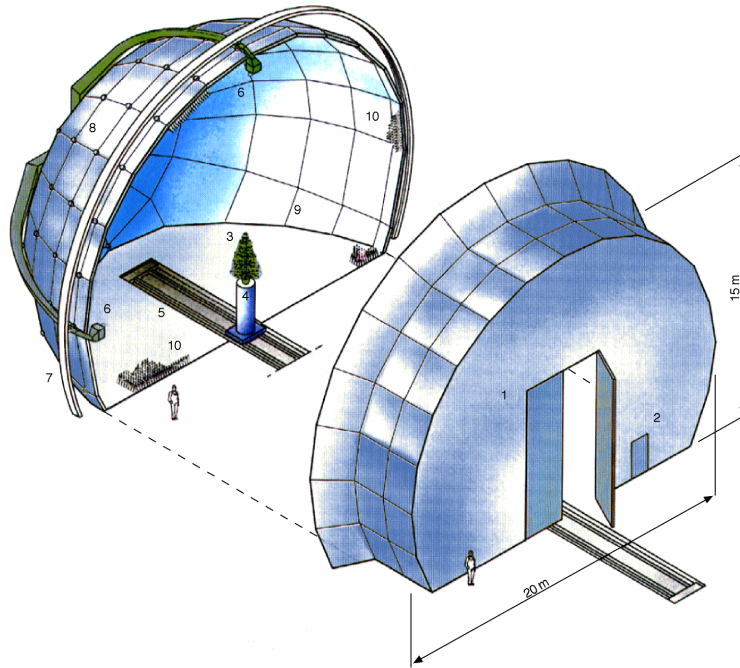
Figure 1.1. Exploded view of the EMSL.

The main objective of this Thesis was to develop a set of rapid and efficient 3-D near-field imaging algorithms for the identification and characterization of radar reflectivity components of complex objects. The development of these algorithms has been carried out considering their subsequent testing with experimental data acquired at the EMSL.

It is important to note that the imaging algorithms presented here rely on the SAR principle and as such they are based on a linearization of the electromagnetic wave scattering problem. This means that the interaction between the scatterers present in the scene is totally neglected. There are a number of microwave and acoustic imaging algorithms developed in the field of linearized inverse scattering (i.e., under the Born approximation) which provide alternative solutions to this problem [61, 62]. An example of a non-linear 3-D imaging algorithm dealing with the inverse scattering problem is reported in [63]. Further, the formulation used is always based on the scalar wave equation. Consequently, in the case of a polarimetric data set, the processing needs to be applied separately to each polarization channel.

The SAR system is nominally a linear system characterized by a space-invariant impulse response function. However, under the near-field condition, there are factors that contribute non-linear behavior and space-variant effects. The quality of a SAR system is normally measured in terms of the spatial resolution and the peak sidelobe levels. In this Thesis, numerical simulations using scenes with ensembles of ideal point scatterers

are employed to assess the quality of a near-field imaging algorithm. This is a common practice in the field of radar imaging.

It is well known that the resolution of any SAR system is subject to fundamental limitations [64]. Basically, the spatial resolution will depend on the shape and dimensions of the volume occupied in the spatial frequency space. This volume is larger under the near-field condition. Consequently, the achievable resolutions with a near-field SAR are slightly higher than those of a far-field SAR.

This Thesis is organized as follows. Chapter 2 deals with the introduction of the fundamentals of range-Doppler radar imaging, which is needed in order to properly understand the imaging techniques presented thereafter. In addition, the formulation of radar imaging algorithms under the near-field and the far-field condition is outlined.

Chapter 3 introduces a novel 3-D near-field radar imaging technique based on the RMA [65]. As an input, the 3-D RMA requires frequency domain backscatter data acquired on a 2-D planar aperture using a stepped frequency radar. The 2-D synthetic aperture is assumed to be planar and within the near-field zone of the target. The spatial resolution in the vertical and horizontal cross-range directions are given by the dimensions of the synthetic aperture, whereas resolution in ground-range is provided by the synthesized frequency bandwidth. The frequency domain data is used because the RMA algorithm works in this domain. Note that the focusing of time domain data sets acquired with a pulsed system would become straightforward by simply applying a Fourier transform.

The 3-D RMA cannot be directly applied with cylindrical and spherical scanning geometries. However as an alternative solution for these scanning geometries, it is proposed to backpropagate the backscattered data onto a planar aperture and then apply the 3-D RMA [66].

The proposed backpropagation technique of the frequency domain backscatter data is based on the so-called "radiating reflectors" model [19]. In this model, the scatterers are assumed to radiate simultaneously a wavefield which propagates at a velocity which is one half of the actual value. Under this assumption, the backscattered fields can be approximated as a solution of the 3-D Helmholtz equation. Consequently, field translations techniques used in antenna measurements (e.g., near-field to far-field transformations of an antenna pattern) can be adapted to translate the backscattered fields. Here these field translations are applied to obtain the backscattered fields that would have been measured on a planar aperture from those actually measured on a cylindrical or spherical aperture.

The work presented in Chapter 3 is the result of a joint effort with Dr.-Ing. Juan-Manuel López-Sánchez, who was working at the JRC at the time these algorithms were

developed.

Chapter 4 deals with two novel imaging algorithms. First, a 3-D SAR algorithm based on the use of a space variant matched filter or near-field focusing function, which accounts for the wavefront curvature and the propagation losses. The spatial distribution of the target reflectivity is estimated by means of an azimuth convolution between the near-field focusing function and the frequency domain data, followed by a coherent integration over the frequency band and the synthetic aperture in elevation. The circular convolution in azimuth is performed by applying FFT techniques, which reduce drastically the computing time. Moreover, instead of using a DFT, the focusing function in the azimuth wavenumber domain is evaluated through an asymptotic expansion obtained by the MSP. This asymptotic expansion is further optimized by using working matrices with the points of stationary phase and their second order derivatives. Second, an imaging algorithm based on the 3-D polar format algorithm (PFA) followed by a geometric rectification of the image. This algorithm is specially tailored to be employed as a quick-look SAR processor. High quality imagery will only be obtained with narrow spans of the two aspect angles.

Chapter 5 reports on a tree imaging experiment conducted in the anechoic chamber of the EMSL [67]. The main objective of this experiment was to map the radar reflectivity of an entire Fir tree in order to support the understanding of the interaction of electromagnetic waves with natural targets and provide the base for the validation and verification of existing models.

Chapter 6 presents a novel 3-D near-field subsurface imaging technique [59]. The subsurface image is accurately focused taking into account both the refraction and dispersion of the wavefield. The use of this subsurface imaging technique is subject to a number of assumptions: the dielectric properties of the ground are known (i.e., the complex permittivity as a function of the frequency), the ground is non-magnetic and therefore it is unequivocally characterized by its dielectric permittivity, the air-ground interface is planar, and the ground is perfectly homogeneous out of the region occupied by the buried objects.

Finally, Appendix A presents the formulation of 3-D RMA making use of the MSP, Appendix B deals with an assessment of the accuracy and validity range of the translation of 2-D backscattered fields, Appendix C introduces an algorithm for the efficient calculation of the amplitudes of the spherical harmonics $c_{m.n}$, and Appendix D gives the solution of a Fourier integral using the MSP. Appendix E gives a list of the articles published in refereed journals.

Radar Imaging Fundamentals

2.1 Introduction

The purpose of this Chapter is to present the fundamentals of range-Doppler radar imaging. The principal feature of an imaging radar is that it is coherent. Coherent radars utilize the range-Doppler principle to form the desired image. Thus, the image is formed using conventional techniques (i.e., a Fourier transform or range compression) to obtain fine-range resolution. The Doppler frequency gradient generated by the rotation of the object field relative to the radar is used to obtain a cross-range resolution that is much finer than that obtainable by the radar's beamwidth [8, 49].

The fundamentals presented here involve a 3-D imaging geometry with separate (i.e., bistatic) transmitting and receiving antennas moving along arbitrary trajectories, as shown

(a)   **(b)**
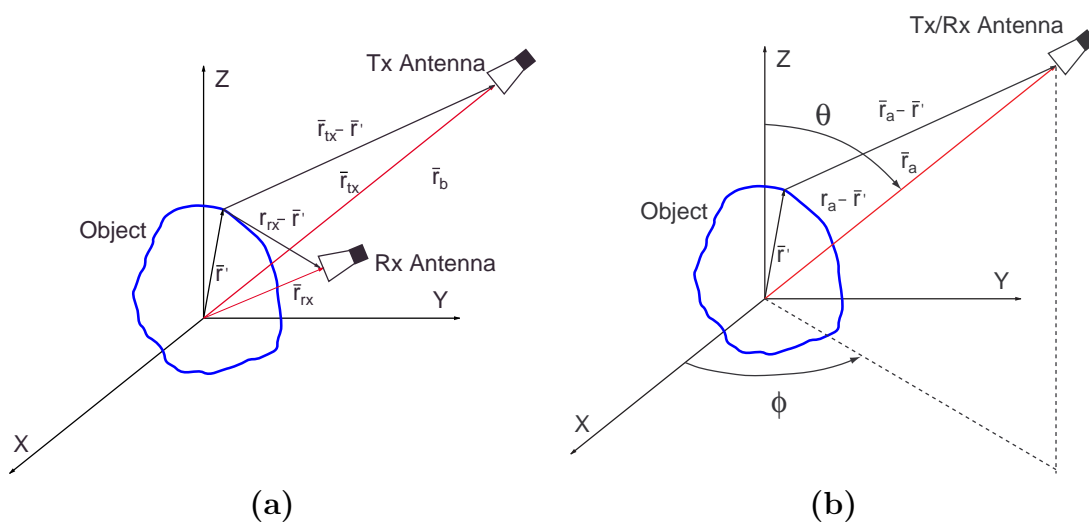
Figure 2.1. Generic 3-D radar imaging geometries: (a) bistatic and (b) monostatic.

in Figure 2.1 (a). Both the object and the antennas can have arbitrary motion, although only the relative motion of the scatterers with respect to the antennas is important for the radar imaging methods considered here.

The fundamental task of a radar imaging system is to estimate the radar reflectivity $\sigma(\mathbf{r}')$ of each element of the object as a function of the spatial coordinate $\mathbf{r}'$. As in any imaging system, the reflectivity function is approximated by an image function $I(\mathbf{r}')$, which is calculated from the returned radar signals. Because of the limitations of the radar data, the function $I(\mathbf{r}')$ will be a blurred representation of $\sigma(\mathbf{r}')$. This blurring is characterized by the so-called "point-spread function" or impulse response from an isolated point scatterer. To obtain imagery of good quality, it is important that the impulse response have its maximum at the location of the point scatterer and have as sharp a peak as possible with low side-lobes.

Most of the objects of interest can be modelled as an ensemble of non-dispersive elementary scatterers and, under the assumption of linearity (i.e., neglecting the interaction between the scatterers), the image $I(\mathbf{r}')$ can be represented as a superposition of point target response functions. For a transmitted signal $s(t)$, the signal received from a point scatterer located at $\mathbf{r}'$ is

$$s_r(t) = \sigma \; s\left[t - \frac{R_{\mathrm{tx}} + R_{\mathrm{rx}}}{c}\right] \tag{2.1}$$

with

$$
\begin{aligned}
R_{\mathrm{tx}} &= |\mathbf{r}_{\mathrm{tx}} - \mathbf{r}'| \\
R_{\mathrm{rx}} &= |\mathbf{r}_{\mathrm{rx}} - \mathbf{r}'|
\end{aligned}
\tag{2.2}
$$

where $R_{\mathrm{tx}} + R_{\mathrm{rx}}$ is the time-varying two-way range to the object point, c denotes the speed of light, and σ is the reflectivity associated with the point scatterer. In general, an image of the object can be formed if $R_{\mathrm{tx}} + R_{\mathrm{rx}}$ is a different function of time for each point on the object. All of the imaging methods presented in this Thesis are based on the same fundamental process of measuring range and changes in range to achieve image resolution.

2.2 Image formation in the spatial frequency domain

A well-known method for processing the received radar data to form an image of the scene is that working in the spatial frequency domain [3]. The radar returns are first converted to the frequency-domain by means of a Fourier transform [68, 69], which corresponds to a polar line segments in the 3-D frequency space of the target. This step can be omitted when the radar operates in the stepped-frequency mode (i.e., sampling the received signal

directly in the frequency domain by transmitting a sequence of continuous wave pulses within the frequency range of interest) [49]. Each segment is oriented according to the angular coordinates of the radar at the time of transmission. Depending on the relative motion of the radar and target during the measurement, a portion of the 3-D spatial frequency space is collected.

The fundamental features of the processing in the spatial frequency space can be derived by observing that for each transmitted pulse $s(t)$, the complex signal received from a target field is given by

$$s_r(t) = \iiint_V \sigma(\mathbf{r}') \, s\left[t - \frac{R_{\text{tx}} + R_{\text{rx}}}{c}\right] \, d\mathbf{r}' \tag{2.3}$$

where $R_{\text{tx}} + R_{\text{rx}}$ is the two-way range to the differential scattering volume $d\mathbf{r}'$, $\sigma(\mathbf{r}')$ is the spatial distribution of radar reflectivity associated with the target which, for convenience, includes the two-way propagation effects and various system gains. The integration in (2.3) is carried out over the volume of the target.

In the frequency domain, the signal received becomes

$$S_r(f) = \iiint_V \sigma(\mathbf{r}') \, S(f) \, \exp\left[-j\frac{2\pi f}{c}(R_{\text{tx}} + R_{\text{rx}})\right] \, d\mathbf{r}' \tag{2.4}$$

where $s_r(t)$ and $S_r(f)$ constitute a Fourier transform pair. Consequently, $S_r(f)$ is given by

$$S_r(f) = \int_{-\infty}^{+\infty} s_r(t) \exp[-j \, 2\pi f t] \, dt \tag{2.5}$$

The main emphasis of this Thesis is on monostatic imaging using a stepped-frequency radar with a single Tx/Rx antenna, as shown in Figure 2.1 (b). In practice, because of the poor isolation achieved with a single antenna, two closely spaced antennas forming a tiny bistatic angle are used. Assuming a monostatic geometry is used, the frequency domain backscatter data can be calibrated by equalizing the measured returns from the target. A reference target with known RCS (e.g., a metallic sphere or disc) is measured to retrieve the equalization factor to be applied to the backscatter data. This is a common practice in RCS measurements using a stepped-frequency radar [12, 31]. The calibration of fully polarimetric backscatter data is more complex and requires the measurement of three-reference targets [70].

Under the assumption that the frequency domain data have been calibrated and the reference target was positioned at the origin of the coordinates system, the backscattered fields from a target field can be expressed as

$$E_s(f, \phi, \theta) = \exp\left[+j\frac{4\pi f}{c}r_a\right] \iiint_V \sigma(\mathbf{r}') \, \exp\left[-j\frac{4\pi f}{c}|\mathbf{r_a} - \mathbf{r}'|\right] \, d\mathbf{r}' \tag{2.6}$$

where $\mathbf{r_a}$ denotes the vector position of the Tx/Rx antenna. For a monostatic geometry it is evident that $\mathbf{r_a} = \mathbf{r}_{\text{tx}} = \mathbf{r}_{\text{rx}}$. The complex exponential outside the integral in (2.6) compensates for the motion of the antenna platform during the aperture synthesis. The motion compensation step must be performed with great precision to produce high-quality imagery.

2.2.1 Far-field formulation

Let us consider that the range to the origin of the coordinates system r_a is large compared with the size of the object. This is to say that the Tx/Rx antenna is in the far-field zone of the object. In RCS measurements, the far-field zone of the object can be defined as [71]

$$r_a \geq \frac{4D^2}{\lambda} \tag{2.7}$$

where D denotes the size of the object and λ is the wavelength at the working frequency. Note that in antenna measurements the far-field condition is satisfied at half the distance indicated in (2.7) because the measured phase is associated with the one-way range to the antenna under test.

If the Tx/Rx antenna is in the far-field zone of the object,

$$|\mathbf{r_a} - \mathbf{r}'| \simeq r_a - \mathbf{r}' \cdot \hat{\mathbf{r}}_{\mathbf{a}} \tag{2.8}$$

where $\hat{\mathbf{r}}_{\mathbf{a}}$ is the unit vector position of the Tx/Rx antenna. The resulting frequency-domain backscattered fields can then be expressed as

$$E_s(f, \phi, \theta) = \iiint_V \sigma(\mathbf{r}') \, \exp\left[+j\frac{4\pi f}{c} \, \hat{\mathbf{r}}_{\mathbf{a}}(\phi, \theta) \cdot \mathbf{r}'\right] \, d\mathbf{r}' \tag{2.9}$$

At this point, the spatial angular frequency variable can be defined as

$$\mathbf{k} = \frac{4\pi f}{c}\hat{\mathbf{r}}_{\mathbf{a}}. \tag{2.10}$$

With the above definition, the backscattered fields become

$$E_s(f, \phi, \theta) = \iiint_V \sigma(\mathbf{r}') \, \exp\left[+j \, \mathbf{k}(f, \phi, \theta) \cdot \mathbf{r}'\right] \, d\mathbf{r}' \tag{2.11}$$

The above integral equation indicates that an estimate of the target reflectivity $\sigma(\mathbf{r})$ can be obtained by carrying out a Fourier transform of the calibrated backscattered fields $E_s(f, \phi, \theta)$, i.e.,

$$I(\mathbf{r}) = \frac{1}{(2\pi)^3} \iiint_K E_s(f, \phi, \theta) \, \exp\left[-j \, \mathbf{k}(f, \phi, \theta) \cdot \mathbf{r}\right] \, d\mathbf{K} \tag{2.12}$$
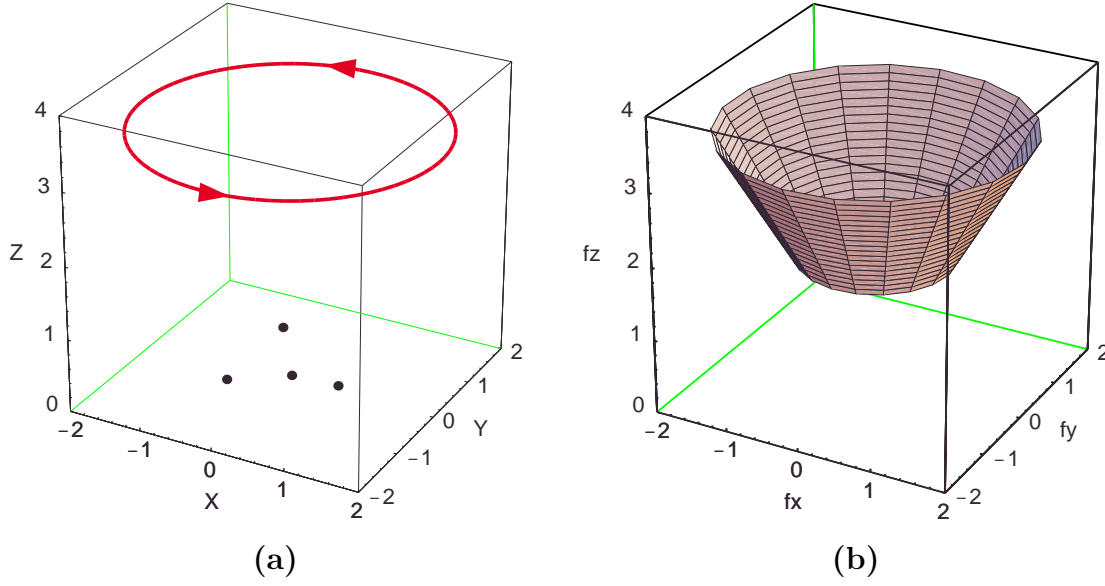
Figure 2.2. (a) Point targets in the object space imaged with a circular synthetic aperture; (b) Data surface observed in the frequency space.

wherein

$$d\mathbf{K} = \left(\frac{4\pi}{c}\right)^3 f^2 \, \sin\theta \, d\phi \, d\theta \, df \tag{2.13}$$

The spatial resolution of the resulting image $I(\mathbf{r})$ will depend on the shape and dimensions of the volume occupied in the spatial frequency space.

In practice, only a small portion of the frequency space is observed, with the attendant limitation on the point target response in each dimension. For example, a linear synthetic aperture produces planar data collection surfaces and the general 3-D processing problem reduces to a 2-D Fourier transformation with a resulting 2-D image of the object, i.e., with no resolution in the direction normal to the collection plane in the frequency space.

As an example, Figure 2.2 shows a generic target consisting of an ensemble of point scatterers imaged with a circular synthetic aperture and the corresponding surface observed in the spatial frequency space.

2.2.2 Near-field formulation

The Tx/Rx antenna is in the near-field of the object when

$$r_a < \frac{4D^2}{\lambda}. \tag{2.14}$$

Under the near-field condition, the approximation made in (2.8) cannot be used. Consequently, the estimate of the target reflectivity $\sigma(\mathbf{r})$ cannot be simply obtained via a Fourier

transform of the backscatter data. An alternative procedure to form the radar image is as follows. First, the integral equation in (2.6) is rewritten as

$$E_s(f, \phi, \theta) = \iiint_V \sigma(\mathbf{r}') \, \exp\left[-j\frac{4\pi f}{c}(|\mathbf{r_a} - \mathbf{r}'| - r_a)\right] \, d\mathbf{r}'. \tag{2.15}$$

By noting that (2.15) resembles a Fourier integral, one can obtain an estimate of the reflectivity image using an integral resembling its inverse transform, i.e.,

$$I(\mathbf{r}) = \frac{1}{(2\pi)^3} \iiint_K E_s(f, \phi, \theta) \, \exp\left[+j\frac{4\pi f}{c}(|\mathbf{r_a} - \mathbf{r}| - r_a)\right] \, d\mathbf{K}. \tag{2.16}$$

The next chapters present various imaging algorithms which are all based on (2.16). The efficiency of the proposed algorithms will depend on our ability to make an extensive use of FFT techniques in the calculation of the integral in (2.16). This will significantly depend on the geometry of the synthetic aperture used. It is important to mention that this integral cannot be always formulated in the form of a Fourier transform.

2.3   Image formation in the time domain

The formation of a radar image in the time domain is an alternative approach which needs also to be considered. SAR or range-Doppler processing in the time domain works as follows [72]. Each pixel in the image where the reflectivity is estimated will show a distinct Doppler profile (or phase history in the frequency domain). The Doppler profile is the two-way propagation time as a function of all the antenna positions on the synthetic aperture to the location represented by that pixel. Thus, an image can be formed by simply assigning to each pixel a matched filter to the Doppler profile associated with its position.

The corresponding time domain formulation for the far-field imaging algorithm takes the following form,

$$I(\mathbf{r}) = \int_\phi \int_\theta E_s^t(t = \frac{2}{c}[r_a - \mathbf{r} \cdot \hat{\mathbf{r}}_\mathbf{a}], \phi, \theta) \; \sin\theta \, d\theta \, d\phi \tag{2.17}$$

where $E_s^t(t, \phi, \theta)$ denotes the backscattered fields in the time domain (i.e., after a 1-D Fourier transform of the frequency domain backscatter data), which is given by

$$E_s^t(t, \phi, \theta) = \frac{8}{c^3} \int_f E_s(f, \phi, \theta) \, f^2 \, \exp\left[+j\frac{4\pi f}{c}t\right] \, df. \tag{2.18}$$

Since the compression in range has already been performed, the integration is only carried out over the two aspect angles (ϕ, θ).

In the time domain, the reflectivity image under the near-field condition can be estimated as follows,

$$I(\mathbf{r}) = \int_\phi \int_\theta E_s^t(t = \frac{2}{c}[|\mathbf{r_a} - \mathbf{r}| - r_a], \phi, \theta) \; \sin\theta \; d\theta \; d\phi. \qquad (2.19)$$

The factor $\sin\theta$ in (2.17) and (2.19) comes from the Jacobian in spherical coordinates. In practice, this factor does not play an important role as its effect is totally cancelled out when the data are windowed prior to the azimuth compression.

3-D Near-Field Radar Imaging Using Seismic Migration Techniques

3.1 Introduction

It is well known that a 2-D reflectivity image can be formed by synthesizing a 1-D aperture with a wide-band radar [49]. Accordingly, a 3-D reflectivity image can be formed by synthesizing a 2-D aperture. As an example, typical geometries of the 2-D apertures that can be synthesized in an anechoic chamber are planar, spherical and cylindrical.

In this chapter a novel 3-D near-field radar imaging technique based on the RMA [65] is presented. The formulation of the 3-D RMA has been derived by using the MSP [73], as suggested in [48] for the 2-D RMA. Further details on the use of the MSP are given in Appendix A. As an input, the 3-D RMA algorithm requires frequency domain backscatter data acquired on a 2-D planar aperture. The frequency domain data are preferred because the RMA algorithm works in the frequency wavenumber domain.

The 3-D RMA shows some similarities with the synthetic aperture focusing technique (SAFT) [45, 74, 75, 76, 77]. This is a focusing technique well known in the fields of ultrasonics and medical imaging, which is based on a 3-D time domain backpropagation. However, as opposed to the presented technique, the SAFT is a time domain technique and does not make any use in its formulation of neither the Stolt interpolator nor the MSP. On the other hand, both algorithms require planar scan surfaces and can be applied under the near-field condition. The computational efficiency of these two techniques are supposed to be of the same order since both algorithms make an extensive use of FFT codes. Another similar algorithm developed in the field of ultrasonics is the Closed Time Reversal Cavity [78, 79, 80].

The 3-D RMA cannot be directly applied with cylindrical and spherical scanning ge-
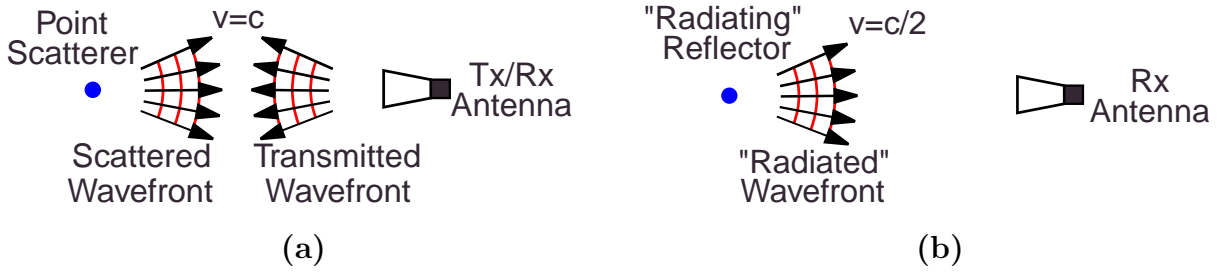
Figure 3.1.   (a) Transmitted and backscattered wavefronts propagating at $v = c$; (b) The "radiating reflectors" model with a radiated wavefront propagating at $v = c/2$.

ometries. However, for these scanning geometries, an alternative solution is to backpropagate the backscattered data onto a planar aperture and then apply the 3-D RMA [66]. The proposed backpropagation technique of the frequency domain backscatter data is based on the so-called "radiating reflectors" model [19]. Note that since the RMA also originates from geophysics, its validity when applied to SAR is based upon this model. In the "radiating reflectors" model, see Figure 3.1, the scatterers are assumed to radiate simultaneously a wavefield which propagates at a velocity which is one half of the actual value. Under this assumption, the backscattered fields can be approximated as a solution of the 3-D Helmholtz equation. Consequently, field translation techniques used in antenna measurements (e.g., near-field to far-field transformations of an antenna pattern) can be adapted to translate the backscattered fields. Here these field translations are applied to obtain the backscattered fields that would have been measured on a planar aperture from those actually measured on a cylindrical or spherical aperture. An assessment of the accuracy and validity range of the translation of 2-D backscattered fields is presented in the Appendix B.

Assuming the validity of the "radiating reflectors" model, the translation of the backscattered fields works as follows. First, the modal coefficients or harmonics amplitudes of the measured backscatter data are calculated. The type of basis functions will depend on the geometry of the aperture. The basis functions associated with the cylindrical and spherical apertures are the so-called cylindrical and spherical harmonics, respectively. The modal coefficients are determined by matching the backscattered fields on the measured aperture. Once these coefficients are known, the modal expansion is then evaluated on a planar surface in the vicinity of the measured aperture. At that stage, the RMA can be readily applied to the translated fields provided they are properly sampled on a planar aperture. Note that in case of a fully polarimetric measurement, the field translation needs to be applied separately for each polarization.

Due to practical limitations, it is important to note that the measurement aperture will enclose the target only partially and therefore the validity region of this extrapolation will

be limited. In fact, the modal coefficients are calculated assuming that the backscattered fields vanish outside the measurement aperture. This means that the further the backscattered field are backpropagated, the higher will be the truncation errors in the estimation of the translated fields. The mitigation of these truncation errors is an important topic of current research in the field of antenna measurements [81, 82, 83, 84, 85].

Since the proposed imaging technique can be used with planar, cylindrical and spherical apertures, the chapter has been split into three sections, each addressing the use of the 3-D RMA with a different scanning geometry. Section 3.2 presents the formulation of the 3-D RMA in a highly detailed form, the algorithm implementation, the required sampling criteria and the resulting resolutions, and the numerical simulations and experimental results obtained with this algorithm. Sections 3.3 and 3.4 address the formulation, algorithm implementation, the numerical simulations and the experimental results of the extension of the 3-D RMA to cylindrical and spherical scanning geometries, respectively.

3.2 Planar scanning geometry

3.2.1 Formulation

Consider the measurement set-up shown in Figure 3.2. A stepped frequency radar illuminates a target with a continuous wave (CW) of frequency f. The antenna is positioned at (x_a, R_o, z_a) and synthesizes a rectangular aperture on the plane $x - z$ at a distance
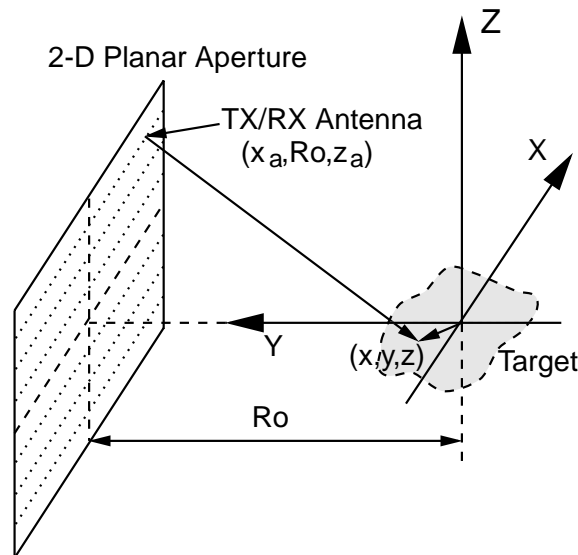
Figure 3.2. Measurement and imaging geometry.

R_o. The measurement points form a rectangular grid with spacings Δx_a and Δz_a in the horizontal and vertical cross-range directions, respectively. At each antenna position the synthesized frequency bandwidth is B. Thus, the acquired backscatter data $d(x_a, f, z_a)$ are a function of two spatial coordinates and the working frequency. The frequency variable is directly related with the two-way frequency wavenumber $k_r = 4\pi f/c$. Consequently, the measurement data can also be denoted as $d(x_a, k_r, z_a)$.

Assuming that there is a point scatterer located at (x, y, z) with reflectivity $s(x, y, z)$, then the measured backscatter is

$$d(x_a, k_r, z_a) = s(x, y, z) \, \exp\left[+jk_r R_o\right] \, \exp\left[-jk_r R\right] \tag{3.1}$$

where R is the range to the point scatterer, i.e.

$$R = \sqrt{(x - x_a)^2 + (y - R_o)^2 + (z - z_a)^2} \tag{3.2}$$

The first exponential in (3.1) establishes the phase reference at the origin of the coordinates system which is at a distance R_o from the aperture. In the 2-D RMA this reference is a line parallel to the linear aperture. The second exponential simply accounts for the phase history associated with the point scatterer. Note that, for the sake of simplicity, the losses due to the free-space propagation and the antenna pattern are not considered here.

From (3.1), the 3-D radar reflectivity map associated with a distributed target can be expressed as

$$s(x, y, z) = \iiint\limits_{A, k_r} d(x_a, k_r, z_a) \, \exp\left[-jk_r R_o\right] \, \times$$

$$\exp\left[jk_r \sqrt{(x - x_a)^2 + (y - R_o)^2 + (z - z_a)^2}\right] \, dx_a \, dz_a \, dk_r \tag{3.3}$$

where A denotes the surface of the synthetic aperture. Equation (3.3) can be reformulated in order to show that the focusing algorithm simply reduces to a 2-D convolution and a frequency integration

$$s(x, y, z) = \int\limits_{k_r} \exp\left[-jk_r R_o\right] \iint\limits_{A} d(x_a, k_r, z_a) \, \times$$

$$\exp\left[jk_r \sqrt{(x - x_a)^2 + (y - R_o)^2 + (z - z_a)^2}\right] \, dx_a \, dz_a \, dk_r \tag{3.4}$$

Note that (3.3) is a solution of the linearized inverse scattering problem and as such it only holds under the first-order Born approximation [86]. Here it is also assumed that

the backscattered fields will vanish at the boundaries of the aperture. This boundary condition is satisfied by simply applying a 2-D weighting function or window prior to the focusing, something which is a common practice in any imaging algorithm.

The 2-D convolution in the aperture coordinates (x_a, z_a) can be computed in the Fourier domain as a complex product if the following 2-D Fourier Transform (FT) were known

$$E(k_x, k_z) = \iint \exp\left[jk_r\sqrt{x^2 + (y - R_o)^2 + z^2}\right] \exp\left[-jk_x x - jk_z z\right] \, dx \, dz \qquad (3.5)$$

This kind of integrals, under certain conditions, can be evaluated analytically by using the MSP [73]. The MSP states that the main contribution to the integral come from points with stationary phase (nulls of the phase derivative), and gives an asymptotic expansion for the integral. The evaluation of the 2-D integral in (3.5) by means of the MSP results in (see Appendix A)

$$E(k_x, k_z) \simeq \frac{2\pi k_r}{jk_y^2} \, \exp\left[-jk_y(y - R_o)\right] \qquad (3.6)$$

where $k_y = \sqrt{k_r^2 - k_x^2 - k_z^2}$. Replacing the 2-D FT by its asymptotic expansion in (3.4), the 3-D reflectivity image is given by

$$s(x, y, z) \simeq \iiint\limits_K D(k_x, k_r, k_z) \, \frac{2\pi k_r}{jk_y^2} \, \exp\left[-jk_r R_o\right] \times$$
$$\exp\left[j(k_x x + k_z z - k_y(y - R_o))\right] \, dk_x \, dk_r \, dk_z \qquad (3.7)$$

where $D(k_x, k_r, k_z)$ is the 2-D horizontal/vertical cross-range FFT of the frequency domain backscatter data. The last exponential term takes the form of the Fourier kernel in a 3-D IFFT. However, prior to this 3-D IFFT, the wavenumber domain backscatter data need to be re-sampled uniformly in k_y. Then, by substituting the frequency wavenumber variable k_r by k_y, the reflectivity image takes the form,

$$s(x, y, z) \simeq \iiint\limits_K D(k_x, k_y, k_z) \, \frac{2\pi}{jk_y} \, \exp\left[-j(k_r - k_y)R_o\right] \times$$
$$\exp\left[jk_x x + jk_z z - jk_y y\right] \, dk_x \, dk_y \, dk_z \qquad (3.8)$$

Note that the amplitude term has been modified due to the change of variables $(k_r \rightarrow k_y)$. Equation (3.8) indicates that reflectivity image can be simply obtained through an 3-D IFFT of the product of the re-sampled wavenumber domain backscatter data by a complex exponential (also known as matched filter).
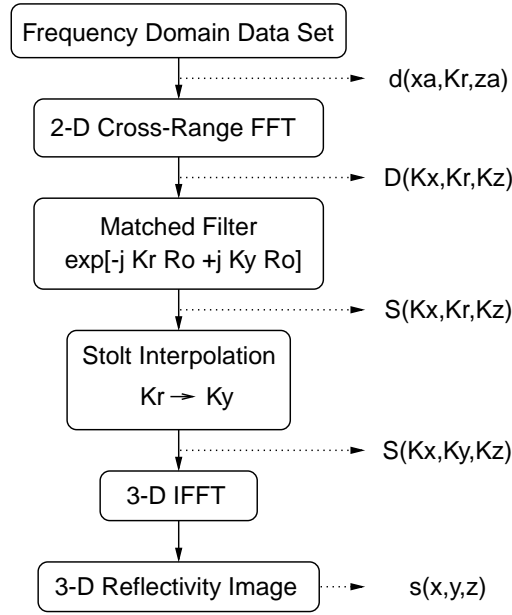
Figure 3.3. Block diagram of the 3-D RMA.

3.2.2 Algorithm implementation

This section deals with the practical implementation of the 3-D RMA. From (3.8), the image reconstruction process can be naturally split into four sequential steps (see Figure 3.3), namely: a 2-D cross-range FFT, matched filtering, Stolt interpolation, and a 3-D IFTT. The first and the last steps are obvious and will not be discussed here. However, the matched filter and the Stolt interpolation deserve special treatment.

The matched filter is necessary to introduce a motion compensation to the wavenumber domain backscatter data. This motion compensation corrects for the wavefront curvature of all scatterers at the same ground range as the scene center (i.e., the origin of the coordinates system). In the next step, the residual range curvature of all scatterers will be removed. The phase associated with the matched filter is space-invariant and depends only on the range to the scene center R_o, the frequency and the cross-range wavenumbers. It is given by

$$\Phi_{\mathrm{MF}}(k_x, k_r, k_z) = -k_r\, R_o + k_y\, R_o = -k_r\, R_o + \sqrt{k_r^2 - k_x^2 - k_z^2}\, R_o \qquad (3.9)$$

where the identity

$$k_y = \sqrt{k_r^2 - k_x^2 - k_z^2} \qquad (3.10)$$

is known as the Stolt transformation [21]. Note that, in (3.10), k_y must be real and therefore the region in the wavenumber domain where the asymptotic expansion of the

MSP is valid reduces to

$$k_r^2 \geq k_x^2 + k_z^2 \tag{3.11}$$

The field modes which satisfy this inequality are the so-called propagating modes, whereas those which do not propagate are the evanescent modes. The amplitude of the evanescent modes is affected by an exponential factor which rapidly vanishes with an increasing distance to the aperture $(y - R_o)$. In the formulation presented here, it is assumed that (3.11) is satisfied. In practice, the data points in the wavenumber domain outside the region defined by (3.11) will be discarded by applying a mask prior to the matched filter.

The third step performed in the 3-D RMA is the Stolt interpolation. This interpolation compensates the range curvature of all scatterers by an appropriate warping of the wavenumber domain backscatter data. After the matched filter the transformed data continue being equally spaced in frequency, and therefore in the k_r variable. In order to prepare the data for the last 3-D IFFT, the next step consists of a change of variables defined by the Stolt transformation, which can be implemented as a 1-D interpolation. As a result, the wavenumber domain backscatter data will be uniformly sampled in the k_y domain. In the present implementation of the algorithm, the sampling frequency is increased to be highly above the Nyquist limit, then a frequency down-conversion followed by a Lagrange interpolation is applied.

Once the Stolt interpolation is performed, the wavenumber domain backscatter data are multiplied by the amplitude terms introduced by the change of variable and the asymptotic expansion of (3.8). Then, the 3-D reflectivity image is obtained by simply applying a 3-D IFFT.

3.2.3 Sampling criteria and resolution

The resolution of the resulting 3-D reflectivity image depends on the frequency bandwidth, the center frequency and the dimensions of the synthetic aperture. The ground-range resolution is usually expressed as

$$\delta_y \simeq \frac{c}{2B} \tag{3.12}$$

where B is the frequency bandwidth. The horizontal and vertical cross-range resolutions are,

$$\delta_x \simeq \frac{\lambda_c R_o}{2L_x} = \frac{cR_o}{2f_c L_x} \tag{3.13}$$

$$\delta_z \simeq \frac{\lambda_c R_o}{2L_z} = \frac{cR_o}{2f_c L_z} \tag{3.14}$$

where L_x and L_z are the lengths of the 2-D synthetic aperture, and λ_c is the wavelength at the center frequency f_c.

In practice, the frequency domain backscatter data are windowed to lower the side-lobes in the imagery, and as a result the final resolutions are usually slightly poorer than those given by the above formulas.

Assuming that the target is confined within a rectangular box of dimensions $D_x \times D_y \times D_z$ centered at the origin of the coordinates system, the required sampling steps in the measurement to satisfy the Nyquist criterion are given by

$$\Delta_f \leq \frac{c}{2D_y} \tag{3.15}$$

$$\Delta x_a \leq \frac{\lambda_{min}}{2} \frac{\sqrt{(L_x + D_x)^2/4 + R_o^2}}{L_x + D_x} \tag{3.16}$$

$$\Delta z_a \leq \frac{\lambda_{min}}{2} \frac{\sqrt{(L_z + D_z)^2/4 + R_o^2}}{L_z + D_z} \tag{3.17}$$

where λ_{min} is the wavelength at the maximum working frequency.

The sampling intervals given by (3.16) and (3.17) are the usual ones in strip-map SAR. The measurement points on the aperture require a minimum spacing in order to sample adequately the phase history associated with all the scatterers after the matched filter. As a result, the sampling frequencies in a strip-map SAR are much higher than those in a spotlight configuration. Note that in a spotlight SAR the minimum cross-range spacing only depends on the target size and the distance to the aperture, but not on the aperture size as in a strip-map SAR. Consequently strip-map SAR measurements will have associated larger data volumes and thus longer measurement times.

Running a strip-map SAR measurement at the spotlight SAR sampling frequency will introduce aliasing in the acquired data set. However, the origin of the aliasing is known and can be eliminated by introducing a deterministic phase correction term. The phase correction term which needs to be applied is as follows

$$\mathrm{HF}(x_a, k_r, z_a) = \exp\left[jk_r(R_o - \sqrt{x_a^2 + R_o^2 + z_a^2}) \right] \tag{3.18}$$

After applying this correction term, the aliasing has been eliminated, the sampling rate can be increased in order to satisfy (3.16) and (3.17). Then a second phase correction, complex conjugate of the first one, is applied to restore the original phase reference in the data. The main advantage of this procedure is the reduction of both the data volume and the measurement times. From the viewpoint of the RMA, this pre-processing is completely transparent and does not have any side effect. Note that the 3-D RMA maintains the
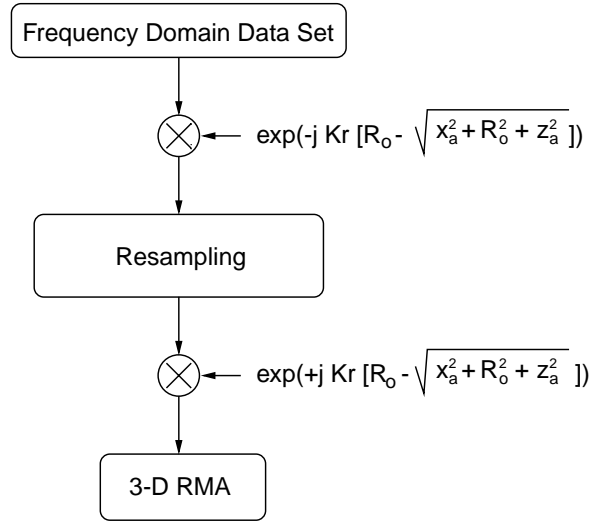
Figure 3.4. Pre-processing of data sampled at the spotlight rate.

same requirements in terms of internal memory and computational load. The flowchart associated with this pre-processing is shown in Figure 3.4. The resulting cross-range sampling intervals (i.e., the ones used in a spotlight SAR) are:

$$\Delta_{x_a} \leq \frac{\lambda_{min} R_o}{2\sqrt{D_x^2 + D_y^2}} \tag{3.19}$$

$$\Delta_{z_a} \leq \frac{\lambda_{min} R_o}{2\sqrt{D_z^2 + D_y^2}} \tag{3.20}$$

An alternative technique to process strip-map data at the spotlight sampling frequency is presented in [51, 52]. This technique, known as Frequency domain Replication and Down-sampling (RMA-FReD), has been used with air-borne data. With this technique, the blurred replicas due to the aliasing fall ideally out of the scene, and the final image exhibits a slightly lower signal-to-background-ratio and a wider impulse response. If this minor degradation in the image quality is accepted, one can use the RMA-FReD as a quick-look processor. Note that, with the RMA-FReD, the data volume to be processed is significantly smaller than that of the conventional RMA. In the next section, the results obtained with these two processors are compared.

3.2.4 Numerical simulations

Figure 3.5 shows a sketch of the target used in the first numerical simulation. The target consists of a 3-D array of $5 \times 5 \times 5$ point scatterers uniformly distributed within a box of side 1 m. All scatterers have the same RCS: 0 dBsm. A Tx/Rx antenna synthesizes a
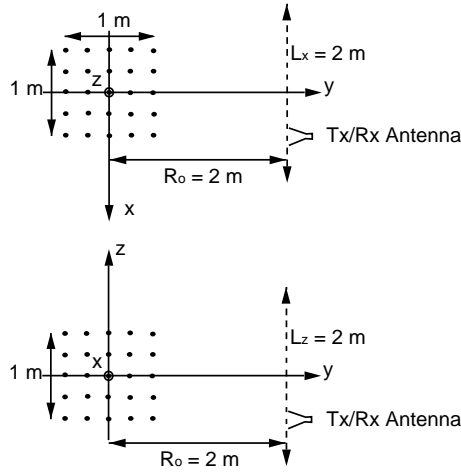
Figure 3.5. Measurement set-up used in the numerical simulation with the 3D array of 125 point scatterers.

planar aperture of 2 m × 2 m located at $R_o = 2$ m from the target center. The number of measurement points is 51, spaced 4 cm, in both the horizontal and vertical cross-range directions. These sampling intervals have been selected according to the spotlight criterion. The resulting sampling intervals without the proposed pre-processing would be 2 cm. The frequency ranges from 2 to 6 GHz, sampling a total of 41 points with a step of 100 MHz. According to these parameters the theoretical resolution is 3.75 cm along the three main axes.

Two 3-D reflectivity images have been reconstructed using the RMA and the RMA-FReD, respectively. The reflectivity image has been reconstructed in a cube of side 1.2 m, with a total of 61 voxel in each dimension. Figure 3.6 shows the projection of the images onto the three main planes. A Kaiser-Bessel ($\alpha = 2$) window has been applied along the dimensions of the frequency domain data set [87]. The dynamic range shown in the image is 50 dB. Both results show a slight dependence on the ground-range coordinate (y). This effect is common in near field measurements since the algorithm does not focus with the same accuracy close and distant scatterers. Anyway, the quality of the reconstructed image is quite satisfactory and, moreover, the processing time much shorter. In the RMA case the processing time was 3 min and 40 secs, requiring about 13 MByte of RAM. The image obtained with the RMA-FReD processor shows some inaccuracies at reflectivity values below –30 dBsm. These imperfections are present in the near range zone because this area introduces the highest spatial frequencies. However, with this processor, the processing time took only 1 min, requiring only 3 MByte of RAM.

The second simulation is intended to estimate the dynamic range of the 3-D RMA processor. The target is similar to that used in the previous simulation. It consists of

(a)   **(b)**
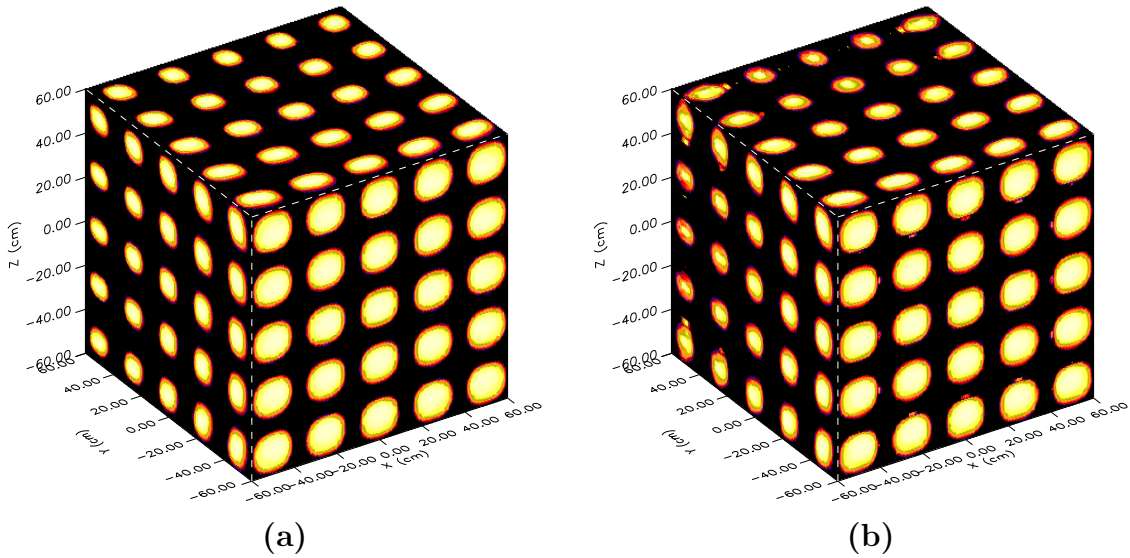
Figure 3.6.   Projections of the 3-D SAR image onto the $x - y$, $x - z$ and $y - z$ planes. Simulation of 125 point scatterers. Parameters: $R_o = L_x = L_z = 2$ m, $f = 2$–6 GHz, $\delta x = \delta y = \delta z = 3.75$ cm, $\Delta f = 100$ MHz, $\Delta x_a = \Delta z_a = 4$ cm, Displayed dynamic range is 50 dB. (a) Original RMA (b) RMA-FReD.

Table 3.1. Measured reflectivity values for the target in Figure 3.7.

Nominal	Measured RCS (dBsm)		
RCS (dBsm)	$y = -0.4$ m	$y = 0.0$ m	$y = 0.4$ m
0	-0.08	-0.10	-0.12
-10	-10.39	-10.53	-10.71
-20	-20.71	-20.95	-21.30
-40	-40.69	-40.94	-41.30
-60	-60.75	-60.99	-61.31
-80	-79.82	-80.45	-81.07

three parallel planes spaced 40 cm, where 9 scatterers have been uniformly distributed as shown in Figure 3.7 (a). The reflectivities now vary and range from 0 to –80 dBsm. The measurement set-up is identical to that of the first simulation. The reflectivity image has been reconstructed using the 3-D RMA. Figure 3.7 (b) shows the slice corresponding to a vertical plane parallel to the aperture at $y = 0$. The dynamic range of this image is 100 dB. As in the previous results, a Kaiser-Bessel ($\alpha = 2$) window has been applied. It is seen that the dynamic range of the imaging algorithm is better than 80 dB. In practice, the dynamic range will be limited by the presence of noise in the system. Table 3.1 compares the reconstructed values of the reflectivity with the actual ones. The maximum error is in the order of 1.5 dB.
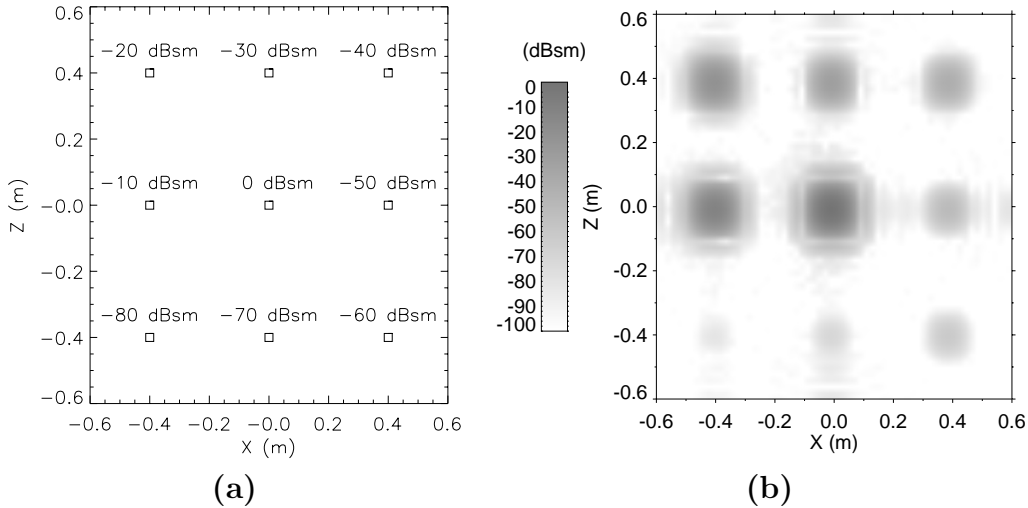
Figure 3.7. Target modelled to evaluate the dynamic range. (a) Sketch of the target; (b) Slice of the reflectivity image.

3.2.5 Experimental results

The presented 3-D imaging algorithm has been tested experimentally by using an outdoor Linear SAR system (LISA) of the Humanitarian Security Unit at JRC-Ispra. This facility is based on a stepped frequency radar which is equipped with a 2-D positioning system. The maximum aperture dimensions are at present limited to 5 m and 1 m in the horizontal and vertical cross-range directions, respectively. The positioning accuracy is better than 0.1 mm. The frequency range is primarily limited by the type of antennas being used. The system performs quasi monostatic measurements using two closely spaced horn antennas. Figure 3.8 shows the measurement set-up used in the experiment. The target consisted of a 3-D arrangement of eight metallic spheres of diameter 7.62 cm, positioned as shown in Figure 3.9. The dimensions of the 2-D synthetic aperture were 1 m × 1 m, with a total of 41 measurement points equally spaced in the horizontal and vertical directions. The backscattered fields in the HH polarization were acquired at 401 frequency points spaced 5 MHz within the frequency range 15.5 to 17.5 GHz. The range from the center of the aperture to the center of the target was 2.3 m, with the plane of the aperture tilted 14 degrees from the vertical. The expected resolutions are 2 cm in the horizontal (x) and vertical (z) cross-range directions, and 7.5 cm in the ground-range (y) direction.

   The measurement time required for this experiment was approximately 2 hours. A 3-D reflectivity image confined in a box of side 60 cm with 61 voxel in each dimension was reconstructed with a processing time of 1 min and 43 secs. Figure 3.10 shows some slices out of the reconstructed 3-D image: three slices at different ground-range ($y = -16, 0, +16$ cm) and cross-range ($x = -16, 0, +16$ cm) positions. The displayed dynamic

range is 20 dB. As expected, the reflectivity at the positions of the spheres is about –
23.4 dBsm, corresponding to the RCS given by the physical optics approximation [88].
The measured spatial resolutions are in agreement with the expected ones. Note that the
reflectivity peaks of the spheres closer to the antennas are narrower because the effective
synthetic aperture is larger in the near range. On the other hand, the spheres have a
diameter of approximately four wavelengths and therefore do not represent ideal point
scatterers. As a result, a minor degradation or defocusing must be expected.

What follows is a description of the field translations which have been applied to obtain
the backscattered fields that would have been measured on a planar aperture from those
actually measured on a cylindrical or spherical aperture. The formulation associated with
the field translation is based on the wave equation in its scalar form. The "radiating
reflectors" model is used in order to extend the validity of the Helmholtz equation to the
backscattered fields.

3.3 Cylindrical scanning geometry

The geometry of the problem is shown in Figure 3.11. A Tx/Rx antenna synthesizes a
cylindrical aperture of radius ρ_a. The aperture is uniformly sampled both in the z and the
ϕ directions within the ranges $z_{min} \leq z \leq z_{max}$ and $\phi_{min} \leq \phi \leq \phi_{max}$. At each antenna
position the synthesized frequency bandwidth is B. The target is assumed to be centered
at the origin of the coordinates system. The axis of the cylindrical aperture coincides with
the z-axis.

Figure 3.8. Photograph of the experiment set-up with LISA.
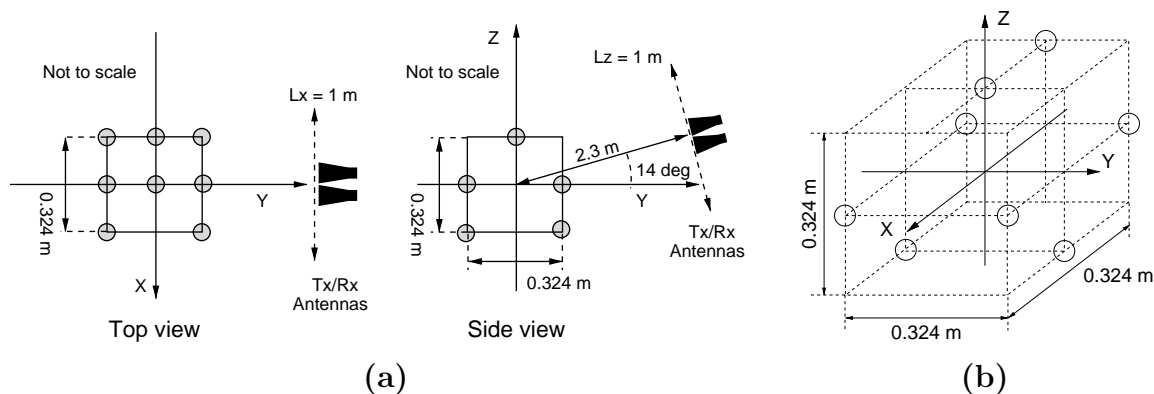
Figure 3.9. (a) Arrangement of the measurement set-up used in the experiment with a 3-D array of eight spheres; (b) Sketch of the target.
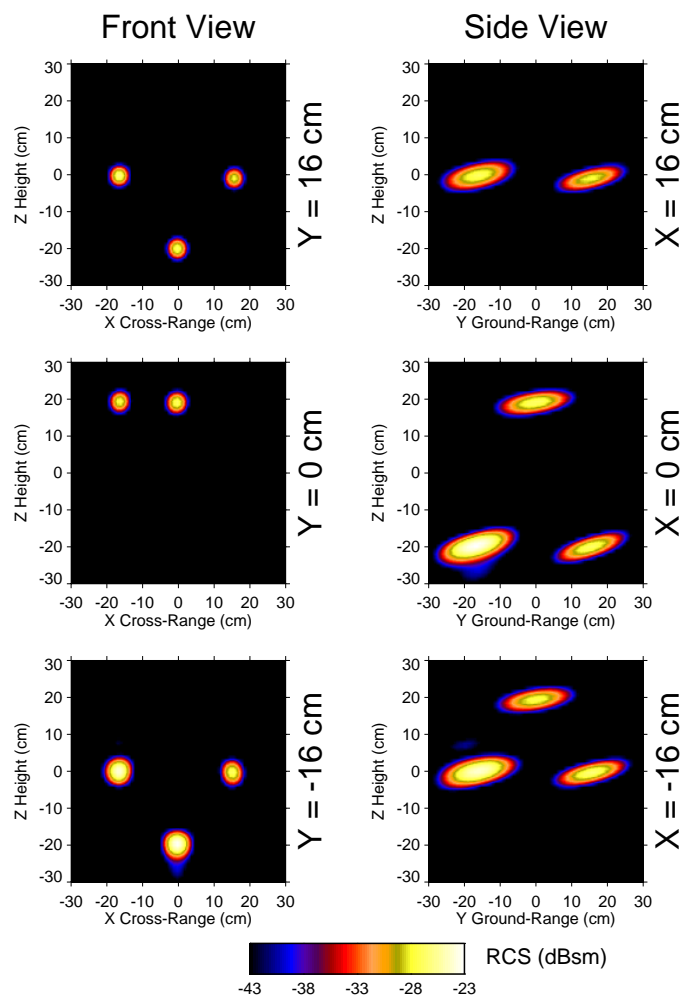
Figure 3.10. Slices of the reconstructed 3-D image with the eight spheres measured by LISA.

3.3.1   Fields translation

Let us assume the measured backscattered fields are a solution of the 3-D scalar Helmholtz equation. Thus, the general solution of this equation can be expanded into a sum of cylindrical harmonics as follows [89]

$$\psi(\rho, \phi, z) = \sum_{n=-\infty}^{\infty} \sum_{k_z=-\infty}^{\infty} c_{n,k_z} H_n^{(2)}(k_\rho \rho) \, e^{jn\phi} \, e^{jk_z z}, \qquad (3.21)$$

where $H_n^{(2)}(\cdot)$ is the Hankel function of second kind and integer order n, c_{n,k_z} are the amplitudes of the cylindrical harmonics, k_ρ and k_z are the wavenumbers along ρ and z, respectively. These two wavenumbers are related with the frequency wavenumber through this equation

$$k_\rho^2 + k_z^2 = k_r^2. \qquad (3.22)$$

In practice the two summations in (3.21) will be always truncated at the limits $|n| \leq N$ and $|k_z| \leq k_z^{max}$. The maximum value of n depends on the radius of the minimum cylinder, concentric with the cylindrical aperture that encloses entirely the target. If the radius of this minimum cylinder is ρ_{min}, the following empirical rule gives a value for N

$$N = [k_\rho \, \rho_{min}] + n_1, \qquad (3.23)$$

where the square brackets denote the integer part, and n_1 is an integer which depends on the accuracy required. The maximum value of k_z is fixed by the sampling rate of the measurement data along the z direction (i.e., $k_z^{max} = 0.5/\Delta z$).

In order to translate the fields to the planar aperture one first needs to calculate the coefficients of the modal expansion c_{n,k_z}. The modal expansion of (3.21) can also be seen
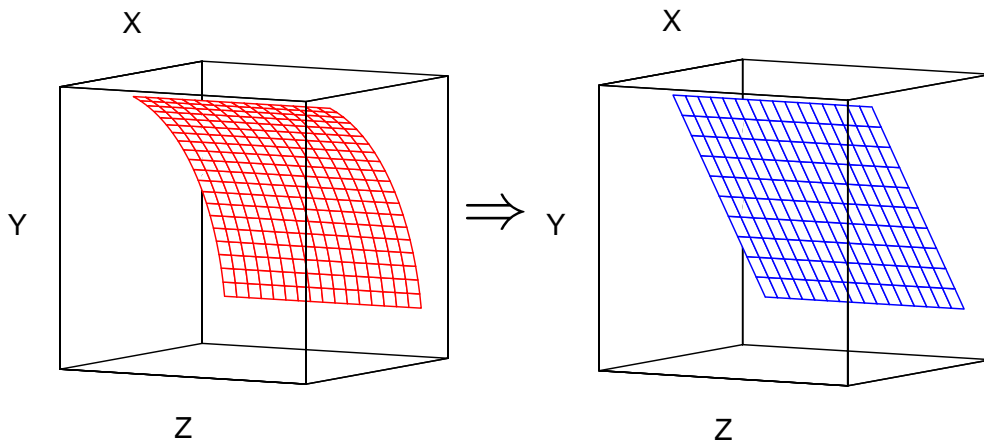
Figure 3.11. Geometry of the original cylindrical aperture and the final planar aperture.

as a 2-D Fourier series and therefore one can calculate the coefficients c_{n,k_z} as follows

$$c_{n,k_z} = \frac{1}{2\pi(z_{max} - z_{min})} \frac{1}{H_n^{(2)}(k_\rho \rho_a)} \int_{\phi_{min}}^{\phi_{max}} \int_{z_{min}}^{z_{max}} \psi(\rho_a, \phi, z)\, e^{-jk_z z}\, e^{-jn\phi}\, dz\, d\phi \quad (3.24)$$

In practice these coefficients are evaluated via a 2-D FFT of the measured backscatter data. Once the coefficients of the modal expansion c_{n,k_z} are calculated, then the fields can be translated to the planar aperture. Further details on the implementation of the fields translation are given in [90].

Concerning the position and dimensions of the planar aperture. Since it has to be as close as possible to the measurement cylinder, the coordinates of the corners of the planar aperture are chosen as follows:

$$\begin{aligned}
C_1 &= (\rho_a \cos\phi_{min},\ \rho_a \sin\phi_{min},\ z_{min}) \\
C_2 &= (\rho_a \cos\phi_{max},\ \rho_a \sin\phi_{max},\ z_{min}) \\
C_3 &= (\rho_a \cos\phi_{min},\ \rho_a \sin\phi_{min},\ z_{max}) \\
C_4 &= (\rho_a \cos\phi_{max},\ \rho_a \sin\phi_{max},\ z_{max})
\end{aligned} \quad (3.25)$$

3.3.2   Sampling criteria and resolution

The number of samples on the planar aperture will be fixed by the electrical dimensions of the target. Assuming the target is confined within a cube of dimensions $D_x \times D_y \times D_z$ and the acquired backscatter data are calibrated with a canonical target placed at the origin of the coordinates system, the sampling intervals needed to satisfy the Nyquist criterion are:

$$\Delta f \ \leq\ \frac{c}{2\sqrt{D_x^2 + D_y^2 + D_z^2}} \quad (3.26)$$

$$\Delta\phi \ \leq\ \frac{\lambda_{min}}{2\sqrt{D_x^2 + D_y^2}} \quad (3.27)$$

$$\Delta z \ \leq\ \frac{\rho_a\, \lambda_{min}}{2D_z} \quad (3.28)$$

where λ_{min} denotes the wavelength at the maximum working frequency. As expected, the required sampling rates increase with increasing electrical dimensions of the object.

Once the backscattered fields are translated to the planar aperture respecting the sampling criteria in (3.15)–(3.17), the formation of the 3-D reflectivity image becomes straightforward. One simply needs to apply the RMA to the translated fields on the

planar aperture. The resolutions in the resulting 3-D reflectivity image depend on the frequency bandwidth, the center frequency and the dimensions of the synthetic aperture. The resulting resolutions are given by:

$$\delta_x \simeq \frac{c}{2B} \tag{3.29}$$

$$\delta_y \simeq \frac{\lambda_c}{4\sin\left(\dfrac{\phi_{max} - \phi_{min}}{2}\right)} \tag{3.30}$$

$$\delta_z \simeq \frac{\lambda_c \, \rho_a}{2L_z} = \frac{c \, \rho_a}{2f_c L_z} \tag{3.31}$$

where L_z is the length of the 2-D synthetic aperture in the z-direction, and λ_c is the wavelength at the center frequency f_c.

In practice, the frequency domain backscatter data are windowed to lower the side-lobes in the imagery, and as a result, the final resolutions are usually slightly poorer than those given by (3.29)–(3.31).

3.3.3   Numerical simulations

Figure 3.12 shows a sketch of the geometry used in the first numerical simulation. The target consists of an ensemble of 27 point scatterers uniformly distributed inside a box of side 0.8 m. The scatterers form a mesh with a spacing of 40 cm. All scatterers have the same RCS: 0 dBsm. A Tx/Rx antenna synthesizes a cylindrical aperture of radius 2 m within the region $20° \leq \phi \leq 40°$ and $-1 \leq z \leq +1$ m. The sampling steps are $1°$ in ϕ,
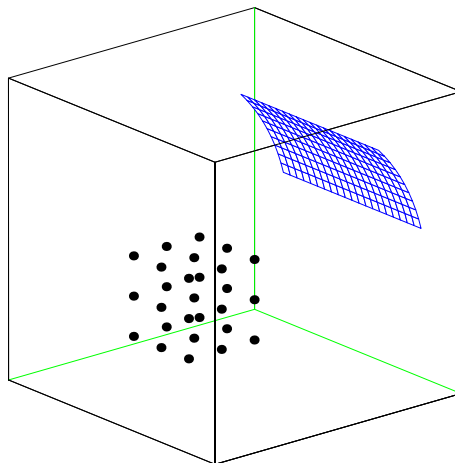
Figure 3.12.   Measurement set-up used in the numerical simulation with the ensemble of 27 point scatterers using a cylindrical aperture.

and 4 cm in the z-direction. The frequency ranges from 2 to 6 GHz, sampling a total of 41 points. The target is centered at the origin of the coordinates system. The number of cylindrical modes used is 201.

The range of validity and accuracy of the translation of 2-D backscattered fields are assessed in the Appendix B. An example of the fields translation from the cylindrical to the planar aperture is presented here. The translated fields have been compared with those that would be measured on the planar aperture (i.e., the exact ones). Figure 3.13 shows the modulus and the phase of the exact and translated fields along three linear cuts on the planar aperture: a line on the vertical plane $z = 0$ m; a horizontal line at the center of the aperture; and a second horizontal line close to the upper edge of the aperture. It can be observed that the agreement between the translated fields and the exact ones is excellent. Surprisingly, the accuracy in the phase is higher than that in the modulus. This result indicates that the distortion introduced in the imagery due to the field translation will be minimum. As expected, the minor discrepancies in the phase correspond to points where the modulus is small. Note that the higher errors observed close to the edges of the aperture will be mitigated after windowing the translated data on the planar aperture. Finally, it can be seen that the two horizontal cuts are symmetric with respect to the center, whereas those on the vertical plane $z = 0$ m are asymmetric. This is due to the oblique incidence used in the simulation. Similar results have been obtained in the spherical case, but they are not shown here due to space constraints.

Figure 3.14 shows the 3-D reflectivity image of the ensemble of 27 point scatterers used in the numerical simulation of the fields translation. The image was reconstructed inside a cube of side 1.2 m. The image has a total of $61 \times 61 \times 61$ voxel. A Kaiser-Bessel ($\alpha = 2$) window [87] was applied along the three dimensions of the frequency domain backscatter data. The displayed dynamic range is 30 dB. As expected, the image shows varying impulse responses for points in the near and far range due to the near field condition. Eventhough, all the scatterers are imaged at their actual positions, and the reflectivities are in agreement with the predicted ones. The data processing was performed on a Sun workstation with a 64 bit CPU and 128 MByte of RAM. The total processing time was approximately 4 min. Table 3.2 presents a breakdown of the computation time in order to gain an insight about the complexity for each processing step. Both the equalization and the coordinates transformation are optional steps, so they are not considered when adding up the total computation time. Note that the translation to the planar aperture entails less than a third of the total elapsed time. The internal memory required in this simulation was about 11 MByte. The RMA exhibits a dynamic range better than 80 dB when used with a planar scanning geometry [65]. In practice this means that the actual dynamic range of the images will be limited by the system noise. A second simulation

(a) $z = 0$ m (center)

(b) $y = 0.985$ m (center)
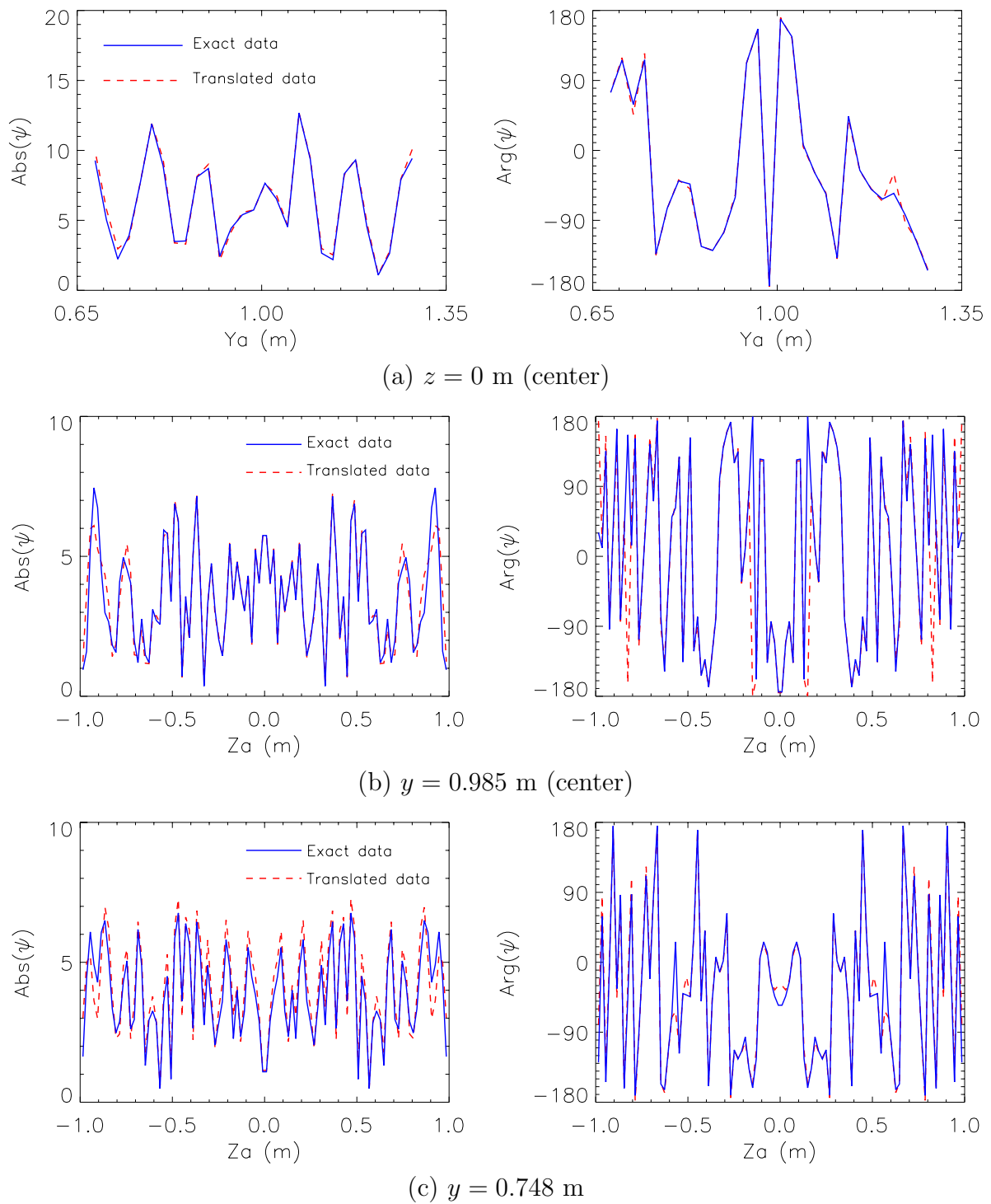
(c) $y = 0.748$ m

Figure 3.13. Comparison between the translated fields (red dashed line) and the exact ones (blue solid line) on the planar aperture. (a) Line at $z = 0$ m.; (b) Line at $y = 0.985$ m.; (c) Line at $y = 0.748$ m.
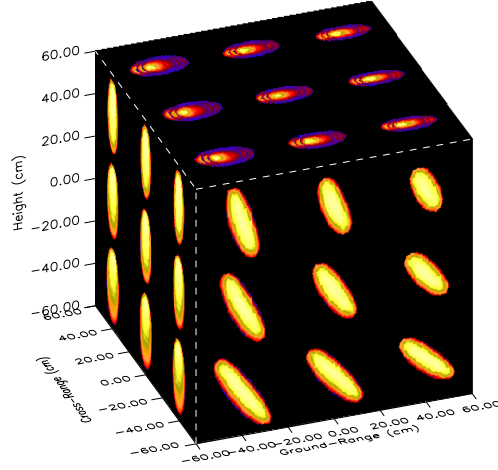
Figure 3.14. Projections of the 3-D SAR image onto the three main planes. Simulation of 27 point scatterers with a cylindrical aperture. Parameters: $\rho_a = 2$ m, $f = 2$–6 GHz, $\Delta f = 100$ MHz, $20° \leq \phi \leq 40°$, $\Delta\phi = 1°$, $L_z = 2$ m, $\Delta z_a = 4$ cm. The displayed dynamic range is 30 dB.

Table 3.2. Computational performance of the 3-D RMA with fields translation.

Processing Step	Time (s)
Frequency-Domain Data Load	0.36
Equalization (Optional)	54.31
Translation to a Planar Aperture	46.63
2-D Along-Track FFT	14.76
Matched Filter and Stolt Interpolation	53.53
3-D Final IFFT	60.09
Coordinates Transformation (Optional)	3.51
Total Elapsed Time	233.19
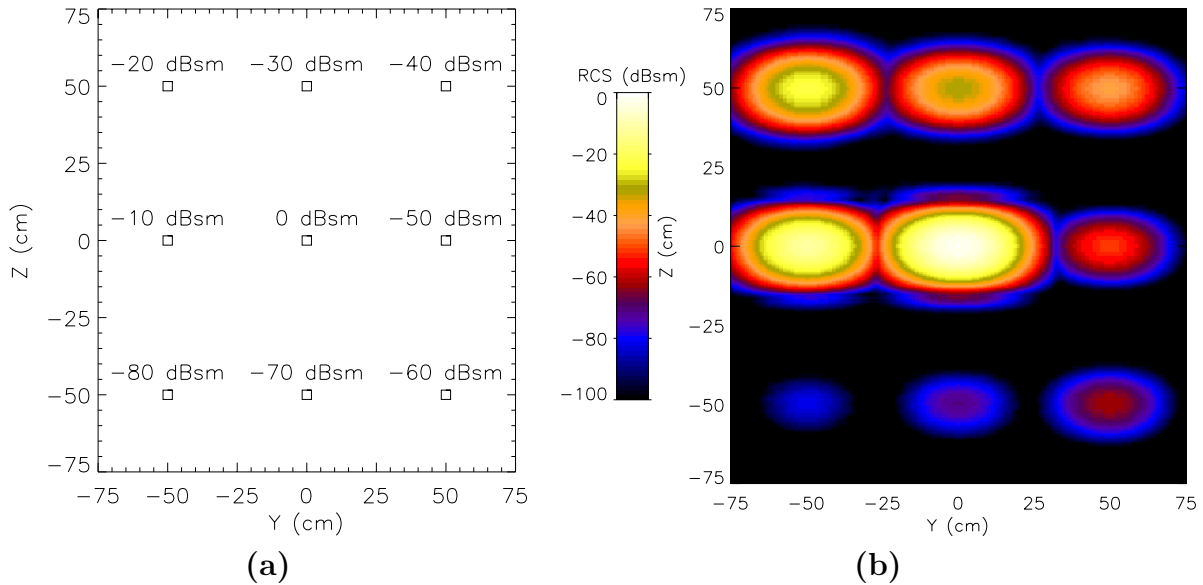
Figure 3.15. Target used to evaluate the dynamic range. (a) Nine points scatterers on the vertical plane $x = 0$ m (b) Vertical slice of the reflectivity image at $x = 0$ m.

to assess the dynamic range achieved with the cylindrical scanning geometry was carried out. The radius of the aperture was again 2 m. The region occupied by the aperture was $-15 \leq \phi \leq +15°$ and $-1 \leq z \leq +1$ m. The sampling steps in the ϕ and z directions were $1°$ and 2 cm, respectively. The frequency ranged from 2 to 6 GHz, sampling a total of 41 points. The target used consisted of three parallel planes as the one displayed in Figure 3.15 (a), uniformly spaced 50 cm in the ground-range direction or x-axis. On each plane there were 9 point targets with reflectivities ranging from 0 to –80 dBsm. The number of cylindrical modes used in the fields translation was 251. A four terms Blackman-Harris window (i.e., with side-lobes below –92 dB) [87] was applied along the three dimensions of the frequency domain backscatter data. Figure 3.15 (b) shows a vertical slice corresponding to the central plane. The displayed dynamic range is 100 dB. In this example, it can be seen that the distortion introduced by the fields translation is totally negligible.

3.3.4   Experimental results

The experimental results have been obtained using the anechoic chamber of the EMSL [60].

A sketch of the target is depicted in Figure 3.16, and a photograph is also shown in Figure 3.17. The target consisted of an arrangement of metallic spheres and trihedrals. The spheres had a diameter of 7.62 cm. There were two pairs of trihedrals reflectors with side length of 28 cm and 19.5 cm, respectively. The measurement was carried out in the

frequency range 6–10 GHz. The target positioner was moved along a total distance of 4 m. During the measurement the antennas covered the angular range $35° \leq \phi \leq 55°$. With these parameters the expected resolutions are 3.75 cm in ground-range, 4.4 cm in cross-range and 5.4 cm in height, respectively. The frequency domain backscatter data were acquired for two polarizations: HH and VV. The number of cylindrical modes used in the fields translation is 1050. The resulting 3-D reflectivity images for the two polarizations are shown in Figure 3.18. The image was reconstructed inside a box of dimensions 2 m×2 m×0.8 m, with 201×201×41 voxels. The displayed dynamic range is 60 dB.

The high quality of the reconstructed images confirms the accuracy of the proposed algorithm with a cylindrical scanning geometry. It is important to observe that all the spheres are clearly distinguishable on the three main projection planes with resolutions in agreement with the expected ones. On the other hand, the trihedrals exhibit a composite response: a high peak centered at the trihedral phase center and the backscatter due to the diffraction on the front edges. The peak value associated with the phase center is identical in the two polarizations. Instead, the edges are highly polarization dependent depending on their orientations. As an example, the HH images show horizontal segments with high reflectivity for all the trihedrals, whereas the other two edges of the front triangle do not show up. Moreover, the upper peak of the two large trihedrals is also present in the HH images. The horizontal edges have disappeared in the VV images, but the other edges are present now. Note that both edges of the trihedrals can be distinguished in the two
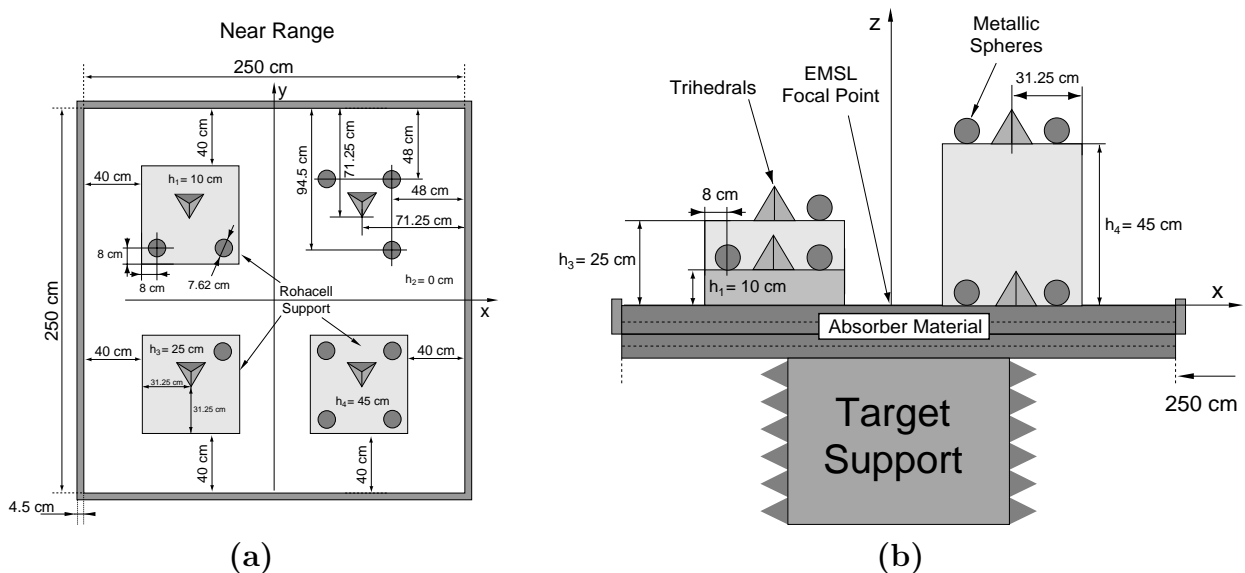
Figure 3.16. (a) Top view and (b) side view of a scheme of the target used in the experiment.
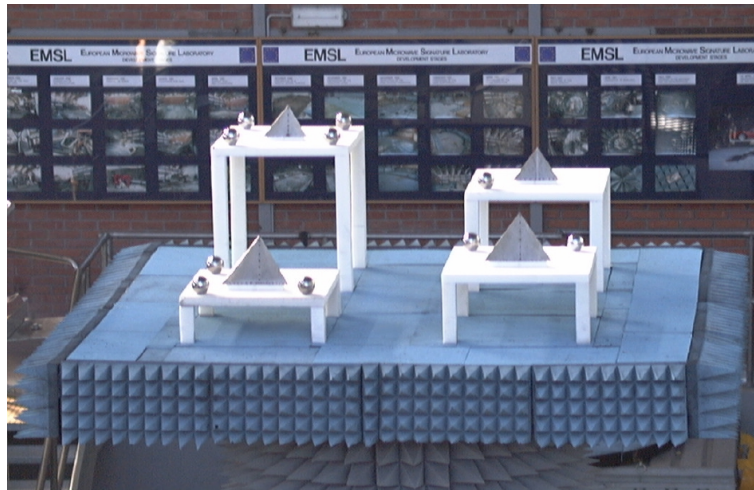
Figure 3.17. Photograph of the target used in the experiment.

large trihedrals, but only the external one is evident for the small trihedrals. The images are also accurate from the quantitative point of view. The retrieved RCS for the spheres and the trihedrals are in agreement with expected ones at the center frequency [88]. The spheres show an RCS of about –23 dBsm, and the trihedrals have 6.6 dBsm for the large ones and 0.3 dBsm for the small ones. The total processing time was only 1 hour. The part corresponding to the field translation entailed 40 minutes, and the RMA processing the remaining 20 minutes.

VV Polarization
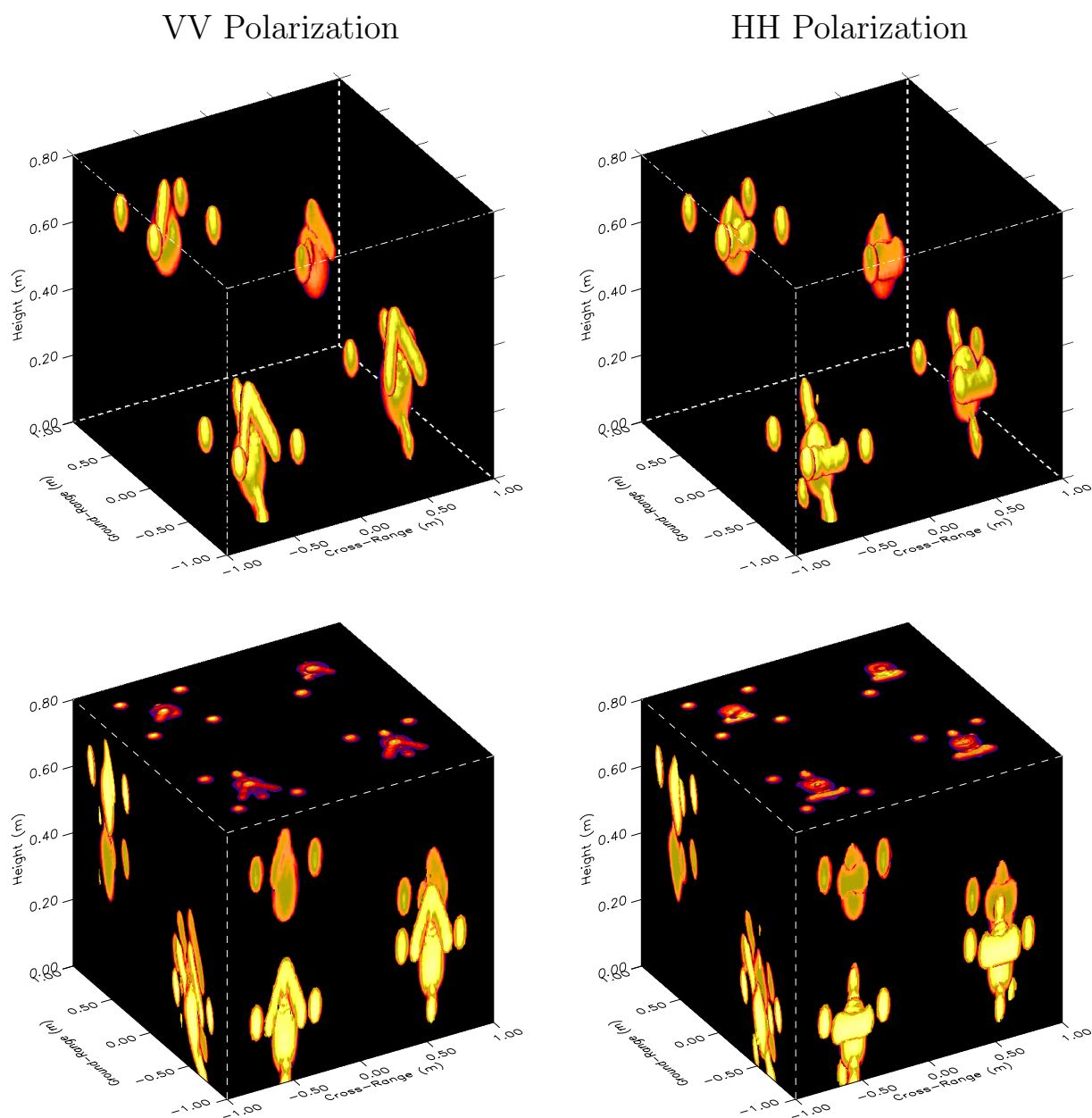
HH Polarization

Figure 3.18. Iso-surfaces (top) and projections (bottom) of the 3-D SAR image obtained in the experiment in the HH and VV polarizations. Parameters: $\rho_a = 9.56$ m, $f = 6$–10 GHz, $\Delta f = 40$ MHz, $35° \leq \phi \leq 55°$, $\Delta\phi = 0.5°$, $L_z = 4$ m, $\Delta z_a = 2.5$ cm. The displayed dynamic range is 60 dB.

3.4   Spherical scanning geometry

The field translation from a spherical to a planar aperture is conceptually identical to that of the cylindrical case. Further details on the practical implementation are given in [90]. The only differences appear as a consequence of the different coordinates system employed in the formulation, which now is spherical. As in the cylindrical case, the measured backscattered fields are assumed to be a solution of the 3-D scalar Helmholtz equation.

3.4.1   Fields translation

The frequency domain backscatter data are assumed to be acquired on the surface of a sphere with uniform sampling both in the azimuth and elevation angles within the ranges $\phi_{min} \leq \phi \leq \phi_{max}$ and $\theta_{min} \leq \theta \leq \theta_{max}$. The radius of the measurement sphere is r_a.

The general solution of the scalar Helmholtz equation can be expanded into a sum of spherical harmonics as follows [89]

$$\psi(r, \phi, \theta) = \sum_{n=0}^{N} \sum_{m=-n}^{n} c_{m,n} \, e^{jm\phi} \left(\frac{m}{|m|} \right)^m \overline{P}_n^m(\cos\theta) \, h_n^{(2)}(kr), \qquad (3.32)$$

where $h_n^{(2)}(\cdot)$ is the spherical Hankel function of second kind and integer order n, and $\overline{P}_n^m(\cdot)$ denotes the normalized associate Legendre function of first kind which is defined as

$$\overline{P}_n^m(\cos\theta) = \sqrt{\frac{2n+1}{2} \frac{(n-m)!}{(n+m)!}} \, P_n^m(\cos\theta). \qquad (3.33)$$
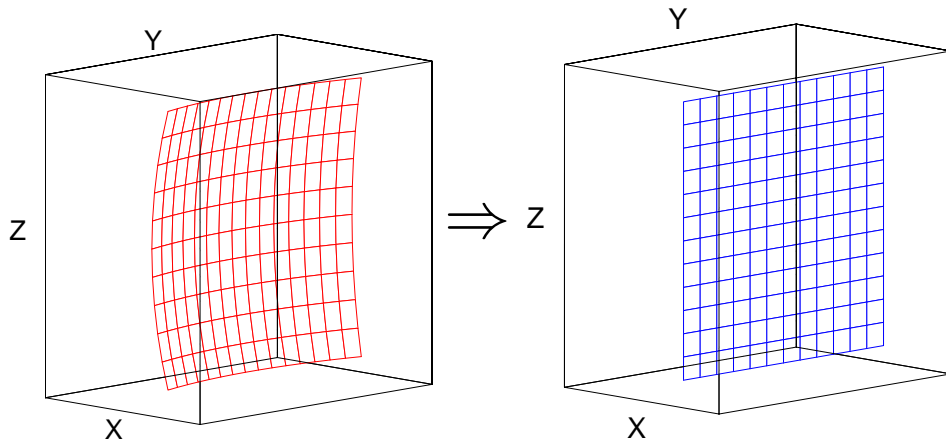
Figure 3.19. Geometry of the original spherical aperture and the final planar aperture.

$\overline{P}_n^m(\cdot)$ is an even function of m, i.e.

$$\overline{P}_n^m(\cos\theta) = \overline{P}_n^{(-m)}(\cos\theta), \tag{3.34}$$

and therefore m is considered to take only positive values. As suggested in [91], a factor $(m/|m|)^m$ is extracted from the coefficients in order to simplify its evaluation.

As in any modal expansion, the summations will be always truncated at $|n| \leq N$. The value of N will be fixed by the radius of the minimum sphere, concentric with the measurement sphere, that encloses entirely the target [91]. If the radius of the minimum sphere is r_{min}, the value of N is given by

$$N = [k\, r_{min}] + n_1, \tag{3.35}$$

where n_1 is fixed depending on the accuracy required.

Analytical evaluation of the coefficients $c_{m,n}$

The technique used to calculate the amplitudes of the spherical harmonics $c_{m,n}$ in (3.32) is based on that employed in near-field to far-field transformations of fields radiated by an antenna under test [91, Chapter 4]. Here only some minor modifications have been introduced in order to apply this technique to the scalar wave equation instead of the vector one. The method is based on the exploitation of orthogonality properties of both the exponential functions and the associate Legendre functions.

Under the hypothesis of validity of the "radiating reflectors" model [19], the backscattered fields measured at a single frequency on a sphere of radius $r = r_a$ can be expressed as a summation of spherical harmonics as follows

$$\psi(r_a, \phi, \theta) = \sum_{n=0}^{N} \sum_{m=-n}^{n} c_{m,n}\, e^{jm\phi} \left(\frac{m}{|m|}\right)^m \overline{P}_n^m(\cos\theta)\, h_n^{(2)}(kr_a), \tag{3.36}$$

where $(m/|m|)^m = 1$ for $m = 0$.

The harmonics amplitudes $c_{m,n}$ in (3.36) are calculated as follows. Let us rewrite (3.36) in the form of a Fourier series in ϕ, i.e.

$$\psi(r_a, \phi, \theta) = \sum_{m=-N}^{N} c_m(r_a, \theta)\, e^{jm\phi}, \tag{3.37}$$

where

$$c_m(r_a, \theta) = \sum_{n=|m|}^{N} c_{m,n} \left(\frac{m}{|m|}\right)^m \overline{P}_n^m(\cos\theta)\, h_n^{(2)}(kr_a). \tag{3.38}$$

Then the amplitudes of the Fourier harmonics $c_m(r_a, \theta)$ can be expressed as

$$c_m(r_a, \theta) = \frac{1}{2\pi} \int_0^{2\pi} \psi(r_a, \phi, \theta) e^{-jm\phi} \, d\phi. \tag{3.39}$$

In practice, the coefficients $c_m(r_a, \theta)$ are evaluated by means of an azimuth discrete Fourier transform of the measured backscattered fields $\psi(r_a, \phi, \theta)$.

Noting that (3.38) can be rewritten is this form

$$c_m(r_a, \theta) = \sum_{n=|m|}^{N} c_{m,n}(r_a) \left(\frac{m}{|m|} \right)^m \overline{P}_n^m(\cos\theta), \tag{3.40}$$

where

$$c_{m,n}(r_a) = c_{m,n} \, h_n^{(2)}(kr_a). \tag{3.41}$$

At this stage, one can obtain the coefficients $c_{m,n}(r_a)$ by making use of the orthogonality property of the normalized associate Legendre function [91] as follows

$$c_{m,n}(r_a) = \left(\frac{m}{|m|} \right)^m \int_0^{\pi} c_m(r_a, \theta) \, \overline{P}_n^m(\cos\theta) \sin\theta \, d\theta. \tag{3.42}$$

The amplitudes of the spherical harmonics are obtained through (3.41), i.e.

$$c_{m,n} = \frac{c_{m,n}(r_a)}{h_n^{(2)}(kr_a)}. \tag{3.43}$$

An algorithm for the efficient evaluation of the modal coefficients $c_{m,n}$ is given in Appendix C. As in the cylindrical case, the computation can be efficiently implemented via FFT codes. However, the computational cost of this solution is higher than that with the cylindrical aperture. Once the coefficients of this modal expansion are derived, then the field can be translated to a planar aperture in the vicinity of the spherical aperture.

Position and dimension of the planar aperture

In relation to the position and dimension of the planar aperture. It is defined as the largest rectangular aperture within the trapezoid defined by the following four points:

$$\begin{aligned}
C_1 &= (r_a \cos\phi_{min} \sin\theta_{min}, \; r_a \sin\phi_{min} \sin\theta_{min}, \; r_a \cos\theta_{min}) \\
C_2 &= (r_a \cos\phi_{max} \sin\theta_{min}, \; r_a \sin\phi_{max} \sin\theta_{min}, \; r_a \cos\theta_{min}) \\
C_3 &= (r_a \cos\phi_{min} \sin\theta_{max}, \; r_a \sin\phi_{min} \sin\theta_{max}, \; r_a \cos\theta_{max}) \\
C_4 &= (r_a \cos\phi_{max} \sin\theta_{max}, \; r_a \sin\phi_{max} \sin\theta_{max}, \; r_a \cos\theta_{max})
\end{aligned} \tag{3.44}$$

3.4.2   Sampling criteria and resolution

Assuming the target is confined within a cube of dimensions $D_x \times D_y \times D_z$ and the acquired data are calibrated with a canonical target placed at the origin of the coordinates system, the sampling intervals needed to satisfy the Nyquist criterion can be expressed as follows:

$$\Delta f \quad \leq \quad \frac{c}{2\sqrt{D_x^2 + D_y^2 + D_z^2}} \tag{3.45}$$

$$\Delta \phi \quad \leq \quad \frac{\lambda_{min}}{2\sqrt{D_x^2 + D_y^2}} \frac{1}{\sin \theta_{max}} \tag{3.46}$$

$$\Delta \theta \quad \leq \quad \frac{\lambda_{min}}{2\sqrt{D_x^2 + D_y^2 + D_z^2}} \tag{3.47}$$

where λ_{min} denote the wavelength at the maximum working frequency.

The resolutions in the resulting 3-D reflectivity image depend on the frequency bandwidth, the center frequency and the dimensions of the synthetic aperture in the following form:

$$\delta_x \quad \simeq \quad \frac{c}{2B \sin \theta_{min}} \tag{3.48}$$

$$\delta_y \quad \simeq \quad \frac{\lambda_c}{4 \sin \left(\dfrac{\phi_{max} - \phi_{min}}{2} \right) \sin \theta_{min}} \tag{3.49}$$

$$\delta_z \quad \simeq \quad \frac{\lambda_c}{2 \left(\cos \theta_{min} - \cos \theta_{max} \right)} \tag{3.50}$$

where λ_c is the wavelength at the center working frequency.

3.4.3   Numerical simulations

The last numerical simulation has been performed using a spherical aperture. The target is that in Figure 3.14. The Tx/Rx antenna now synthesizes an spherical aperture with radius 2 m. The angular ranges in azimuth and elevation are $0° \leq \phi \leq 20°$ and $75° \leq \theta \leq 90°$, respectively. The corresponding angular steps are both $1°$. As in the previous simulation, the frequency ranges from 2 to 6 GHz with a step of 100 MHz. The number of spherical modes used in the fields translation is 213. The resulting 3-D reflectivity image is shown in Figure 3.20. The image has a total of $61 \times 61 \times 61$ voxels. A Kaiser-Bessel ($\alpha = 2$) window [87] has been applied along the three dimensions of the frequency domain backscatter data. The displayed dynamic range is 30 dB. It can be observed that
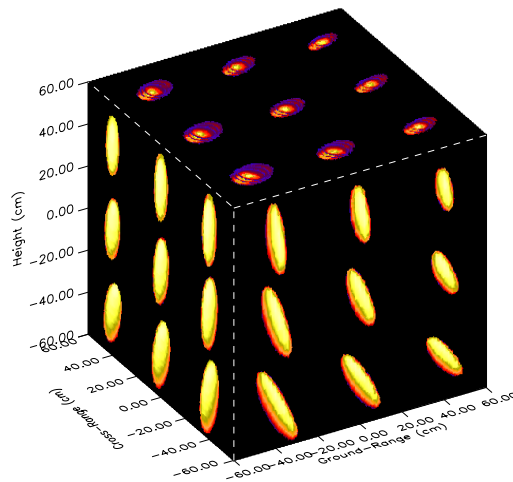
Figure 3.20. Projections of the 3-D SAR image onto the three main planes. Simulation with 27 point scatterers using a spherical aperture. Parameters: $r_a = 2$ m, $f = 2$–6 GHz, $\Delta f = 100$ MHz, $0° \leq \phi \leq 45°$, $60° \leq \theta \leq 75°$, $\Delta\phi = \Delta\theta = 1°$. The displayed dynamic range is 30 dB.

the quality of the image is remarkable, thus demonstrating the validity of the presented technique. As predicted, the computational load associated with the translation is higher than that in the cylindrical case.

3-D Near-Field Radar Imaging of Targets Electrically Large

4.1 Introduction

The practical problem motivating the development of the imaging techniques presented in this Chapter was the formation of a 3-D near-field SAR image of a 5 m high Fir tree [67]. This tree was measured in the anechoic chamber of the EMSL using the spherical scanning geometry [60]. The use of the imaging algorithm presented in Chapter 3 (i.e., the backpropagation of the backscatter data to a planar aperture followed by the focusing with the range migration algorithm) was discarded because of the large electrical dimensions of the tree. As indicated in Section 3.4.1, the number of spherical harmonics to be used in the fields translation is an increasing function of the electrical dimensions of the target, i.e.

$$N \simeq \frac{4\pi f_{\max}}{c} \, r_{\max} \tag{4.1}$$

In this measurement, the radius of the minimum sphere enclosing the entire tree $r_{\max}$ was 4 m, and the maximum frequency was 5.5 GHz. The resulting minimum number of spherical harmonics is $N \simeq 922$. In practice, the computation of the normalized associate Legendre function of orders above 200 becomes extremely difficult as the maximum values reached cannot be treated with double precision (8 byte) floating point numbers [92, 93]. Note that with 922 spherical modes the normalized associate Legendre function can reach values over 10^{+1725}. This limitation can be circumvented by using long double (16 byte) numbers instead. However, it has been observed that the calculations with these type of floating point numbers slow down the execution of the code dramatically. Further, some functions in the standard libraries of the compiler cannot be called with long double arguments. Thus, the development of a code implementing the fields translation with such

a large number of spherical harmonics has been postponed until a practical solution to the above-mentioned problems is found.

This chapter presents two imaging algorithms which are specially suited for forming 3-D near-field SAR images of targets electrically large. For both algorithms the synthetic aperture is assumed to have a spherical shape. The use of these imaging algorithms with cylindrical and planar apertures is not addressed here.

The first imaging algorithm uses a near-field focusing function which accounts for the wavefront curvature and the propagation losses [58]. The spatial distribution of the target reflectivity is estimated by means of an azimuth convolution between this near-field focusing function or space-variant matched filter and the frequency domain backscatter data, followed by a coherent integration over the frequency band and the synthetic aperture in elevation. The circular convolution in azimuth is performed by employing FFT codes, thus reducing drastically the computational cost. Moreover, instead of using a DFT, the focusing function in the azimuth wavenumber domain is evaluated through an asymptotic expansion obtained by means of the MSP. This asymptotic expansion is further optimized by using working matrices with the points of stationary phase and their second order derivatives.

The second imaging algorithm is basically the 3-D PFA [48, 94] (i.e., an algorithm to be used under the far-field condition) followed by a geometric rectification of the image. The resulting geometric distortion due to the short observation distance or near-field condition is corrected by applying the rectification algorithm. It is important to note that the rectification algorithm is only effective when the angular span of the synthetic aperture is limited [49]. This limitation must be kept in mind when using this technique. On the other hand, the computational cost of this solution is minimum. This algorithm is specially tailored to be employed as a quick-look SAR processor. High quality imagery will only be obtained with narrow spans of the two aspect angles.

This Chapter is organized as follows. In Section 4.2, the imaging algorithm with the space-variant matched filter is presented providing details about its formulation using the MSP, the processing steps involved, the spatial resolutions achieved, the sampling intervals, the numerical simulations and the measurements. Section 4.3 introduces the PFA with the 3-D image rectification. This algorithm is successfully tested both with synthetic and experimental data.

The focusing of the tree data with the first algorithm is entirely addressed in Chapter 5. Here, the experimental results obtained in the measurement of the Fir tree have uniquely been used to test the second algorithm.

4.2   A 3-D SAR algorithm using a space-variant matched filter

4.2.1   Formulation of the problem

The imaging geometry is shown in Figure 4.1. A CW signal is radiated from an antenna, located at a distance R_a from the center of the coordinates system, with a beamwidth sufficiently large to uniformly irradiate a 3-D target. The reflected signal is received by a similar adjacent antenna. The object is positioned on a low reflectivity platform which rotates about the z-axis. The antenna system rotates in the $y - z$ plane forming an angle θ with the z-axis. Thus, the backscattered fields $E_s(f, \phi, \theta)$ are acquired as a function of three parameters: the frequency f of the CW signal, the azimuth position of the rotating platform ϕ, and the looking angle of the antenna system θ. Considering that the antenna is located within the near-field region of the object (i.e., it illuminates the object with a spherical wavefront), and its radiation pattern introduces a negligible distortion, then the 3-D complex reflectivity image in cylindrical coordinates $I(\rho, \phi, z)$ can be written as follows (see [41] and Chapter 2),

$$I(\rho, \phi, z) = \frac{8}{c^3} \int_f f^2 df \int_\theta \sin\theta d\theta \int_{\phi'} E_s(f, \phi', \theta) \, F(\rho, \phi - \phi', z; f, \theta) \, d\phi' \qquad (4.2)$$
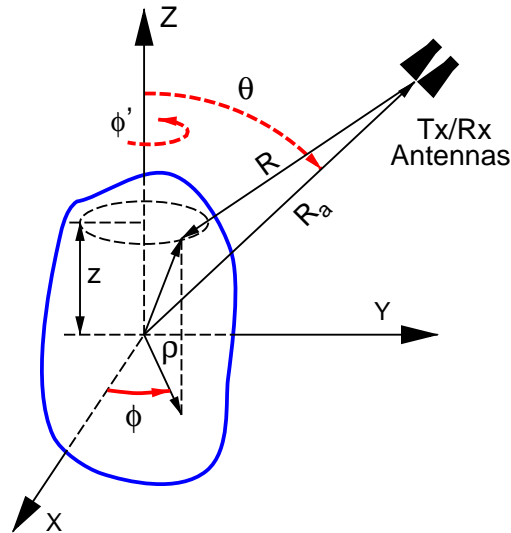
Figure 4.1.   Imaging geometry with the 3-D target.

where $F(\cdot)$ is a near-field focusing function (or space-variant matched filter) which can be expressed as,

$$F(\rho, \phi, z; f, \theta) = (\frac{R}{R_a})^2 \exp\left[jk(R - R_a)\right] \tag{4.3}$$

$$R = \sqrt{R_a^2 + \rho^2 + z^2 - 2R_a\left[\rho \sin\theta \cos\phi + z \cos\theta\right]} \tag{4.4}$$

where R denotes the range to the point with coordinates (ρ, ϕ, z), R_a is the range to the center of the coordinates system and zero-phase reference point, and k is the frequency wavenumber. Here the frequency wavenumber is defined as $k = 4\pi f/c$. In (4.2), both the exact near-field phase history and the free-space propagation losses are accounted for by the exponential function and the quadratic term in the amplitude, respectively. It is important to note that the focusing function $F(\cdot)$ is defined only by the measurement geometry and the working frequency. Thus, if calculated once and stored on memory, $F(\cdot)$ could be reused with different data sets measured under the same conditions. This is the case of a fully polarimetric measurement, where four data sets have to be focused using identical processing parameters. The core of this algorithm resides in the calculation of the circular convolution in (4.2). A description of the approach followed in the algorithm implementation is next.

4.2.2   Imaging algorithm

The circular convolution in azimuth in (4.2) can be calculated using FFT codes. In the simplest form, it requires the use of 1-D DFT and a complex product in the azimuth wavenumber domain k_ϕ. Instead of using a DFT, the azimuth Fourier transform of the focusing function $\mathcal{F}(\cdot)$ may be evaluated by using the MSP [95]. This approach has the advantage of giving as a result an analytical expression, the evaluation of which can be highly optimized by using working matrices containing the points of stationary phase and their second order derivatives. Furthermore, the number of points in the azimuth wavenumber domain does not need to be a power of two, thus alleviating the memory requirements and speeding-up the code.

The azimuth Fourier transform of the focusing function $\mathcal{F}(\cdot)$ is given by

$$\mathcal{F}(\rho, k_\phi, z; f, \theta) = \int_{-\pi}^{\pi} \left(\frac{R(\phi)}{R_a}\right)^2 \exp\left[j\, p(\phi)\right]\, d\phi \tag{4.5}$$

where,

$$p(\phi) = A\left[R(\phi) - R_a\right] - k_\phi\, \phi \tag{4.6}$$

$$R(\phi) = \sqrt{B - C \cos\phi} \tag{4.7}$$

and

$$
\begin{aligned}
A &= k \\
B &= R_a^2 + \rho^2 + z^2 - 2R_a z \cos\theta \\
C &= 2R_a \rho \sin\theta
\end{aligned}
\tag{4.8}
$$

Since the integrand in (4.5) has no singular points and is a highly oscillating function, the integral can be evaluated by means of the MSP provided that A is sufficiently large.

Assuming a sampling rate consistent with the Nyquist criterion, the DFT of the focusing function may be expressed as,

$$
\mathcal{F}(\rho, k_\phi, z; f, \theta) = \sum_{n=-N_\phi/2}^{N_\phi/2-1} \left(\frac{R(n\,\Delta\phi)}{R_a} \right)^2 \exp\left[j\, p(n\,\Delta\phi) \right] \, \Delta\phi
\tag{4.9}
$$

$$
k_\phi = \left\{ -\frac{N_\phi}{2}, -\frac{N_\phi}{2} + 1, \ldots, \frac{N_\phi}{2} - 1 \right\}
$$

$$
\Delta\phi = \frac{2\pi}{N_\phi}, \quad N_\phi \text{ even}
$$

The asymptotic evaluation of this DFT with the method of the stationary phase gives the following result (see Appendix D for further details),

$$
\begin{aligned}
\mathcal{F}(\rho, k_\phi, z; f, \theta) \simeq \frac{\sqrt{j\,2\pi}}{R_a^2} &\left\{ \frac{R^2(\phi_-)}{\sqrt{p''(\phi_-)}} \exp\left[j\, p(\phi_-) \right] + \right. \\
&\left. \frac{R^2(\phi_+)}{\sqrt{p''(\phi_+)}} \exp\left[j\, p(\phi_+) \right] \right\}, \quad \text{if } k_\phi \leq \hat{k}_\phi, \text{ and}
\end{aligned}
\tag{4.10}
$$

$$
\begin{aligned}
\mathcal{F}(\rho, k_\phi, z; f, \theta) \simeq 2\pi \left(\frac{R(\phi_o)}{R_a} \right)^2 &\exp\left[jp(\phi_o) \right] \left(\frac{2}{|p'''(\phi_o)|} \right)^{(1/3)} \times \\
&Ai\left(-\left[\frac{2}{|p'''(\phi_o)|} \right]^{(1/3)} p'(\phi_o) \right), \quad \text{if } k_\phi > \hat{k}_\phi
\end{aligned}
\tag{4.11}
$$

with

$$
\hat{k}_\phi = |p'''(\phi_o)| - \left(\frac{|p'''(\phi_o)|}{2} \right)^{(1/3)}
\tag{4.12}
$$

and wherein $Ai(\cdot)$ denotes the Airy function [92]. In (4.10), the asymptotic evaluation of the integral in (4.5) is performed by summing the contribution from two stationary phase points at $\phi = \{\phi_+, \phi_-\}$. In (4.11), the major contribution to the integral in (4.5) comes

from a small neighborhood near the point $\phi = \phi_o$. In this neighborhood, the second order derivative $p''(\phi)$ vanishes and

$$p(\phi) \simeq p(\phi_o) + p'(\phi_o)\,(\phi - \phi_o) + p'''(\phi_o)\,\frac{(\phi - \phi_o)^3}{3!} \qquad (4.13)$$

Substituting $p(\phi)$ with this series expansion, the integral in (4.5) can be expressed in terms of the Airy function, leading to (4.11).

If $C \ll B$, i.e. the reflectivity is being estimated at points close to the origin of the coordinates system, then Equations (4.10) and (4.11) reduce to a much simpler form and $\mathcal{F}(\cdot)$ may be expressed as follows

$$\mathcal{F}(\rho, k_\phi, z; f, \theta) \simeq 2\pi\,J_{k_\phi}(\eta)\,\exp\left[-j(kR_a + k_\phi\frac{\pi}{2})\right] \qquad (4.14)$$

wherein $\eta = A\sqrt{B}/2$ and $J_{k_\phi}(\cdot)$ denotes the Bessel function of integer order k_ϕ.

Once $\mathcal{F}(\cdot)$ has been calculated for each working frequency f and antenna looking angle θ, the reflectivity image in cylindrical coordinates is recovered from the measured data in the azimuth wavenumber domain as

$$I(\rho, \phi, z) = \frac{8}{c^3}\,\mathsf{IFFT}_{k_\phi}\left[\sum_f f^2 \sum_\theta \sin\theta\,\,\mathsf{FFT}_\phi[E_s(f, \phi, \theta)] \times [\mathcal{F}]_{k_\phi}\right]\Delta f\,\Delta\theta\,\Delta\phi \qquad (4.15)$$

with $[\mathcal{F}]_{k_\phi} = \mathcal{F}(\rho, k_\phi, z; f, \theta)$ for $k_\phi = -\frac{N_\phi}{2}, -\frac{N_\phi}{2} + 1, \ldots, \frac{N_\phi}{2} - 1$.

In (4.15), the evaluation of the near-field focusing function in the azimuth wavenumber domain $[\mathcal{F}(\cdot)]_{k_\phi}$ is associated with most of the computational burden of the algorithm. What follows is a description of the computational procedure used in the implementation of the proposed imaging algorithm.

4.2.3   Computational procedure

The near-field 3-D SAR algorithm presented in Section 4.2.2 may be very demanding in terms of computer power and memory requirements, especially when the object being imaged is electrically large. In order to reduce the computational burden, the circular convolution in azimuth in (4.2) has been implemented with a complex product in the azimuth wavenumber domain. The focusing function $\mathcal{F}(\cdot)$ is evaluated by means of the asymptotic expansions in Equations (4.10), (4.11) and (4.14). This is basically the core of this imaging algorithm, which is the most computer intensive part of the code. The implementation of the first asymptotic expansion may be reduced to reading and interpolating two lookup tables or working matrices with the values of $p(\phi_\pm)$ and $p''(\phi_\pm)$ as a function of two
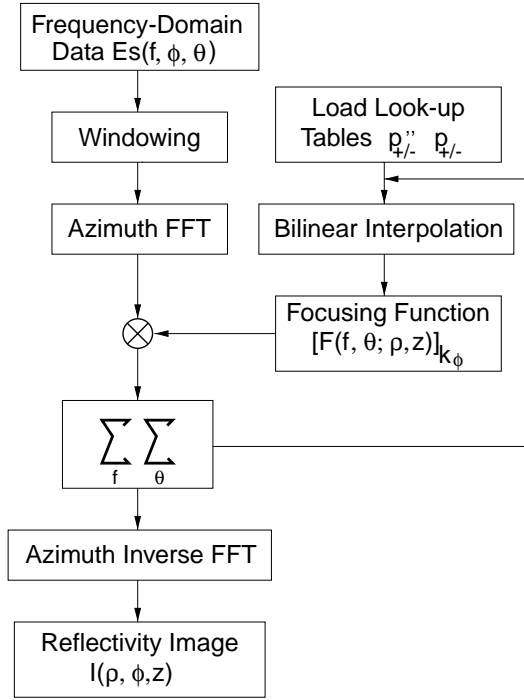
Figure 4.2. Flowchart of the near-field 3-D SAR algorithm.

parameters: α and β. Given these two look-up tables with $N_\alpha \times N_\beta$ uniformly located samples, the interpolated values may be calculated by using a bilinear interpolation [92]. The second and third asymptotic expansions are of much simpler implementation and can be directly introduced into the code.

The computational procedure for reconstructing a 3-D reflectivity image on the basis of (4.2) may be presented in the form of the following steps (see flow chart in Figure 4.2):

Step 1: Window the frequency-domain data with the desired weighting function. In the case of an inverse SAR measurement with the entire rotation of the object, no azimuth window is applied.

Step 2: Calculate a 1-D FFT in azimuth for each frequency and antenna looking angle. As a result, a 3-D array of complex values is obtained.

Step 3: Create the two look-up tables with the values of $\{p(\phi_-), p(\phi_+)\}$ and $\{p''(\phi_-), p''(\phi_+)\}$ as a function of α and β on a rectangular grid with $N_\alpha \times N_\beta$ points. The useful
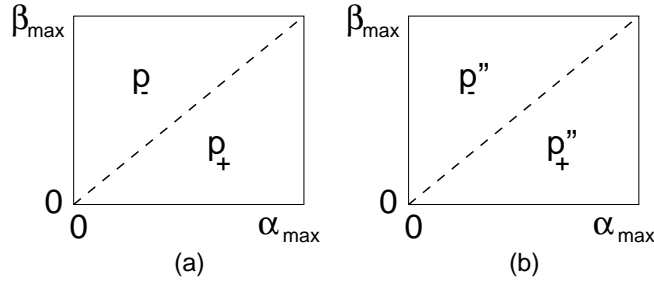
Figure 4.3. Look-up tables: (a) $p_{\pm}(\alpha, \beta)$ and (b) $p''_{\pm}(\alpha, \beta)$.

ranges for α and β are given by

$$0 \leq \;\; \beta \;\; \leq \beta_{\max} = \max_{(\rho, z, \theta)} \left[\frac{2R_a \rho \sin\theta}{R_a^2 + \rho^2 + z^2 - 2R_a z \cos\theta} \right] \tag{4.16}$$

$$0 \leq \;\; \alpha \;\; \leq \alpha_{\max} = \frac{\sqrt{1 - \sqrt{1 - \beta^2}}}{2} \tag{4.17}$$

From (4.17), it follows that $\alpha_{\max} \leq \beta$. Thus, a single 2-D float array split into two triangular sub-arrays can be used to store the pairs $\{p(\phi_-), p(\phi_+)\}$ and $\{p''(\phi_-), p''(\phi_+)\}$, as shown in Figure 4.3.

Step 4: Use bilinear interpolation [92] to calculate the focusing function in the azimuth wavenumber domain. Alternatively, if the sampling intervals $\Delta\alpha$ and $\Delta\beta$ are small enough, a nearest neighbor interpolation can be used without significant truncation errors.

Step 5: Calculate the complex product of the near-field focusing function and the measurement data in the azimuth wavenumber domain.

Step 6: Coherent summation over the antenna looking angle and frequency measured ranges for all pairs (ρ, z) repeating steps 4 and 5.

Step 7: IFFT in azimuth. As a result, the 3-D reflectivity image in cylindrical coordinates $I(\rho, \phi, z)$ is obtained.

4.2.4 Resolution and sampling criteria

In the resulting 3-D complex reflectivity image, the resolutions in ground-range and cross-range depend on the frequency bandwidth and the angular extent of the synthetic aperture

in azimuth, respectively. Thus

$$\delta_x = \frac{\lambda_c}{4 \sin\left(\dfrac{W_\phi}{2}\right) \sin\theta} \tag{4.18}$$

$$\delta_y = \frac{c}{W_f \sin\theta} \tag{4.19}$$

where W_ϕ denotes the angular extent in azimuth, W_f is the frequency bandwidth and λ_c is the wavelength at the center working frequency. When the SAR measurement is performed with the entire rotation of the object, equivalent to synthesizing a circular aperture which completely surrounds the object, resolutions in cross-range and ground-range coincide and reach their maximum limit which is approximately $\lambda/5$ [11]. The resolution in height depends on the angular extent in elevation and is given by

$$\delta_z = \frac{\lambda_c}{2 \left(\cos\theta_{\min} - \cos\theta_{\max}\right)} \tag{4.20}$$

Assuming the object is confined within a rectangular box of dimensions $D_x \times D_y \times D_z$ and the acquired data are calibrated with a canonical target placed at the origin of the coordinates system, the sampling intervals needed to satisfy the Nyquist criterion can be expressed as follows:

$$\Delta f \leq \frac{c}{2\sqrt{D_x^2 + D_y^2 + D_z^2}} \tag{4.21}$$

$$\Delta\phi \leq \frac{\lambda_{\min}}{2\sqrt{D_x^2 + D_y^2}} \frac{1}{\sin\theta_{\max}} \tag{4.22}$$

$$\Delta\theta \leq \frac{\lambda_{\min}}{2\sqrt{D_x^2 + D_y^2 + D_z^2}} \tag{4.23}$$

where $\lambda_{\min}$ denote the wavelength at the maximum working frequencies, respectively. As expected, the required sampling rates increase with increasing electrical dimensions of the object.

4.2.5   Experimental results

All results have been obtained on a high performance Sun workstation, equipped with a 64 bit CPU and 128 MByte of RAM. What follows is the description of the measurement set-ups and the results on simulated and experimental data sets.
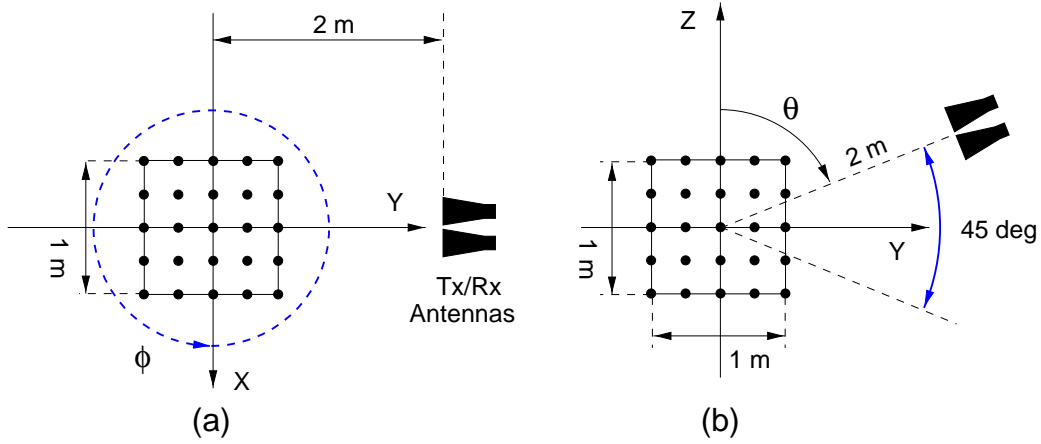
Figure 4.4. Measurement set-up used in the numerical simulation with the 3-D array of 125 point scatterers: (a) top view and (b) side view.

Numerical simulations

The target used in this numerical simulation consisted of a 3-D ensemble of $5 \times 5 \times 5$ point scatterers uniformly distributed within a box of 1 m^3, as shown in Figure 4.4. The range to the center of the coordinates system was $R_a = 2$ m. The RCS of all the scatterers was set 0 dBsm. This target was imaged in the frequency range 2 to 6 GHz, sweeping 51 frequency points spaced 80 MHz. A full rotation of the target about the z-axis, with 360 azimuth points and a step of 1 deg, was used. The antenna looking angle θ ranged from 67.5 to 112.5 deg, with 46 antenna positions spaced 1 deg. A 3-D SAR image was reconstructed using the presented near-field SAR algorithm. The projections of this 3-D image onto the $x - y$, $x - z$ and $y - z$ planes are shown in Figure 4.5. The array dimensions used in this reconstruction is $N_\rho = 85$, $N_\phi = 360$ and $N_z = 121$. This requires approximately 30 MByte of internal storage. The overall processing time is 3 h. 20 min. The processing time using a DFT code, and not the proposed asymptotic evaluation, for the azimuth Fourier transform of the focusing function is 12 h 13 min. Figures 4.6-(a1)-(a5) show five horizontal slices extracted from the 3-D complex reflectivity image. These slices correspond to the five horizontal planes where the point scatterers are uniformly distributed. For comparison, reconstructions using both the proposed near-field technique and a far-field algorithm (i.e., an interpolation followed by a 3-D inverse DFT, as described in Section 4.3.2) are shown in Figures 4.6 (b1)-(b5). Here, range curvature aberrations introduced by not using the exact phase history term in the focusing function $F(\cdot)$ are evident. Figure 4.7 depicts the cross-range, ground-range and height profiles from the 3-D image generated with the near-field algorithm. As expected, resolutions in cross-range and ground range are both approximately 1 cm. The height resolution is about 6 cm. A

Kaiser-Bessel window ($a = 2$) [87] across the aperture in elevation and across frequency is used. These resolutions as well as the reflectivity values at the position of the point scatterers are all in agreement with the predicted ones.

Experimental results

The presented near-field SAR algorithm has been tested experimentally using the anechoic chamber of the EMSL [60]. Two series of test measurements were performed.

The first measurement set-up consisted of a planar array of 49 metallic spheres forming an "S" shape, as shown in Figure 4.8 (a). The spheres were laid on top of a low reflectivity platform of 2.5×2.5 m². All spheres had a diameter of 7.62 cm. The range to the center of the coordinates system was R_a= 9.56 m. The backscattered fields in the HH polarization were acquired in the stepped frequency mode of the HP-8510 VNA within the frequency range 8 to 12 GHz, sweeping 801 frequency points spaced 5 MHz. A full rotation of the target about the z-axis, with 1200 azimuth positions and an angular step of 0.3 deg, was used. This was a pure 2-D SAR measurement, and no aperture synthesis in elevation was used. Therefore, no spatial resolution in height can be achieved. The antenna looking angle is kept fixed to 45 deg. Once the frequency data set was calibrated, gated in the time domain to isolate the response of the target, the number of frequency points used in the subsequent processing was decimated by a factor of 8, which still was above the Nyquist sampling rate defined by the target size and measurement geometry. Figure 4.8 (b) shows the image obtained with the presented near-field SAR algorithm. As expected, resolutions
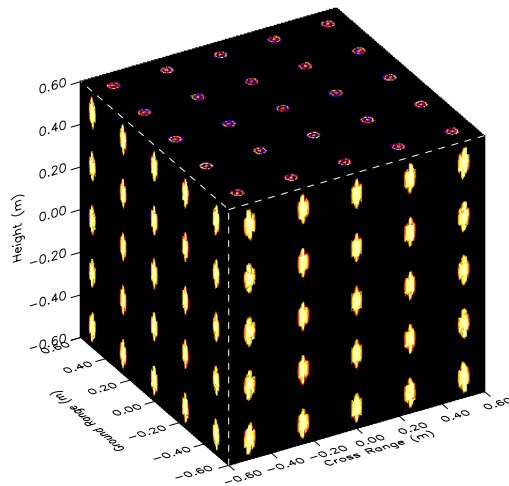
Figure 4.5. Projections of the 3-D SAR image onto the $x - y$, $x - z$ and $y - z$ planes obtained in the numerical simulation with the 3-D array of 125 point scatterers.
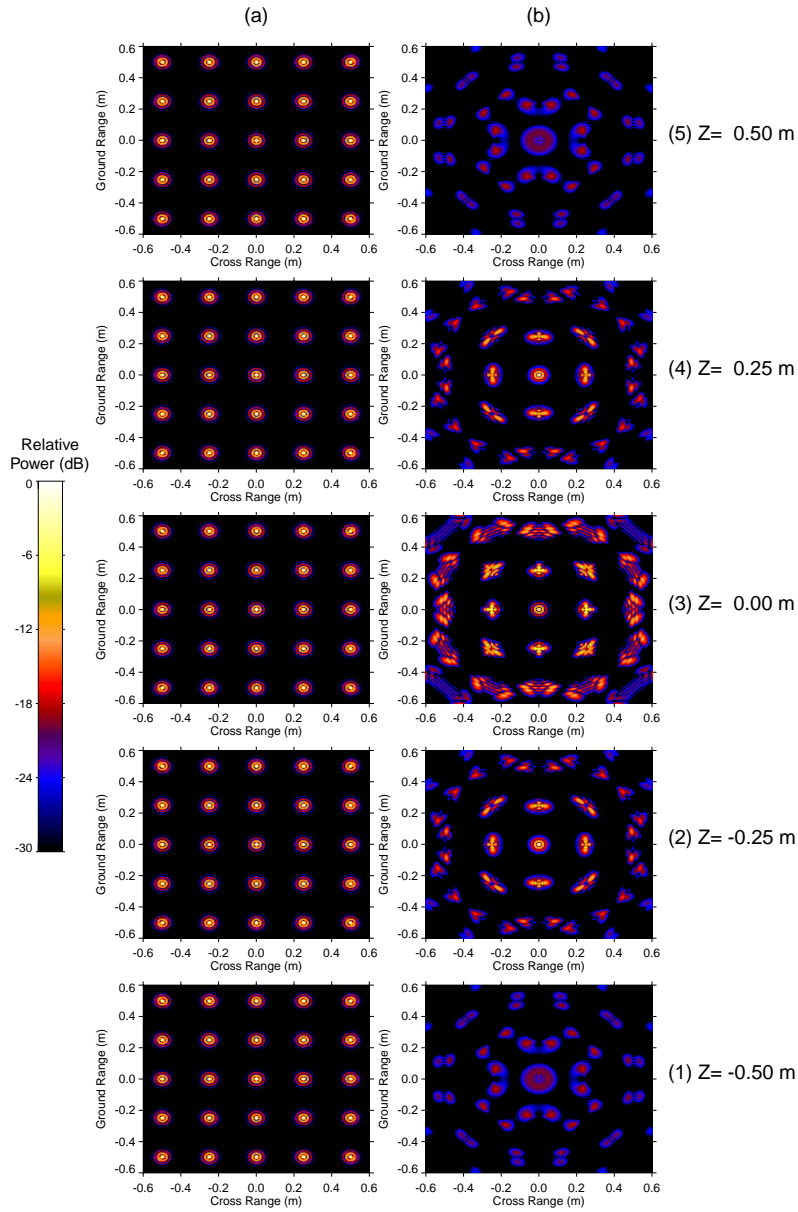
Figure 4.6. Horizontal slices from the 3-D reflectivity image obtained in the numerical simu-
lation using the near-field (a) and far-field (b) algorithms.

in cross-range and ground range are both approximately 5 mm. A Kaiser-Bessel window
($a = 2$) across frequency was used. The overall processing time was 1 min. The processing
time using a DFT code, and not the proposed asymptotic evaluation, for the azimuth
Fourier transform of the focusing function was 4 min. For comparison, this image is
shown along with that obtained with a far-field or PFA, see Figure 4.8 (c). Again, the
better focusing capabilities of the presented algorithm are clearly visible. As expected,
aberrations in outer part of the image obtained with the far-field processor are more
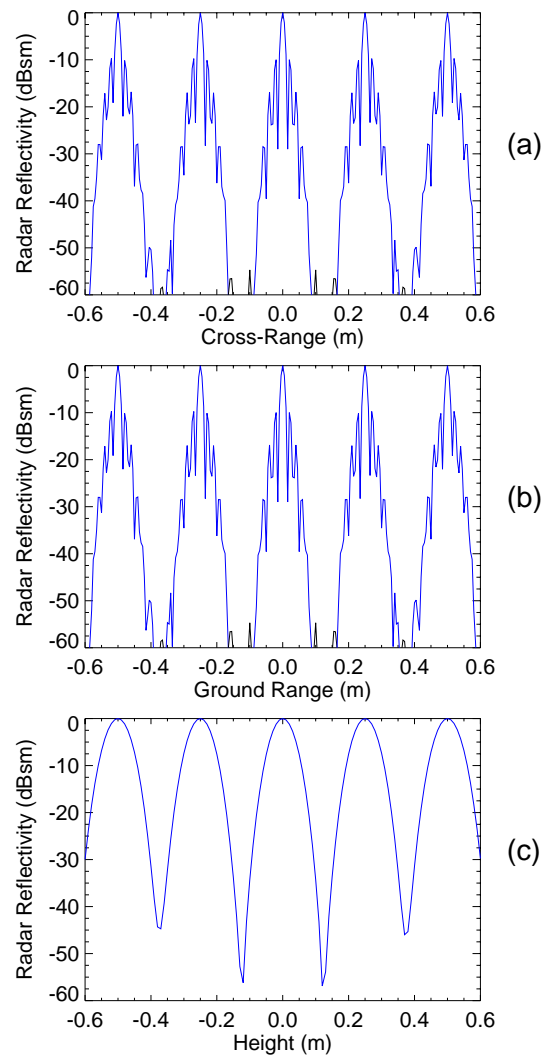
Figure 4.7. Cross-range (a), ground-range (b) and height (c) profiles from the 3-D reflectivity image obtained in the numerical simulation.

evident.

The target used in the second test measurement was a 3-D arrangement of eight metallic spheres of diameter 7.62 cm, see Figure 4.9 and photograph in Figure 4.10 (a). The measurement was conducted with the same angular span in azimuth and elevation, with 61 points equally spaced within the angular range from 0 to 45 deg, acquiring the backscattered fields in the HH polarization at 801 frequency points spaced 5 MHz within the frequency range 8 to 12 GHz. Here, the number of frequency points was decimated by a factor of 20 after the calibration. The range to the center of the coordinates system was that of the previous measurement, R_a= 9.56 m. The measurement time required in this experiment was approximately 50 h. Note that there were 3600 antenna positions on the
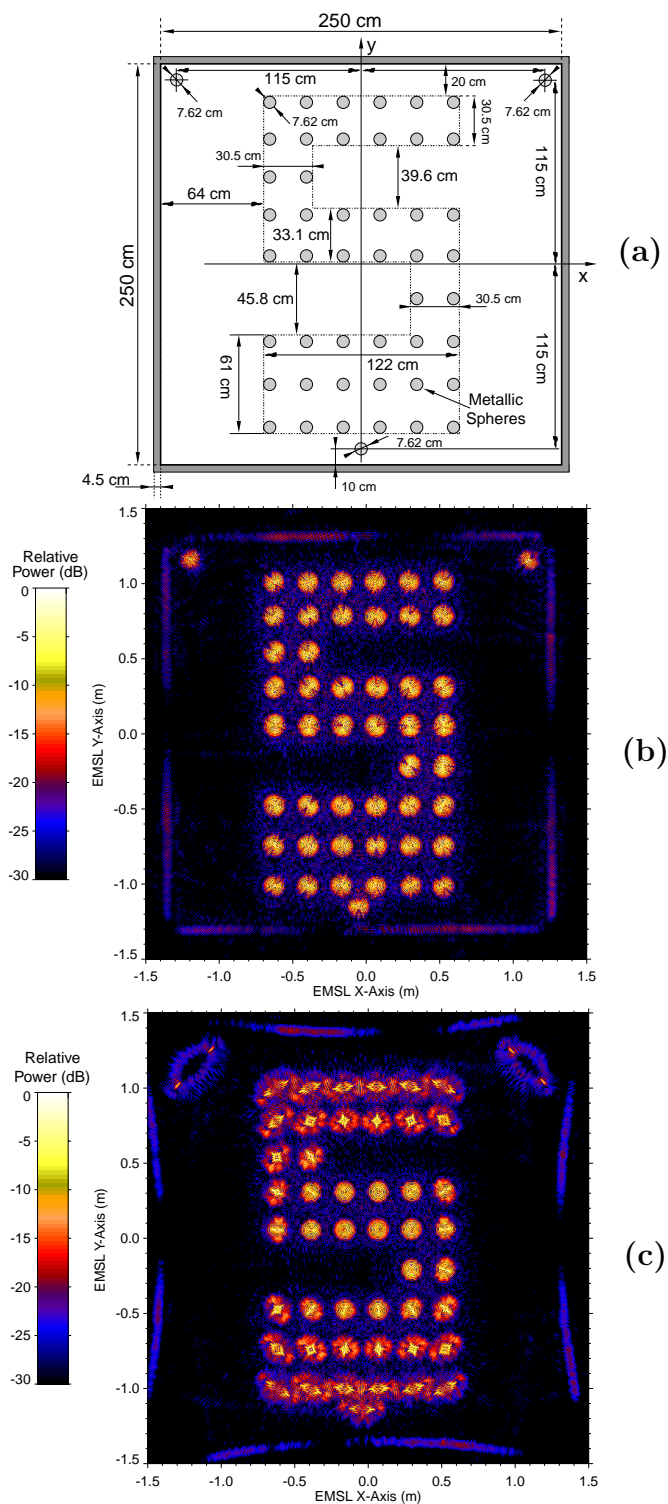
Figure 4.8. (a) Schematic of the planar array of metallic spheres; 2-D SAR images obtained with the near-field (b) and far-field (c) algorithms.
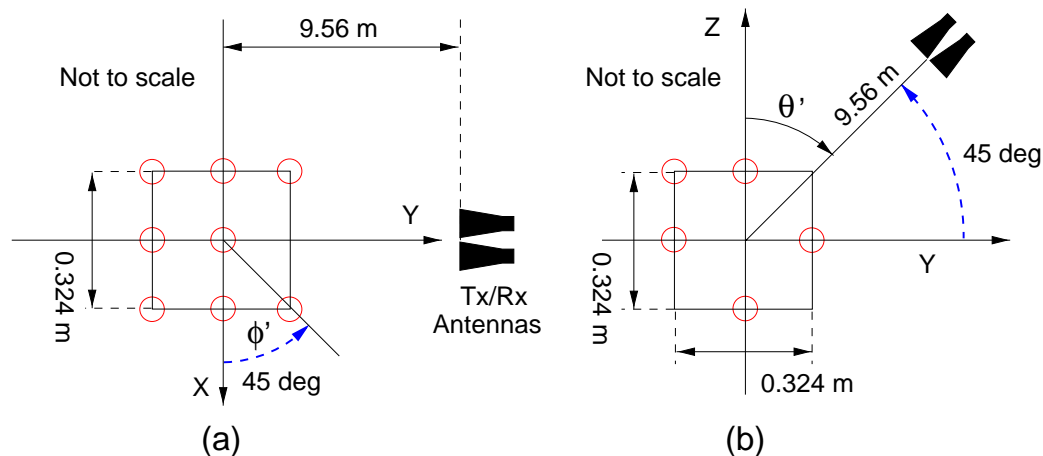
Figure 4.9. Measurement set-up used in the second experiment with a 3-D array of 8 metallic spheres: (a) top view and (b) side view.

(a)   **(b)**
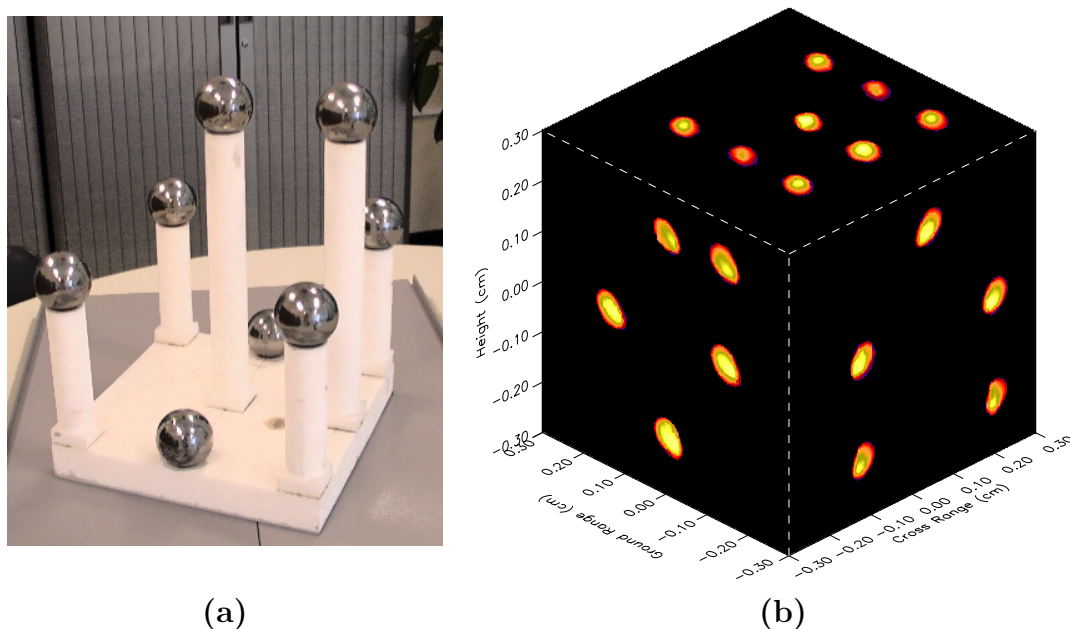
Figure 4.10. Photograph (a) and projections onto the $x-y$, $x-z$ and $y-z$ planes of the 3-D SAR image (b) with the 8 metallic spheres measured in the EMSL.

2-D synthetic aperture. A 3-D SAR image consisting of $N_z = 61$ horizontal slices on a polar raster with $N_\rho = 101$ and $N_\phi = 480$ was reconstructed, as shown in Figure 4.10 (b). The processing time was 3 h 27 min. The achieved resolutions, as expected, were about 2 cm in the cross-range and height directions, and 4 cm in the ground-range direction.

4.3   Polar format algorithm and image rectification

4.3.1   Introduction

Near-field SAR imaging of large objects using the polar format algorithm result in images showing a geometric distortion [3]. The resulting geometric distortion due to the short observation distance can be corrected by applying a rectification algorithm provided that the angular spans of the synthetic aperture are limited.

Mensa developed the first rectification algorithm for 2-D SAR images [49, Appendix A]. This rectification procedure works as follows. First, a 2-D SAR image is formed by using a standard PFA (i.e., interpolation of the polar formatted data onto a Cartesian grid followed by a 2-D FFT). For short observation distances the resulting image will show a geometric distortion. The image is referred to the coordinates system perceived by the radar (i.e., a set of radial lines and concentric circular arcs disposed about the radar antenna). The corrected image, free of any geometric distortion, is obtained by applying a geometric transformation between the coordinates system perceived by the radar and that of the target. This 2-D rectification algorithm can easily be adapted and used to rectify 3-D SAR images. This Section presents a 3-D SAR image formation technique based on the use of a 3-D PFA followed by an image rectification. This technique has been tested with numerical simulations and with anechoic chamber data acquired in the EMSL [60].

4.3.2   Polar format algorithm

Let us consider the measurement geometry shown in Figure 4.1. As considered previously in Section 4.2.1, the backscattered fields $E_s(f, \phi, \theta)$ are acquired as a function of three parameters: the frequency f of the CW signal, the azimuth position of the rotating platform ϕ and the looking angle of the antenna system θ. As indicated in Chapter 2, under the far-field approximation the 3-D reflectivity image of the target can be formed by coherently integrating the backscattered fields within the solid angle of target aspects synthesized in the measurement, i.e. [3, 15]

$$I(\mathbf{r}) = \frac{1}{(2\pi)^3} \int_f \int_\theta \int_\phi E_s(f, \phi, \theta) \exp\left[j(\mathbf{k} \cdot \mathbf{r} - k\, R_a)\right]\, d\mathbf{K} \qquad (4.24)$$

wherein

$$\mathbf{r} = \frac{4\pi f}{c} \left[x\,\hat{\mathbf{x}} + y\,\hat{\mathbf{y}} + z\,\hat{\mathbf{z}} \right] \tag{4.25}$$

$$\mathbf{k} = \frac{4\pi f}{c} \left[\cos\phi \sin\theta\,\hat{\mathbf{x}} + \sin\phi \sin\theta\,\hat{\mathbf{y}} + \cos\theta\,\hat{\mathbf{z}} \right] \tag{4.26}$$

$$d\mathbf{K} = \left(\frac{4\pi}{c} \right)^3 f^2 \, \sin\theta \, d\phi \, d\theta \, df \tag{4.27}$$

One can easily note that the volume integral in (4.24) becomes a Fourier integral after re-sampling the backscatter data onto a Cartesian grid in the frequency wavenumber space. After this re-sampling or interpolation the integral simply reduces to following 3-D Fourier transform

$$I(\mathbf{r}) = \frac{8}{c^3} \int_{f_x} \int_{f_y} \int_{f_y} \tilde{E}_s(f_x, f_y, f_z) \exp\left[j\,2\pi(f_x\,x + f_y\,y + f_z\,z - \frac{2f}{c}\,R_a) \right] \, df_x \, df_y \, df_z \tag{4.28}$$

where

$$\tilde{E}_s(f_x, f_y, f_z) = E_s(f, \phi, \theta) \, f^2 \sin\theta \tag{4.29}$$

with

$$f_x = \frac{2f}{c} \cos\phi \, \sin\theta \tag{4.30}$$

$$f_y = \frac{2f}{c} \sin\phi \, \sin\theta \tag{4.31}$$

$$f_z = \frac{2f}{c} \cos\theta \tag{4.32}$$

The type of re-sampling or interpolation required in (4.29) is well known in the field of computer tomography [96, 97, 98]. The factor $f^2 \sin\theta$ in (4.29) is a weighting function applied prior to the Fourier transform which does not play an important role. In practice, the interpolated frequency domain data will be weighted with a window function in order to reduce the side-lobes in the reflectivity image [87].

4.3.3 Rectification algorithm

Consider the measurement geometry shown in Figure 4.11, where a target rotates about the z-axis forming an angle ϕ with the x-axis (in the inverse SAR mode). The target is illuminated by an antenna that is located in the $y - z$ plane and rotates about the x-axis forming an angle θ_a with the z-axis (in the spotlight mode). When the observation distance is small compared to the target size (i.e., the antenna is in the near-field of the target) the wavefront impinging the target becomes spherical. As a result, the surfaces of
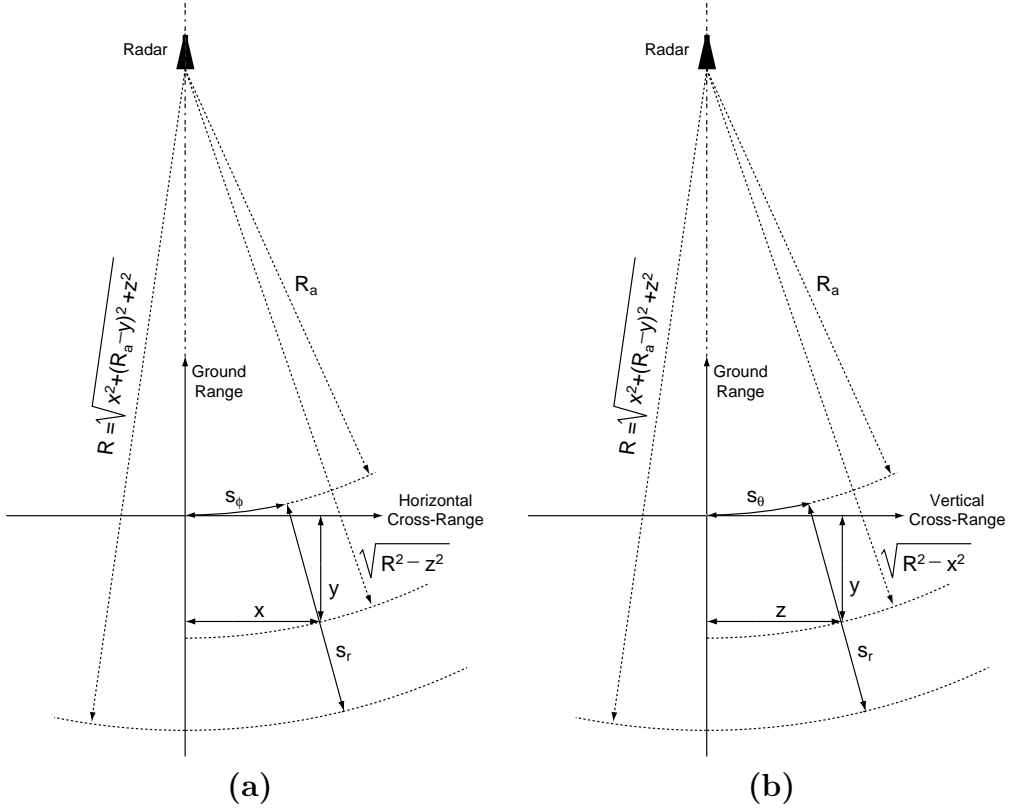
Figure 4.11. Radar and target coordinates system: (a) top view and (b) side view.

constant range, horizontal and vertical cross-range respectively describe a set of mutually orthogonal radial planes and concentric spheres disposed about the radar antenna [49]. With such a measurement geometry, the range to the point scatterer located at P is

$$R(\phi, \theta_a) = \sqrt{(\rho \cos \phi)^2 + (\rho \sin \phi + R_a \sin \theta_a)^2 + (z - R_a \cos \theta_a)^2} \qquad (4.33)$$

By properly processing the acquired backscatter, the radar can measure the range R and two Doppler quantities that are proportional to the derivative of R with respect to the angles ϕ and θ_a, respectively. Thus, the set of coordinates perceived by the radar is given by

$$
\begin{aligned}
S_\phi &= \frac{\partial R}{\partial \phi} = \frac{R_a}{R} \, x \sin \theta_a \\
S_r &= R - R_a \\
S_\theta &= \frac{\partial R}{\partial \theta_a} = \frac{R_a}{R} \, (y \cos \theta_a + z \sin \theta_a)
\end{aligned}
\qquad (4.34)
$$

which correspond to the following set of target coordinates (Cartesian coordinates system),

$$
\begin{aligned}
S_x &= S_\phi \\
S_y &= S_r \sin\theta_a + S_\theta \cos\theta_a \\
S_z &= -S_r \cos\theta_a + S_\theta \sin\theta_a
\end{aligned}
\tag{4.35}
$$

The above identities can be further simplified if a rotation about the x-axis of an angle θ_a is applied. The corresponding rotation matrix is as follows:

$$
\begin{pmatrix} \tilde{x} \\ \tilde{y} \\ \tilde{z} \end{pmatrix} =
\begin{pmatrix}
1 & 0 & 0 \\
0 & \sin\theta_a & -\cos\theta_a \\
0 & \cos\theta_a & \sin\theta_a
\end{pmatrix}
\begin{pmatrix} x \\ y \\ z \end{pmatrix}
\tag{4.36}
$$

Equation (4.34) in the rotated coordinates system can be rewritten in the following form:

$$
\begin{aligned}
S_\phi &= \frac{R_a}{R}\,\tilde{x}\sin\theta_a \\
S_r &= R - R_a \\
S_\theta &= \frac{R_a}{R}\,\tilde{z}
\end{aligned}
\tag{4.37}
$$

with

$$
R = \sqrt{\tilde{x}^2 + (\tilde{y} + R_a)^2 + \tilde{z}^2}
\tag{4.38}
$$

The inverse transformation from perceived radar coordinates to the corrected ones is given by

$$
\begin{pmatrix} x \\ y \\ z \end{pmatrix} =
\begin{pmatrix}
1 & 0 & 0 \\
0 & \sin\theta_a & \cos\theta_a \\
0 & -\cos\theta_a & \sin\theta_a
\end{pmatrix}
\begin{pmatrix}
\dfrac{S_\phi R}{R_a \sin\theta_a} \\[2ex]
\sqrt{R^2 - \left(\dfrac{S_\phi R}{R_a \sin\theta_a}\right)^2 - \left(\dfrac{S_\theta R}{R_a}\right)^2} - R_a \\[2ex]
\dfrac{S_\theta R}{R_a}
\end{pmatrix}
\tag{4.39}
$$

wherein $R = S_r + R_a$. Note that if $\theta_a = \pi/2$, Equations (4.34) and (4.39) properly reduce to those in [49, Appendix A]. Moreover, for a large observation distance (i.e., $R_a \gg D$, where D denotes the size of the target), the geometric distortion vanishes and the coordinates perceived by the radar coincide with those of the target.

The processing steps of the resulting imaging algorithm are shown in the flowchart of Figure 4.12.
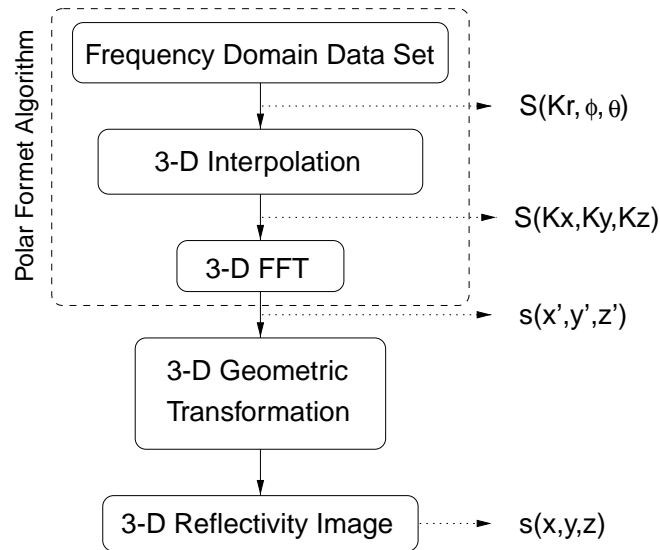
Figure 4.12. Flow-chart of the imaging algorithm.

4.3.4 Experimental results

Numerical simulations

The target used in this numerical simulation consisted of a 3-D ensemble of 56 point scatterers uniformly distributed along the edges of a cube of side 2 m^3, as shown in Figure 4.13. The range to the center of the coordinates system was R_a= 5 m. The RCS of all the scatterers was equal and set to 0 dBsm. This target was imaged in the frequency
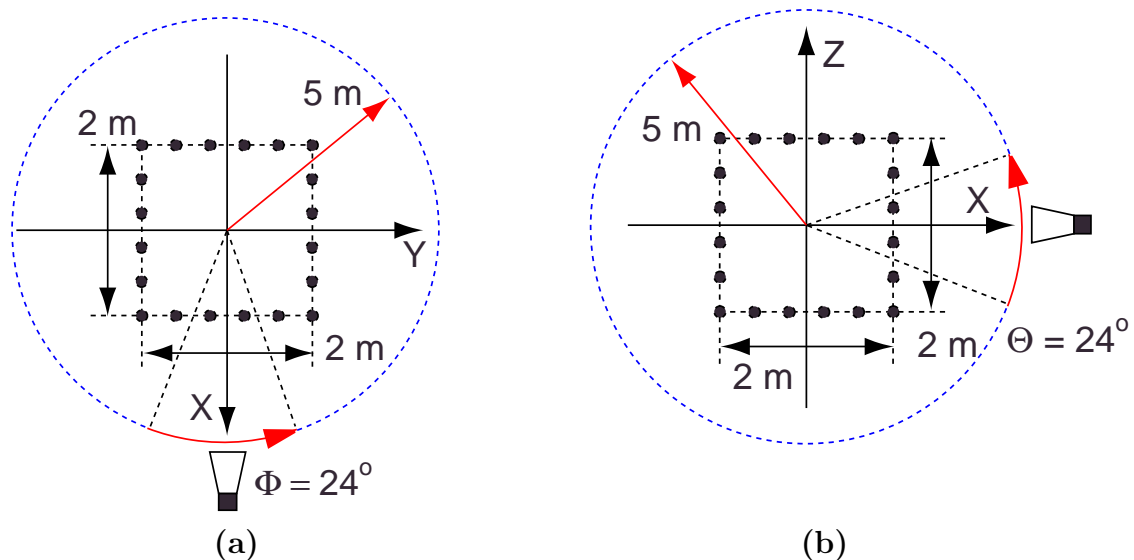
Figure 4.13. Sketch of the measurement set-up used in the simulation with the ensemble of 56 point scatterers: (a) top view; (b) side view.
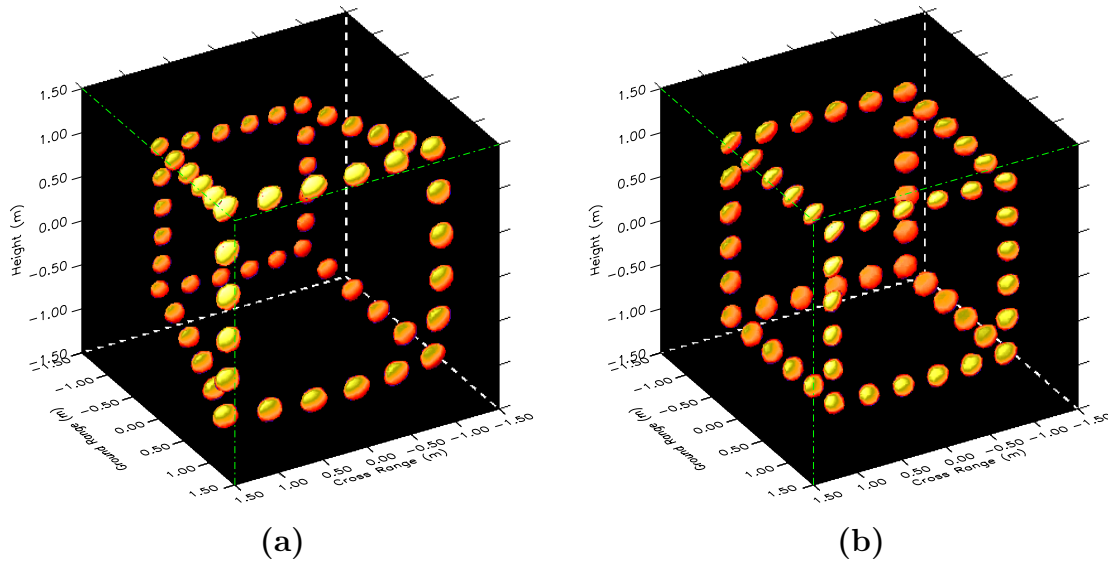
Figure 4.14. Iso-surfaces of the 3-D reflectivity images obtained before (a) and after (b) the geometric rectification.

range from 2 to 6 GHz, sweeping 101 frequency points spaced 40 MHz. The aspect angle in azimuth ϕ ranged from -12 to $+12$ deg, with 49 azimuth points uniformly space 0.48 deg. The aspect angle in elevation θ ranged from 78 to 102 deg, with the same number of points and spacing as those in ϕ. Note that, for this target, the far-field condition is satisfied at a range distance of about 960 m. This indicates that the geometric distortion introduced by the short observation distance will be enormous.

A 3-D SAR image was reconstructed using the presented near-field SAR algorithm. The computation time needed to form the image was less than 4 min on a high-performance Sun workstation. There is probably no other way to synthesize a 3-D near-field SAR image in a shorter time. However, it must be kept in mind that the effectiveness of the geometric rectification degrades notably as the angular spans of the two aspect angles (ϕ, θ) increase. In this example, the angular spans were narrow enough for an effective mitigation of the geometric distortion. Figure 4.14 shows the iso-surfaces of the 3-D reflectivity images before and after the geometric rectification. The positions of the point scatterers after the rectification are in perfect agreement with the actual ones. The geometric distortion in the image has been highly reduced by using the proposed rectification technique.

Measurements

The experiments have been performed with a 3-D SAR measurement of a 5 m high Fir tree. The full description of the experiment is given in the Chapter 5. A Tx antenna

was located at a distance $R_a = 9.56$ m from the focal point of the anechoic chamber. A receiving antenna, which was $1.5°$ apart, acquired the backscattered fields by the entire tree. The backscattered fields from the tree $E_s(f, \phi, \theta)$ were collected as a function of three parameters: the frequency f of the CW synthesizer, the azimuth position of the rotating platform ϕ, and the looking angle of the antenna system θ. The frequency ranged from 1.0 to 5.5 GHz, sampling a total of 401 points. In the measurement, the azimuth angle ϕ covered an span of $24°$, sweeping a total of 41 azimuth aspect angles $0.6°$ apart. The angular span in the antenna looking angle θ was $24°$, covering the range from 28 to $52°$ with 81 points spaced $0.3°$. The far-field condition for the tree is satisfied at a range distance of about 1833 m. Therefore the image obtained with the PFA will be highly distorted due to the short observation distance.

Three frequency ranges were selected: 1.0 to 2.8 GHz (low band), 3.7 to 5.5 GHz (high band), and 1.0 to 5.5 GHz (entire band). A 3-D SAR image in the HH polarization was formed in these three bands using the proposed imaging algorithm with the geometric rectification. The computation time for each image, as in the numerical simulation, was extremely short and below 5 min. Figure 4.15 shows the vertical slices out of the 3-D SAR images corresponding to the front and side views. The slices with finer resolution are obviously those using the entire frequency band. As expected, those with the coarser resolution correspond to the low band. The dynamic range of the images shown is 30 dB.
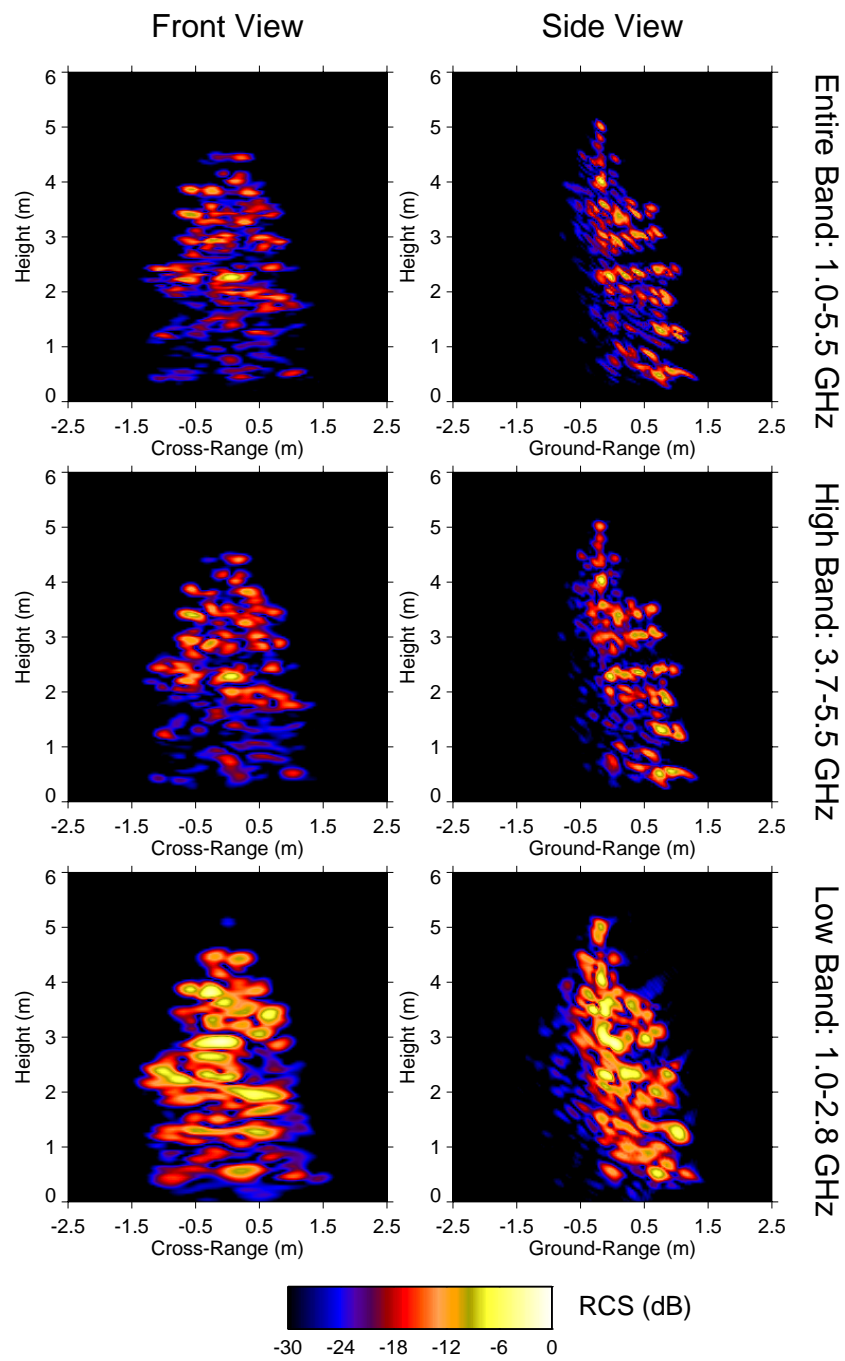
Figure 4.15. Slices of the 3-D SAR image of the Fir tree in the HH polarization in three different frequency bands.

3-D Near-Field Radar Imaging of a Fir Tree

5.1 Introduction

First analyzes of a single Fir tree in the microwave region were performed in 1982 [99] using a high-resolution, pulsed, coherent radar operating in the scatterometric mode at 10 GHz. In this experiment, the scattering centers and their corresponding polarimetric signatures were measured. The main scattering sources were associated to the green, outer branches coated with needles. This work was followed by further investigations on tree signatures showing that both attenuation and backscattering are highly dependent on the tree structure (i.e. size, shape and orientation of trunk, branches and needles) and the selected polarization [100, 101, 102, 103, 104]. This polarization dependence is, in general, significant due to the strong anisotropic character of trees.

Measurements of a forest canopy under natural conditions are complex. One has to define the relevant canopy parameters to be measured and deploy the required instrumentation associated with outdoor radar measurements. Effects such as varying weather conditions, the ground tree interaction, presence of RF interfering signals, shadowing introduced by surrounding trees, unknown variations of the local topography and soil conditions may heavily influence the measurement. As a result, experimental data acquired under these conditions may not be interpreted properly and consequently lead to wrong conclusions. On the other hand, when running the measurements in an anechoic chamber under laboratory conditions, all relevant measurement parameters can be fully controlled. The measurement data can be accurately calibrated. The backscatter from the tree volume can be isolated by covering with microwave absorber the underlying surfaces, facilitating the interpretation of the acquired data.

To date most of the radar measurements on single trees performed under laboratory conditions have been carried out using non-imaging systems that measure the backscatter from parts of the tree, without dealing with the backscattering from the entire tree. A typical set-up used in these measurements is reported in [105]. In the frequency range of interest for forestry applications (i.e. P, L and C bands), a non-imaging or scatterometric system has a cross-range resolution limited by the radar's beamwidth, which means that the position of the scattering centers within the tree volume cannot be determined precisely. Nowadays, indoor SAR systems are available and, with the development of highly efficient imaging algorithms, it is possible to image an entire tree with much finer cross-range resolutions (in the horizontal and vertical directions). The major scatterers and their position within the tree volume can be identified by means of this new technique [32, 36, 67]. This can be used as a new tool to gain a better understanding of the interactions between the tree and the microwave. In addition to the position and intensity of the main scattering centers, an indication about the dominant scattering mechanism can be given by using a recently developed polarimetric classification scheme [106].

This Chapter reports on a tree imaging experiment conducted in the anechoic chamber of the EMSL [60]. The main objective of this experiment was to map the radar reflectivity of an entire Fir tree in order to support the understanding of the interaction of electromagnetic waves with natural targets and provide the base for the validation and verification of existing models.

This Chapter is organized as follows. First, in Section 5.2, a general description of the experiment, the measurement technique and main characteristics are presented. The 2-D and 3-D near-field SAR imaging algorithms used to focus the acquired backscatter data are described in Section 5.3. The resulting radar images of the tree are presented and discussed in Section 5.4.

5.2   Measurement set-up

The present experiment consisted of a three 3-D imaging measurement on a 5 m high Balsam Fir tree (*Abies Nordmanniana*), which was approximately 21 years old. The radar measurements were performed in a controlled environment, making use of the anechoic chamber of the EMSL. In order to have stable measurement conditions, prior to and during the measurements the tree was watered regularly. A constant artificial illumination replicating the sunlight's spectrum was used to reduce the day-night effect. The tree used in this experiment presented quasi-horizontal branches bearing typically 2-3 cm needles showing a brush-like distribution. The branches constituted large horizontal planar sur-

faces at different levels in height. The top of this tree conforms to a young tree of its same species. The tree was put in a pot and then mounted on a rotating platform inside the anechoic chamber, as shown in the photographs in Figure 5.1. The pot under the tree was covered with microwave absorber, to make sure that the measured backscatter did not include any contribution from the ground and the corresponding interaction with the tree. The measurement system is based on a network analyzer and operates in the stepped-frequency mode. The frequency band used in the measurement ranged from 1 to 5.5 GHz, i.e. covering the L, S and C bands, using a frequency step of 5.625 MHz and sweeping a total of 401 frequency points. The acquired data in the frequency domain were empty room subtracted and gated in the time domain in order to isolate the response of the tree from the residual antennas coupling and eventual spurious reflections in the chamber. Then a single reference, fully polarimetric calibration [70], using a reference target placed at the focal point of the chamber, was applied. The calibration accuracy has proven to be better than 0.5 dB in power and $5°$ in phase at 0 dBsm. The sensitivity depends on the number of averaged samples at each frequency point and the time gate span; e.g., with an averaging factor of 128, equivalent to an integration time of 0.025 s and a time gate span of 10 ns, a system noise floor of –55 dBsm at 2 GHz was measured [107]. The antenna system is polarimetric and consists of two dual polarized horn antennas that, in the measured frequency range, has a 3 dB beamwidth of about $30°$, which is sufficient to irradiate the entire tree. The measured cross-pol isolation is better than 30 dB in the region occupied by the tree.

(a)   (b)
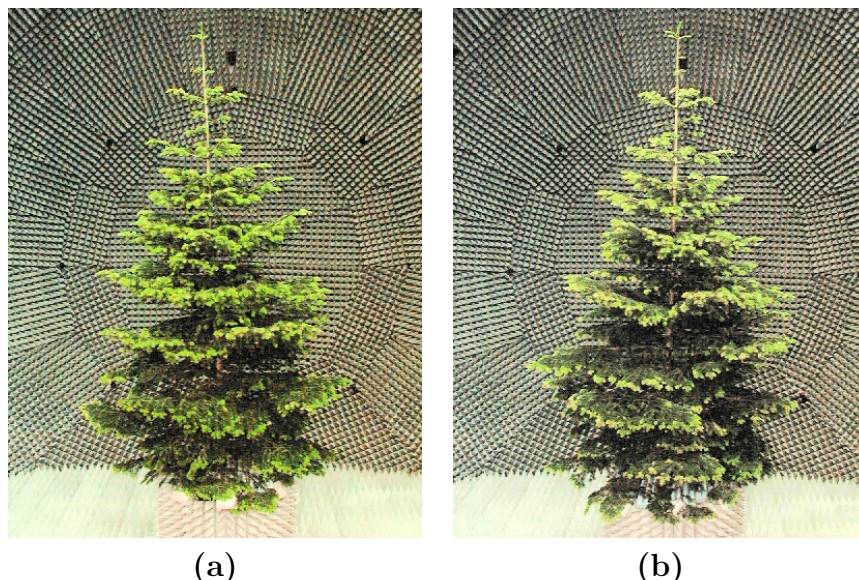
Figure 5.1. Photographs of the 5 m high Balsam Fir tree inside the anechoic chamber of the EMSL: (a) side and (b) front views.
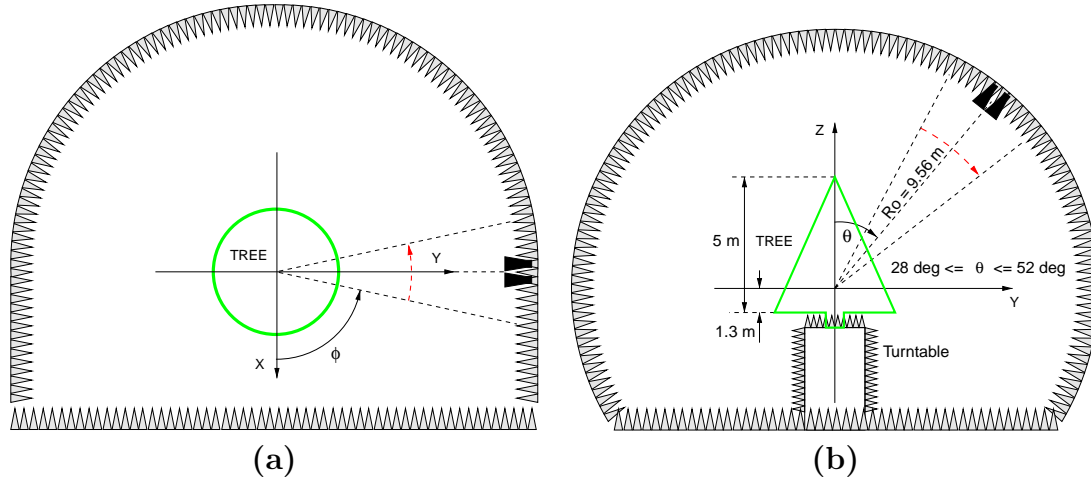
Figure 5.2. Imaging geometry used in the measurement of the Fir tree: (a) top view and (b) side view.

In addition to the imaging measurements, and within the frame of a scientific collaboration between the George Washington University, the Canadian CCRS and the JRC, a series of scatterometric measurements were carried out [108]. These measurements were divided into three groups: monostatic, bistatic and measurements in the forward direction. The bistatic measurements were made to test the strength of the specular trunk scatter which is an important factor in double bounce contribution appearing in many forest models. In addition, some bistatic measurements in the forward direction were also performed. After finishing the measurements, a tree vectorization was performed by Robert Landry, from CCRS. This technique is used to setup a database with the position, average orientation and dimensions of all branches and the trunk. These data can afterwards be used to generate a realistic computer tree model, which is being developed at present. During the tree vectorization, a series of dielectric permittivity measurements on the tree bark, sap wood and hard wood portion of the trunk, needles and branches was undertaken using a coaxial probe. These measurements were performed over a much wider frequency range compared to that one used in the imaging mode. An HP-8510B VNA based reflection coefficient measurement with an open-ended coaxial probe was used.

5.3   Reconstruction algorithm

The imaging geometry is shown in Figure 5.2. A CW signal is radiated from an antenna, located at a distance $R_a = 9.56$ m from the focal point of the anechoic chamber. A receiving antenna, which is 1.5° apart, acquires the backscattered fields by the entire tree. The tree is mounted on a low reflectivity platform covered with absorber. This platform

rotates about the z-axis forming an angle ϕ with the x-axis. The antennas rotate in the $y - z$ plane forming an angle θ with the z-axis. Thus, the tree backscatter $E_s(f, \phi, \theta)$ can be acquired as a function of three parameters: the frequency f of the CW synthesizer, the azimuth position of the rotating platform ϕ, and the looking angle of the antenna system θ. In the measurement, the azimuth angle ϕ covered an span of 24°, sweeping a total of 41 azimuth aspect angles 0.6° apart. The angular span in the antenna looking angle θ was 24°, covering the range from 28 to 52° with 81 points spaced 0.3°. These angular steps in the azimuth and elevation directions have been fixed according to the following upper bounds,

$$\Delta\phi \ \leq \ \frac{\lambda_{\min}}{2 \, D_h \sin\theta} \tag{5.1}$$

$$\Delta\theta \ \leq \ \frac{\lambda_{\min}}{2 \, D_v \sin\theta} \tag{5.2}$$

where $\lambda_{\min}$ is the minimum radar wavelength (at the highest frequency). D_h and D_v denote the tree width and height, respectively. As expected, the required angular sampling rates increase with increasing electrical dimensions of the tree.

The measurement parameters used in the imaging experiment are summarized in Table 5.1. Note that with such measurement parameters, apart from a 3-D SAR image, one can form a number of 2-D SAR images or projections of the 3-D SAR image onto the horizontal and the vertical planes. What follows is a description of the imaging algorithms especially developed to form the 2-D and 3-D SAR images of the measured Fir tree. The influence of the antenna pattern is considered to be negligible and is not taken into account when forming the images. All radar images are calibrated and display the spatial distribution of RCS in dBsm. In principle, by properly measuring the effective area illuminated by the radar, the reflectivity values can be converted to the backscattering coefficients σ°. However, in the present measurement there are high spillover losses due to the large 3 dB beamwidth of the horn antennas (approximately 30°) and therefore this conversion has not been applied.

It is important to note that the reconstruction algorithms presented here are linear and

Table 5.1. Measurement parameters used in the tree imaging experiment.

Polarizations:	HH–HV–VH–VV			
Parameter:	Min	Max	Step	# Points
Tree azimuth rotation (°):	–12.0	12.0	0.6	41
Antenna looking angle (°):	28.0	52.0	0.3	81
Frequency (GHz):	1.0	5.5	0.01125	401

model the target as a set of non-dispersive scatterers arbitrarily distributed. The multiple interactions between the scattering centers will only be focused if they are present at the same range bin for all the antenna positions in the synthetic aperture. A typical example is the interaction between a tree trunk and the ground surface. If this is not the case, the artifacts associated to the multiple interactions will be blurred by the reconstruction algorithm. Consequently, the peak amplitude of the artifacts may be significantly reduced and sometimes they are not even observable. When imaging a target with a high degree of anisotropy such as a tree, one would expect that the multiple interaction term will show significant differences depending on the observed polarization. The problem of exploiting the use of a polarimetric classification scheme which provides a spatial distribution of the dominant scattering mechanisms (e.g. surface, dipole and dihedral) within the tree volume has been recently addressed [109]. This technique has been used to separate real scatterers from artifacts due to the multiple interactions.

5.3.1   Two-dimensional SAR imaging

The projections of the tree volume onto two orthogonal planes, in our case the horizontal and vertical planes, can be formed by using a 2-D SAR processor that takes into account the near-field condition. The 2-D SAR image in the horizontal plane is obtained by taking a single antenna aspect angle in the elevation plane θ_a, and synthesizing an horizontal aperture in the azimuth direction. The resulting 2-D radar reflectivity map at $z = 0$ is given by [11],

$$I(x, y, z = 0) = \frac{4}{c^2} \sin \theta_a \int_f f df \int_{\phi'} E_s(f, \phi', \theta = \theta_a) \, (\frac{R_{xy}}{R_a})^2 \, \exp\left[j2k(R_{xy} - R_a)\right] d\phi' \tag{5.3}$$

where k denotes the frequency wavenumber and R_{xy} is the range to the point with coordinates $(x, y, z = 0)$,

$$R_{xy} = \sqrt{R_a^2 + x^2 + y^2 - 2R_a \, x \sin \theta_a} \tag{5.4}$$

As shown for example in [49], the resolutions in the horizontal cross-range x and in ground-range y can be approximated as

$$\delta_x \quad \simeq \quad \frac{c}{4 \, f_{\max} \, \sin\left(\dfrac{W_\phi}{2}\right) \sin \theta_a} \tag{5.5}$$

$$\delta_y \quad \simeq \quad \frac{c}{2 \, W_f \sin \theta_a} \tag{5.6}$$

where W_ϕ and W_f denote the azimuth and frequency spans, respectively. Fine resolution in cross-range implies coherent processing through a large W_ϕ. High resolution in ground-

range is achieved by increasing the amount of synthesized bandwidth W_f. Note that for steep incidence angles both resolutions degrade considerably.

Alternatively, a 2-D SAR image in the vertical plane can be formed by choosing an azimuth aspect angle ϕ' and synthesizing a vertical aperture. In this case, the 2-D SAR reflectivity map at $x = 0$ is computed as

$$I(x = 0, y, z) = \frac{4}{c^2} \int_f f df \int_\theta E_s(f, \phi = \phi', \theta) \, (\frac{R_{yz}}{R_a})^2 \, \exp\left[j2k(R_{yz} - R_a)\right] d\theta \qquad (5.7)$$

where

$$R_{yz} = \sqrt{R_a^2 + y^2 + z^2 - 2R_a \left[y \sin\theta + z \cos\theta\right]} \qquad (5.8)$$

The resulting resolutions in the ground-range and vertical cross-range directions are

$$\delta_y \simeq \frac{c}{2 \left(f_{\max} \sin\theta_{\max} - f_{\min} \sin\theta_{\min}\right)} \qquad (5.9)$$

$$\delta_z \simeq \frac{c}{2 \left(f_{\max} \cos\theta_{\min} - f_{\min} \cos\theta_{\max}\right)} \qquad (5.10)$$

wherein $\theta_{\min}$ and $\theta_{\max}$ denote the minimum (steepest) and maximum antenna looking angles, respectively; $f_{\min}$ is the minimum CW frequency measured. Note that in (5.3) and (5.7), both the exact near-field phase history and the free-space propagation losses are accounted for by the exponential function and the quadratic term in the amplitude, respectively. The formation of the two 2-D SAR images in the vertical and horizontal planes provides a first indication of the position and intensity of the main scattering centers within the tree volume.

5.3.2 Three-dimensional SAR imaging

Similarly to (5.3) and (5.7), the 3-D complex reflectivity image in cylindrical coordinates $I(\rho, \phi, z)$ can be written as follows [11, 41],

$$I(\rho, \phi, z) = \frac{8}{c^3} \int_f f^2 df \int_\theta \sin\theta d\theta \int_{\phi'} E_s(f, \phi', \theta) \, F(\rho, \phi - \phi', z; f, \theta) \, d\phi' \qquad (5.11)$$

where $F(\cdot)$ is a near-field focusing function (or space-variant matched filter) which can be expressed as,

$$F(\rho, \phi, z; f, \theta) = (\frac{R}{R_a})^2 \, \exp\left[j2k(R - R_a)\right] \qquad (5.12)$$

$$R = \sqrt{R_a^2 + \rho^2 + z^2 - 2R_a \left[\rho \sin\theta \, \cos\phi + z \cos\theta\right]} \qquad (5.13)$$

Here R denotes the range to the point with coordinates (ρ, ϕ, z). R_a is the range to the center of the coordinates system and zero-phase reference point. In (5.11), the wavefront illuminating the tree is spherical due to the short observation distance.

The formation of a 3-D SAR radar image under the near-field condition is computationally very intensive [49]. As an example, with the focusing algorithm as equated in (5.11), a 3-D SAR radar image of the Fir tree with dimensions $5 \times 5 \times 6$ m^3 and $101 \times 101 \times 61$ voxels requires the computation of approximately 1.25 E+08 azimuth FFTs of 1024-points, which is about 0.5 Tera-Flop. Moreover, during the image formation, a 3-D float complex array of about 80 MByte must be stored on the RAM. Using a high performance workstation (a Sun Ultra-Sparc equipped with one CPU of 64 bits and a DRAM of 128 MByte), the data focusing takes 4 days. Therefore, there is a clear need to speeding up the code. As indicated in Section 4.2, a possible alternative is to use the MSP to calculate analytically the discrete Fourier transform of the near-field focusing function in (5.11) [58]. This new algorithm is about four times faster than that using the azimuth FFTs.

5.4   Experimental results and discussion

This Section is divided into three parts. First, an analysis of the frequency domain data acquired in the Fir tree imaging measurement is presented. Then, the obtained 2-D SAR images of the Fir tree (projected onto the horizontal and vertical planes) are introduced with a discussion on the interpretation of the results. Finally, an assessment on the 3-D SAR image of the Fir tree is addressed.

5.4.1   Frequency domain data analysis

The acquired data in the imaging measurement have been analyzed. The measured mean RCS as a function of the frequency and the antenna looking angle are shown in Figures 5.3 (a) and 5.3 (b), respectively. In the frequency plot, after averaging over the measured angular ranges in azimuth and elevation, the backscatter in HH is higher than that in VV and HV over the entire frequency range. However, as the frequency increases, the three backscattering coefficients tend to converge to a common value. At high frequencies, it is expected that the electromagnetic interaction between branches and the absorption losses will become more important and therefore the tree behaves more as a cluster of lossy dipoles randomly oriented. Consequently, the cross-pol backscatter increases steadily over the entire frequency range. On the other hand, the backscatter in HH and VV increases in the frequency range from 1 to 3 GHz, and then decrease steadily

following a "bell-shaped" curve. The differences between HH and VV range from about
4 dB at the lowest frequency, to 1 dB at the highest frequency. By applying a Fourier
transform to the frequency backscatter data, the time domain backscatter shows that there
is no prevalence of the response of the trunk, which is probably due to the fact that the
incidence is oblique and the penetration depth through the tree volume is rather limited.
The angular variation of the backscatter, which has been averaged over the entire fre-
quency and azimuth ranges, shows a gradual general decrease in the three backscattering
coefficients. This trend is more evident in the backscatter in VV and HV, with a common
decrease of about 2 dB over the whole angular range. The differences between HH and
VV increase very slowly with a increasing incidence angle. These results are in agreement
with those indicated in [110].

5.4.2   Two-dimensional SAR images

The presented reconstruction algorithms are scalar and as such have to be sequentially
applied to the frequency domain data in each one of the four polarizations. As a result, a
set of four complex reflectivity images is obtained. The phase in the resulting four images
is preserved. In practice, VH is supposed to be identical to HV due to reciprocity. The 2-D
SAR images, in the HH polarization, formed by synthesizing a one-dimensional aperture
in the horizontal ($\theta = 40^o$) and the vertical ($\phi = 0^o$) directions are shown in Figures 5.4 (a)
and 5.4 (b), respectively. When forming these images, a Kaiser-Bessel ($a = 2$) [87] window
has been used both in frequency and azimuth. The measured resolutions in the horizontal
image are approximately 20 cm and 10 cm in the horizontal cross-range and ground range
directions, respectively. The top part of the trunk is distinguishable in the near range (top
part) of the image. The region with the higher reflectivity seems to correspond to one of

(a)   **(b)**
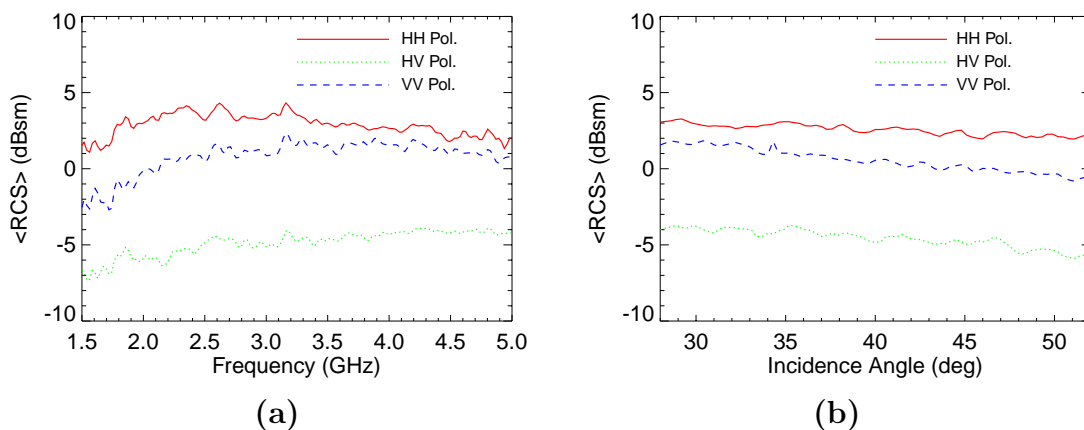
Figure 5.3. Measured mean σ° as a function of the (a) frequency and (b) the antenna looking
angle.
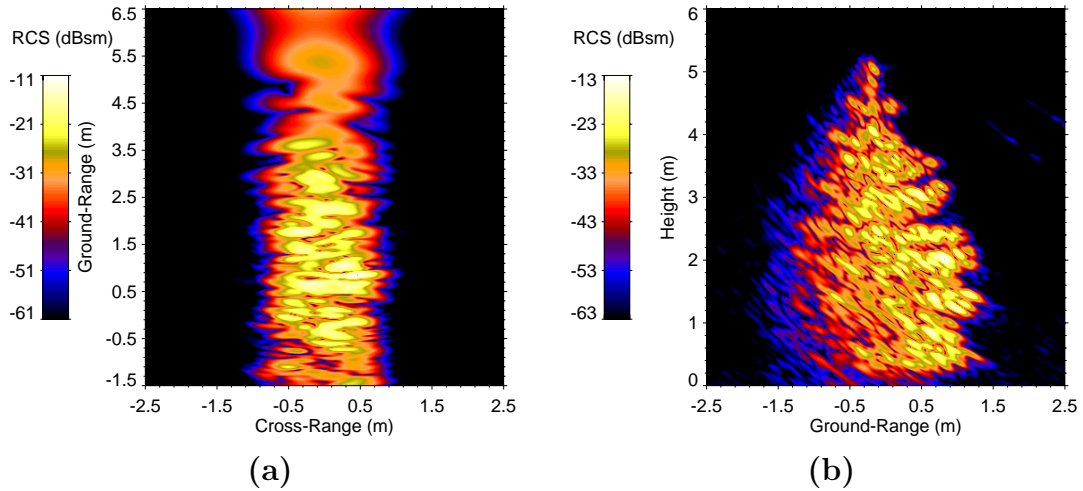
Figure 5.4. 2-D SAR images of the Fir tree projected onto the horizontal (a) and vertical (b) planes in the HH polarization.

the large horizontal branches in the bottom part of the tree, where the reflectivity reaches the maximum value of –11.0 dBsm.

The vertical image presents a higher spatial resolution: about 6 cm in both the vertical cross-range and the ground-range directions. The overall shape is surprisingly close to that of the optical image. Note that the backscattering behavior of the tree at radar frequencies is by far more complicated and radically different from that of optics. In this image, the trunk is slightly tilted towards the far range. This image shows clearly the different large horizontal planar branches in the near-range (illuminated side). Two openings on the near-range side, with heights 3.6 and 3.2 m, are clearly visible in the image. The maximum reflectivity of this image is –13.1 dBsm. The reconstructed reflectivity, as expected, is much lower in the back side due to the attenuation of the transmitted power through the tree canopy.

5.4.3   Three-dimensional SAR images

The 3-D SAR image in VV is shown in Figure 5.5 as seen from the radar. The maximum reflectivity within the tree volume is about –19.5 dBsm. The dynamic range used in this image is 50 dB. As in the vertical 2-D SAR image, the overall shape of radar image coincides with that of the optical image. The spatial resolution, achieved with the frequency bandwidth and the synthetic aperture lengths in elevation and azimuth indicated in Table 5.1, is in the order of 6 cm in the vertical cross-range and ground-range directions, and 15 cm in the horizontal cross-range direction. A Kaiser-Bessel ($a = 2$) window has been applied over the frequency and the two aspect angles (in azimuth and elevation). This

is enough to produce imagery where the position of the scattering centers can be easily associated to a small volume within the tree structure. The vertical slices out of the 3-D images at zero cross-range (side view) and zero ground-range (front view) are shown in Figure 5.6. The observed differences in polarization are more evident in the top part of the tree, where almost there are no branches and the trunk is giving the main contribution to the backscattering. Consequently, the top part of the trunk is more visible in the VV image. On the other hand, in the middle and bottom part of the tree, the tree architecture is more complex and the differences in polarization are smaller. The backscattered power in HV is comparable to those in HH and VV, which indicates that the main scattering centers are mainly associated with the green, outer branches coated with needles.
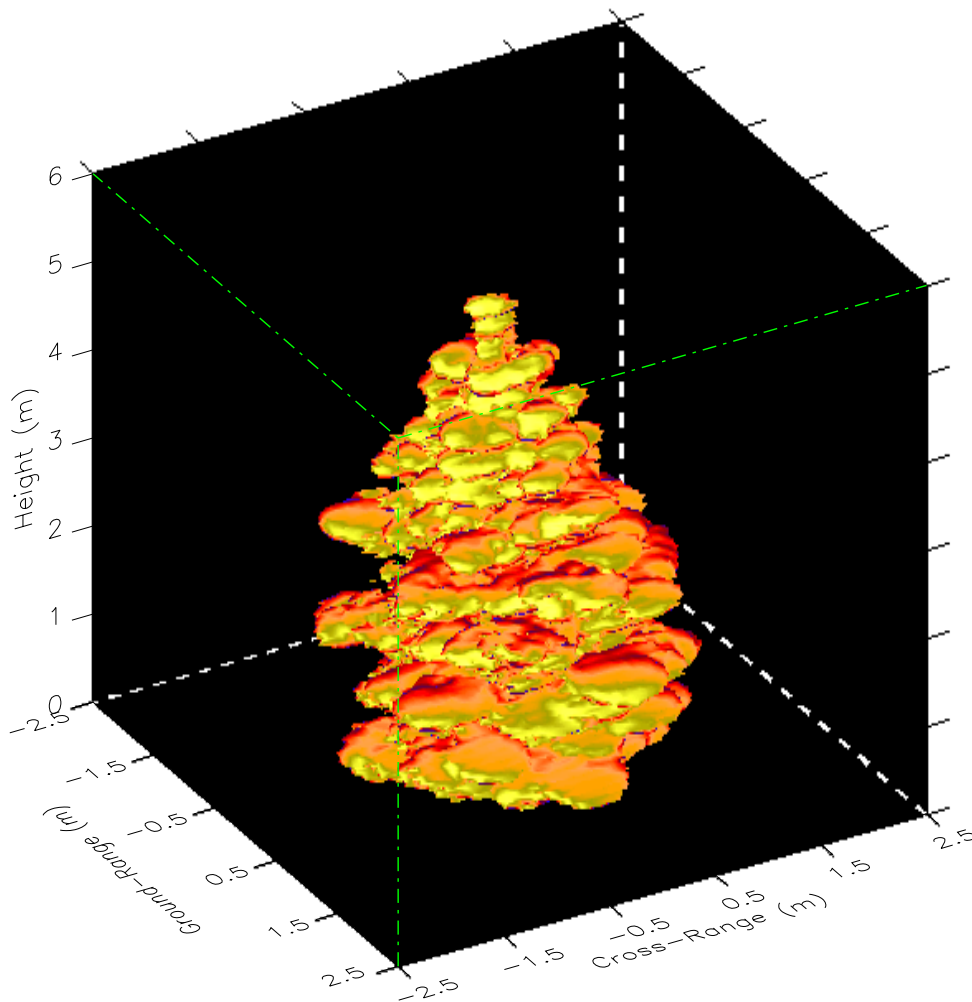
Figure 5.5. 3-D SAR image of the Fir tree in the VV polarization.
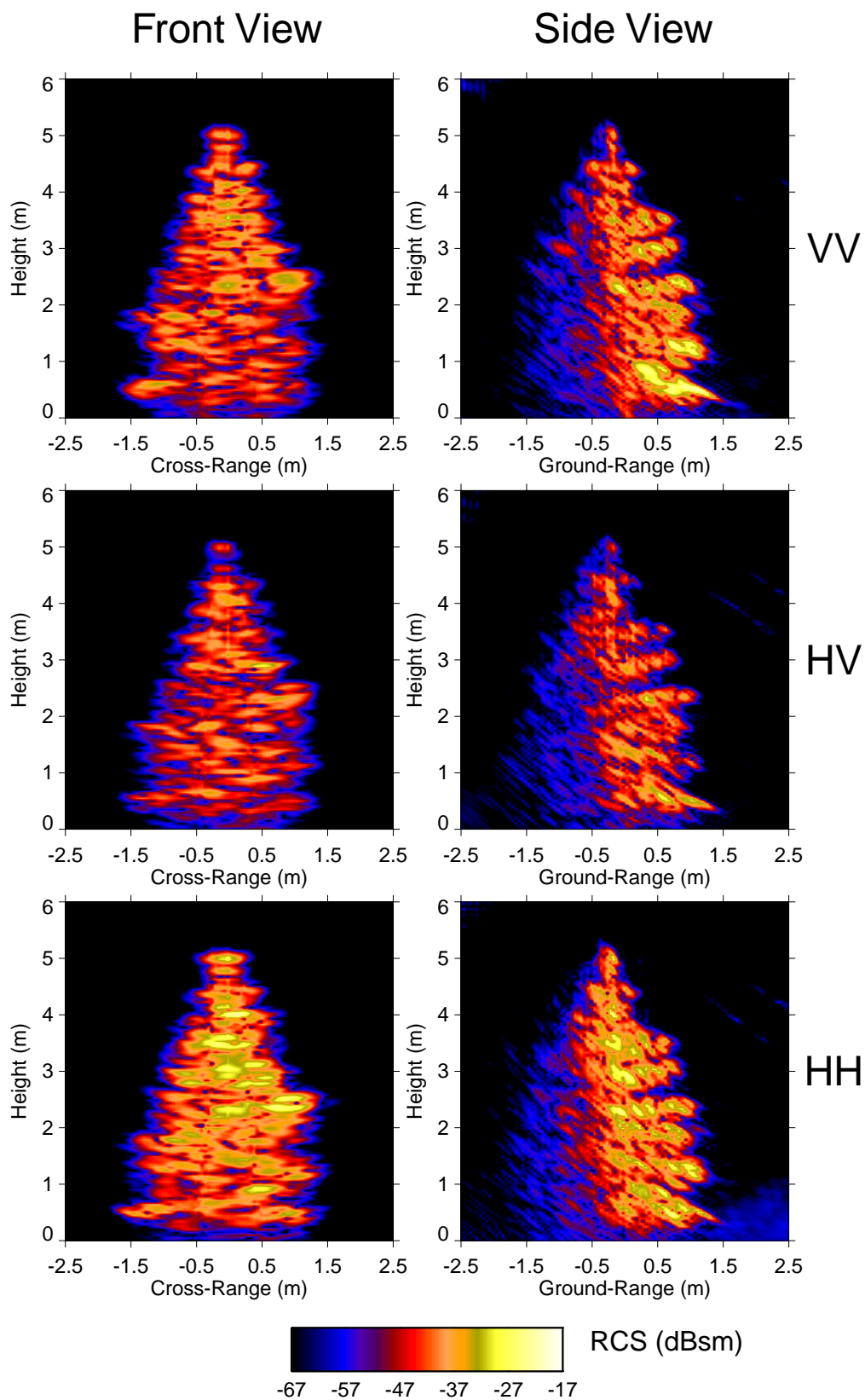
Figure 5.6. Vertical slices out of the 3-D radar image at zero ground-range (front view) and zero cross-range (side view) in the HH, HV and VV polarizations.

3-D Near-Field Subsurface Radar Imaging

6.1 Introduction

This Chapter addresses the problem of the formation of subsurface radar images [111, 112, 113]. This problem is by far more severe than that of forming the radar images in the free-space. The medium where the objects are embedded is usually lossy and inhomogeneous. This together with the presence of the air-ground interface make the task of subsurface radar imaging highly challenging.

A vast majority of the research efforts in this area are purely experimental and mostly focused on the detection and mapping of interfaces in the earth employing commercial versions of ground penetrating radars (GPRs) [114, 115]. In these measurements, the GPR is in towed continuously over the surface collecting backscatter data. Synthetic aperture radar processing (referred to as migration by geophysicists) may be used to process an improved subsurface image. However, difficulties associated with technical limitations of commercial GPRs (e.g., multiple internal reflections, clutter generated by the air-ground interface, poor impedance matching at the antenna,...) and a heterogenous velocity distribution in the subsurface may introduce serious impediments to an efficient use of SAR processing with GPR data. Some of these difficulties are circumvented by separating the antennas from the ground and pointing them in the forward direction. With the antennas looking forward, the measured return from the surface is minimum. However, the return from the buried object is expected to be about the same as that measured with the antennas looking down. Consequently, the forward looking geometry is an alternative to conventional down looking GPR which deserves special attention.

Here, instead of having the radar looking down in close contact with the surface, it is

suggested to have a stand-off forward looking system. This solution is most appropriate when looking for dangerous objects such as anti-personnel landmines (APL) and unexploded ordnance (UXO) [29, 30, 116, 117, 118, 119, 120]. The observation distance for such a system would be in the order of some tens of meters. Candidate platforms where to operate this system are a heavy vehicle or an airship. The use of an air-borne platform is discarded as it is more suitable for the survey of mine fields at a large scale (i.e., not for the detection of every single landmine) [121].

This Chapter presents a novel 3-D near-field subsurface imaging technique. The subsurface image is accurately focused taking into account both the refraction and dispersion of the wavefield. The use of this imaging technique is subject to a number of assumptions. The dielectric properties of the ground are known (i.e., the complex permittivity as a function of the frequency). The ground is considered to be non-magnetic and therefore it is unequivocally characterized by its dielectric permittivity. The air-ground interface is assumed to be planar. The ground is supposed to be perfectly homogeneous out of the region occupied by the buried objects.

The numerical validation of the proposed subsurface imaging technique entails the implementation of highly complex integral-equation solvers taking into account the presence of the air-ground interface. In the frequency range of interest, this problem can only be tackled by using a multilevel fast-multipole method of moments code. This code must rigorously evaluate the dyadic half-space Green's function, requiring the evaluation of Sommerfeld integrals [122, 123, 124, 125, 126, 127, 128, 129]. As the development of such a simulation tool is out of the scope of the present Thesis, no full-wave numerical simulations are presented. Alternatively, the proposed imaging technique has been tested experimentally by running various 3-D SAR measurements in the anechoic chamber of the EMSL [60].

This Chapter is organized as follows. Section 6.2 introduces the formulation of the proposed subsurface imaging technique. Section 6.3 presents an measurement technique to characterize electromagnetically a soil sample. Section 6.4 is entirely devoted to the experimental testing of the imaging technique.

6.2   Formulation

The geometry of measurement is shown in Figure 6.1 (a), where a Tx/Rx antenna located off the ground illuminates the air-ground interface with a looking angle θ_i. The measurement system is supposed to function in the stepped-frequency mode. The antenna
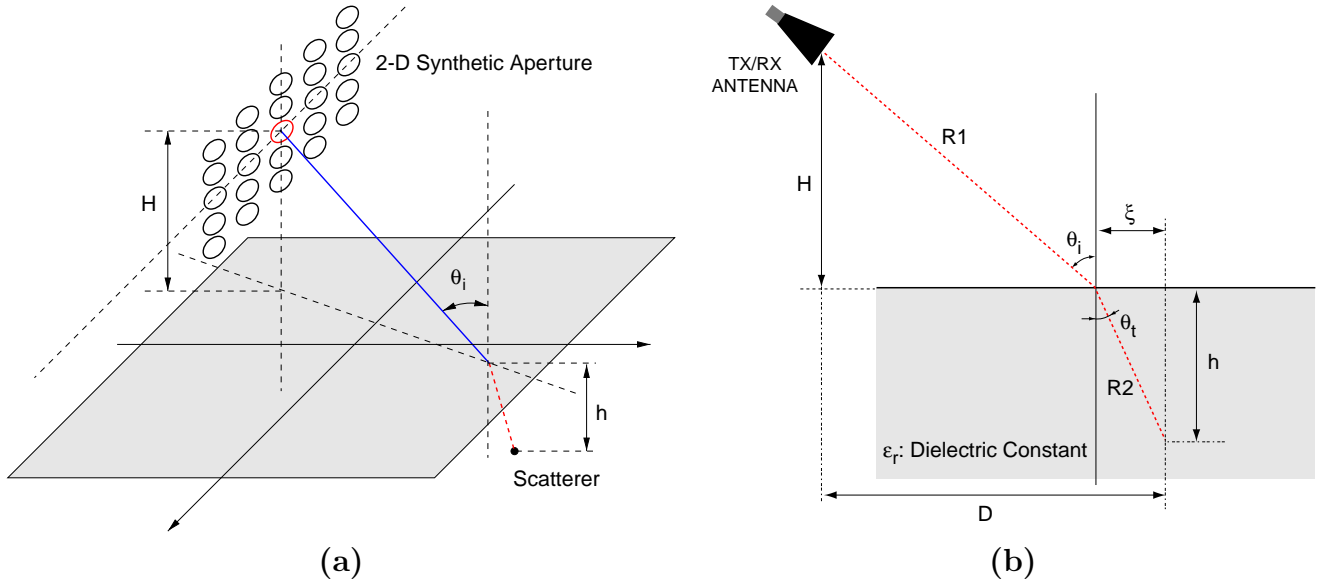
Figure 6.1. (a) Sketch of the 2-D synthetic aperture; (b) Propagation paths associated with the incident and refracted wavefields with a lossless ground.

platform is assumed to be capable of forming a 2-D synthetic aperture which will provide spatial resolution in the three dimensions.

In the processing of SAR data, it is usually assumed that the target consists of an ensemble of point scatterers whose response is independent of the observation angle. For subsurface sensing under the near-field condition, this assumption is usually not satisfied due to the presence of the air-ground interface. Consequently, a new class of focusing technique is required. The details of the implementation of this technique both with a lossless and lossy ground is next.

6.2.1   Lossless ground

Let us consider a point scatterer buried in a lossless ground at a depth h, its associated phase history will be defined by the electrical length of the two-way path travelled by an spherical wave from the antenna to the location of the point scatterer. Figure 6.1 (b) shows the propagation paths associated with the incident and refracted wavefields from the antenna to the location of the scatterer where the radar reflectivity is to be estimated. Assuming that these (generally spherical) wavefields are locally planar, one can estimate the electrical length corresponding to the propagation path through Snell's law of refraction [130] as follows

$$R = R_1 + R_2 = \sqrt{H^2 + (D - \xi)^2} + \sqrt{\epsilon_r} \, \sqrt{h^2 + \xi^2} \qquad (6.1)$$

where R_1 and R_2 are the electrical lengths in the air and in the medium, respectively; ϵ_r is the relative dielectric constant of the lossless medium, H is the height of the antenna, and ξ denotes the horizontal distance between the antenna and the point scatterer, which can be obtained by finding the zero of the following function,

$$
\begin{aligned}
F(\xi) &= sin\theta_i - \sqrt{\epsilon_r}\ sin\theta_r \\
&= \frac{D-\xi}{\sqrt{H^2+(D-\xi)^2}} - \sqrt{\epsilon_r}\frac{\xi}{\sqrt{h^2+\xi^2}}
\end{aligned}
\tag{6.2}
$$

Once the total electrical length R is determined for each antenna position, the reflectivity associated with the location of the scatterer can be estimated by convolving the backscatter data with a space-variant matched filter using that electrical length (i.e., instead of the two-way range to the point scatterer used in the free space case).

6.2.2 Lossy ground

When the medium is lossy the permittivity becomes complex ($\epsilon_r = \epsilon' - j\epsilon''$), see Figure 6.2, the planes of constant phase and those of constant amplitude do not coincide and the direction of propagation in the ground is determined by the normal to the constant phase
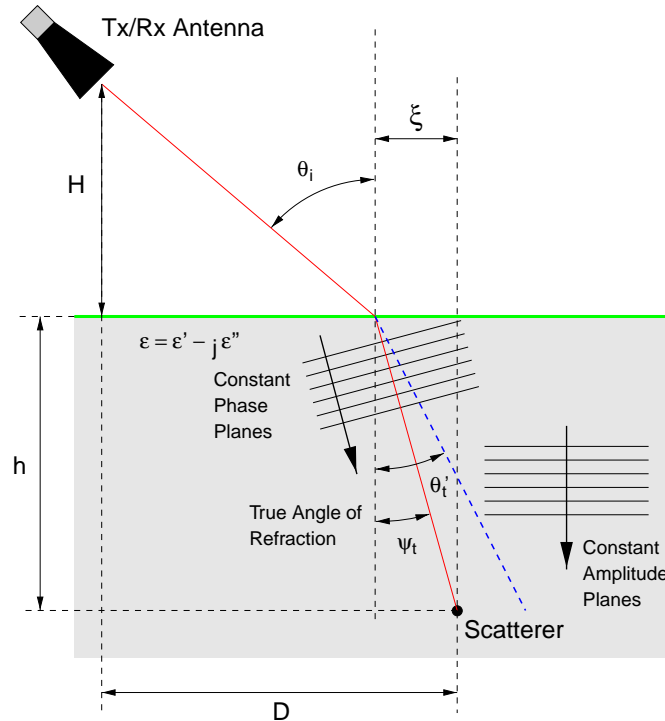
Figure 6.2. Scenario with a lossy medium surrounding a point scatterer.

planes $\hat{n}_\psi$, which is given by [131],

$$\tan \psi_t = \frac{\sqrt{2} \tan \theta_t'}{\sqrt{1 + \sqrt{1 + (\frac{2 \tan \delta}{\cos^2 \theta_t'})^2}}} \tag{6.3}$$

where $\tan \delta$ is the loss tangent and $\sin \theta_t' = \frac{\sin \theta_i}{\sqrt{\epsilon'}}$. The total electrical length is now expressed as

$$R = R_1 + n(\theta_i)R_2 = \sqrt{H^2 + (D - \xi)^2} + n(\theta_i)\sqrt{h^2 + \xi^2} \tag{6.4}$$

where $n(\theta_i)$ is the effective refractive index which depends on the incidence angle, and ξ is obtained by finding the zero of the following function

$$F(\xi) = \sin \theta_i - n(\theta_i) \sin \psi_t = \frac{D - \xi}{\sqrt{H^2 + (D - \xi)^2}} - n(\theta_i) \frac{\xi}{\sqrt{h^2 + \xi^2}} \tag{6.5}$$

with

$$n(\theta_i) = \sqrt{\epsilon'} \sqrt{\frac{1 + \sin^2 \theta_t'}{2} + \sqrt{\tan^2 \delta + (\frac{\cos^2 \theta_t'}{2})^2}} \tag{6.6}$$

wherein

$$\theta_t' = \arcsin(\frac{\sin \theta_i}{\sqrt{\epsilon'}}). \tag{6.7}$$

As in the lossless case, the total electrical length R given by the solution of Equation (6.5) is used in the matched filtering or focusing of the backscatter data.

It must be noted that getting an accurate estimate of the total electrical length R is subject to an priori knowledge of the dielectric properties of the medium surrounding the target of interest. A procedure for estimating the complex permittivity of a soil sample is suggested in Section 6.3. Furthermore, the relative position of the antenna referred to the air-ground interface must be precisely known.

6.2.3 Propagation and transmission losses

From a qualitative viewpoint (i.e., without making use of full-wave integral or differential equation solvers), the total propagation losses to "reach" the hidden object can be broken down as follows:

- Propagation losses from the antenna to the air-soil interface. The amplitude factor associated with this loss is given by

$$\mathrm{L}_{\text{free-space}} \simeq \frac{1}{R_1} \tag{6.8}$$

- Transmission losses through the air-soil interface, which will depend on the orientation of the electric field with respect to the incidence plane. For an electric field parallel to the incidence plane

$$T_\parallel = \frac{2\sqrt{\epsilon' - j\,\epsilon'' - \sin^2\theta_i}}{(\epsilon' - j\,\epsilon'')\cos\theta_i + \sqrt{\epsilon' - j\,\epsilon'' - \sin^2\theta_i}} \tag{6.9}$$

where $T_\parallel$ denotes the Fresnel transmission coefficient [130]. Alternatively, the Fresnel transmission coefficient for an electric field perpendicular to the incidence plane is

$$T_\perp = \frac{2\cos\theta_i}{\cos\theta_i + \sqrt{\epsilon' - \sin^2\theta_i - j\,\epsilon''}}. \tag{6.10}$$

- Propagation losses in the soil. The factor associated with this loss will be a function of scatterer depth h, i.e.

$$L_{\text{soil}} = \exp[-\alpha_e h] \tag{6.11}$$

wherein α_e denotes the attenuation constant in the ground, which is given by

$$\alpha_e = \frac{w}{c}\sqrt{\epsilon'}\,\sqrt{\frac{1}{2}\left[\sqrt{1 + \tan^2\delta} - 1\right]}. \tag{6.12}$$

As expected, the losses associated to (6.11) increase dramatically with an increasing frequency. In practice, if this loss is high there is no chance to get any backscatter signal from the buried object.

- Reflectivity losses of the object embedded in the ground. This loss factor will basically depend on the dielectric contrast between the buried object and its surrounding medium. The shape of the object and the direction of the incident wavefield are also expected to play an important role.

The resulting (two-way) total loss factor in dB can then be expressed as

$$\text{Total Loss [dB]} \simeq 40\,\log\left[L_{\text{free-space}}\,T_{\text{trans}}\,L_{\text{soil}}\,L_{\text{refl}}\right] \tag{6.13}$$

where T_{trans}, depending on the orientation of the incident electric field with respect to the incidence plane, can be either $T_\parallel$ or $T_\perp$. The term L_{refl} denotes the factor loss associated with the reflectivity of the object embedded in the ground.

When the incident electric field is parallel to the incidence plane, the loss factor in (6.13) can be minimized by choosing an incidence close to Brewster's angle. That would guarantee a total transmission of the radiated power into the ground, resulting in a maximum return from the buried object.

6.2.4   Subsurface imaging algorithm

Considering that the antenna is located within the near-field region of the illuminated spot on the ground, and its radiation pattern introduces a negligible distortion, then the 3-D complex reflectivity image can be estimated as follows [49],

$$I(\mathbf{r}) \simeq \int_f df \int_{\theta_a} d\theta_a \int_{\phi_a} E_s(f, \phi_a, \theta_a) \, F(\mathbf{r}, \mathbf{r_a}, f) \, d\phi_a \qquad (6.14)$$

where f is the working frequency, θ_a denotes the antenna viewing angle, ϕ_a is the aspect angle in azimuth, $E_s(\cdot)$ are the frequency domain backscatter data, and $F(\cdot)$ is a near-field focusing function (or space-variant matched filter) which can be expressed as

$$F(\mathbf{r}, \mathbf{r_a}, f) = \exp\left[j\frac{4\pi f}{c}(R - R_a)\right] \qquad (6.15)$$

where and c is the speed of light, R denotes the total electrical length between the antenna and the point with coordinates $\mathbf{r}$ given by (6.1) and (6.4), and R_a is the range to the origin of the coordinates system which, for convenience, is also the zero-phase reference point. This is a generalized imaging algorithm specially tailored for subsurface sensing.

Practical implementation aspects

It is important to note that the total electrical length R is always an even function of $(\phi - \phi_a)$ (i.e., it is a function of the relative distance between the antenna and the point with coordinates $\mathbf{r}$). As a result, the azimuth integration in (6.14) becomes a circular convolution in azimuth. This integration can therefore be efficiently implemented by using FFT techniques as a complex product in the azimuth wavenumber domain. This solution reduces the computational cost of the imaging algorithm from $O(N_f \ N_\phi \ N_\theta)$ down to $O(N_f \ \log_2 N_\phi \ N_\theta)$, where N_f is the number of frequency points measured and, N_ϕ and N_θ are, respectively, the number of aspect angles in azimuth and elevation.

Another important implementation aspect to be taken into account is that of finding the zero of the functions in (6.2) and (6.5). The adopted solution has been to use a simple Newton-Raphson's solver [93]. The convergence with a high accuracy was achieved in all cases in a minimum number of iterations. Further, in Eq. (6.14), the exact near-field phase history is accounted for by the exponential term of (6.15). On purpose, this term does not include an amplitude term correcting for the propagation loss given in (6.13) as its inclusion would reduce significantly the SNR of the resulting images.

6.3   Soil characterization

The detection capabilities of a surface penetrating radar can be significantly improved
through a precise characterization of the environment. For a non-magnetic medium, the
characterization reduces to the retrieval of the dielectric permittivity ϵ as a function of the
frequency. Once the dielectric permittivity is estimated, then one can form a subsurface
radar image precisely correcting both for the refraction of the wavefield and the dispersion.
The proposed characterization technique is simple and reasonably accurate. It is assumed
that, in the frequency range of interest, the permittivity shows a linear dependence with
the frequency.

The characterization is performed as follows. The sample of the soil under test is put
in an open box with low reflectivity walls (e.g., made of Rohacell) which has a metal
plate underneath. This sample is first measured with normal incidence. Then a second
measurement of the metal plate alone is carried out. Figure 6.3 shows the measurement
set-up used. The thickness of the sample d varies depending on the losses of the sample
measured. Since the backscatter fields are usually measured within a very wide frequency
range, a precise value for the thickness can be retrieved by using time domain reflectometry.

By combining the measurements with and without the sample on top of the metal
plate, an equivalence with transmission lines can be employed. This equivalence is shown
in Figure 6.4 (a). A photograph of the sample of the sandy soil is shown in Figure 6.4 (b).
By properly normalizing the measured backscatter one can obtain the reflection coefficient
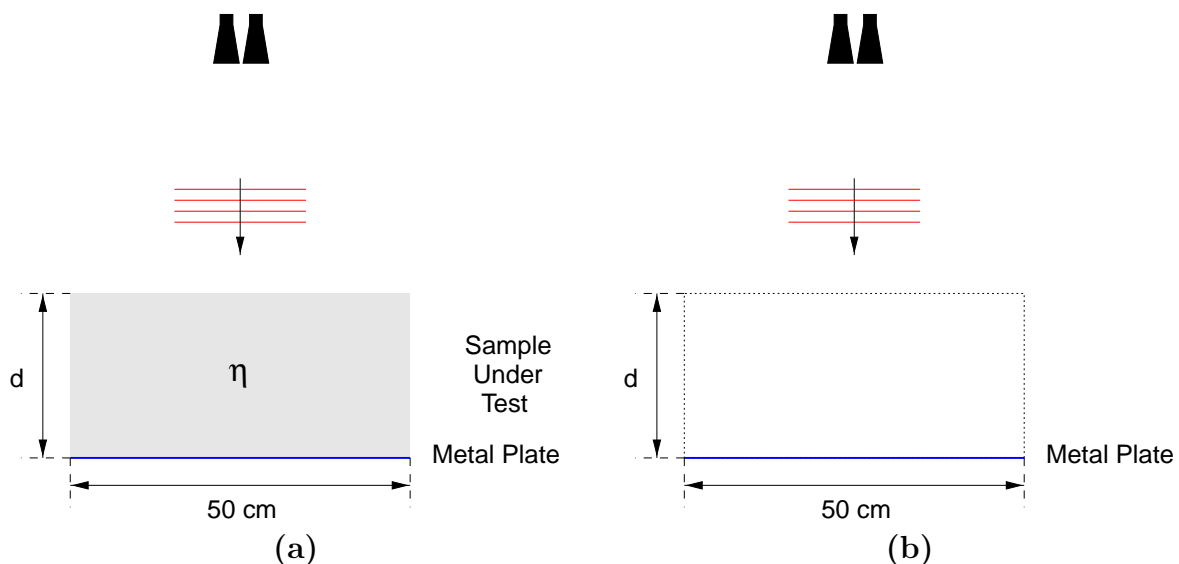
Figure 6.3.   Measurement set-up used in the characterization of the soils: (a) soil sample on
metal plate and (b) metal plate alone.
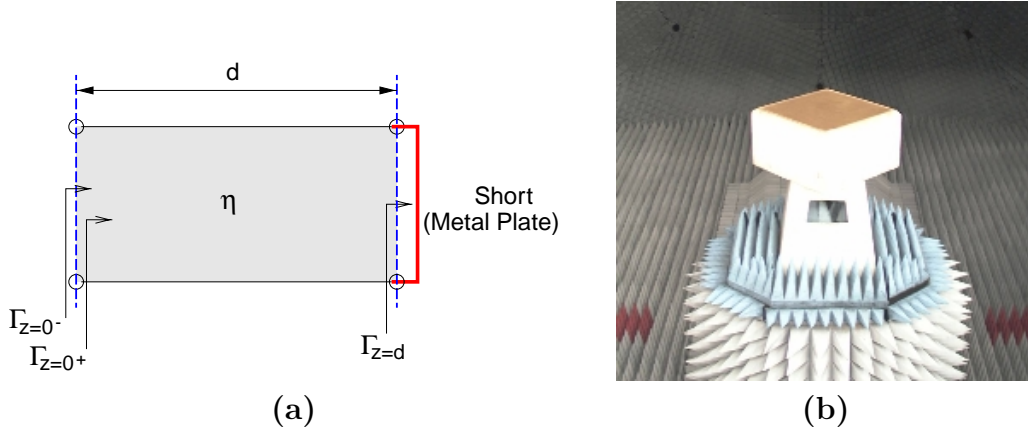
Figure 6.4. (a) Equivalence with transmission lines; (b) Sample of the sandy soil in the anechoic chamber.

Γ. The reflection coefficient is directly related to the dielectric permittivity as follows

$$\Gamma(f) = \frac{\tanh(j\dfrac{4\pi f}{c}\sqrt{\epsilon}\, d) - \sqrt{\epsilon}}{\tanh(j\dfrac{4\pi f}{c}\sqrt{\epsilon}\, d) + \sqrt{\epsilon}} \tag{6.16}$$

which corresponds to the reflection coefficient of a dielectric slab of thickness d under normal incidence [130].

A global error estimate integrated over the entire frequency band is then defined as

$$E = \int_f |\log(\frac{\Gamma_{\mathrm{ms}}(f)}{\Gamma(f)})|^2 \, df \tag{6.17}$$

The proposed procedure to retrieve the complex permittivity is based on an optimization which minimizes the error estimate given by (6.17).

This characterization technique has been tested on various types of soil. The frequency range used in these measurement ranged from 1.5 to 9.5 GHz. As an example, Figures 6.5 (a)-(d) show, respectively, the estimated complex permittivity (real and imaginary parts) and the corresponding reflection coefficient (in the frequency and time domains) for a sample of a sandy soil of thickness 5 cm with a moisture level of 5%. As expected with a sample of a sandy soil with low moisture [132], the real part of the complex permittivity is almost independent of the frequency, ranging from 2.5 to 2.7. On the other hand, the imaginary part is extremely low and below 0.03. The global error resulting from the optimization in this measurement was 0.29 dB. Figures 6.5 (e)-(h) show the estimated complex permittivity and the corresponding reflection coefficient (in the frequency and time domains) for the same sample of sandy soil with a moisture level of 10%. The retrieved real and imaginary parts of the complex permittivity are higher than those

for the moisture level of 5%, in agreement with the increase of the volumetric moisture. The global error resulting from the optimization in this measurement was 0.52 dB. In these two measurements, the reflection coefficient given by the model and that measured show are in perfect agreement both in the frequency and the time domains. These results indicate that the model used is appropriate to characterize soil samples by means of a stepped-frequency radar.

A soil sample consisting of a mixture of about 80% of gravel and 20% of dry sand was also characterized. The thickness of this sample was 10 cm. Figures 6.6 (a)-(d) show, respectively, the estimated complex permittivity (real and imaginary parts) and the corresponding reflection coefficient (in the frequency and time domains) for the mixture of gravel and sand. It is seen that the real part of the complex permittivity shows no dependence with the frequency and its value is about 3.4. The integrated error resulting from the optimization was 0.62 dB.

6.4   Experimental results

The proposed subsurface imaging algorithm has been tested experimentally with a series of three measurements carried out in the anechoic chamber of the EMSL [60].

In the first measurement, the target used consisted of an ensemble of 8 metallic spheres of radius 7.62 cm. The spheres were all buried in a cylindrical container of diameter 2 m and depth 0.5 m. The container was filled up with a sandy soil with a moisture in the order of 5%. The disposal of the spheres in the container is shown in Figure 6.7. The frequency range employed in this measurement was 2 to 6 GHz, sampling a total of 401 frequency points. The synthetic aperture was spherical with a radius of 9.56 m. The angular ranges of the aspect angles in azimuth and elevation were $0° \leq \phi \leq 45°$ and $22.5° \leq \theta \leq 67.5°$, respectively. The corresponding angular steps were both 0.75°. This results in a total of 3721 antenna positions uniformly distributed on the spherical aperture. The measurement time needed to collect the frequency backscatter data was about three entire days.

A 3-D SAR image within the volume of the cylindrical container was reconstructed through (6.14). The dielectric permittivity used in the matched filter of (6.14) was that retrieved from the characterization of the sample of the sandy soil with moisture 5% presented in Section 6.3. The 3-D image consisted of 10 horizontal slices uniformly spaced within the depth range $-70 \leq z \leq -20$ cm. On each horizontal slice, the reflectivity was estimated at points forming a polar raster with $N_\rho = 51$ and $N_\phi = 180$. Figure 6.8 shows eight horizontal slices out of the resulting 3-D SAR image within the depth range $-42 \leq z \leq 0$ cm. The dynamic range shown in these images is 40 dB. The polarization of the
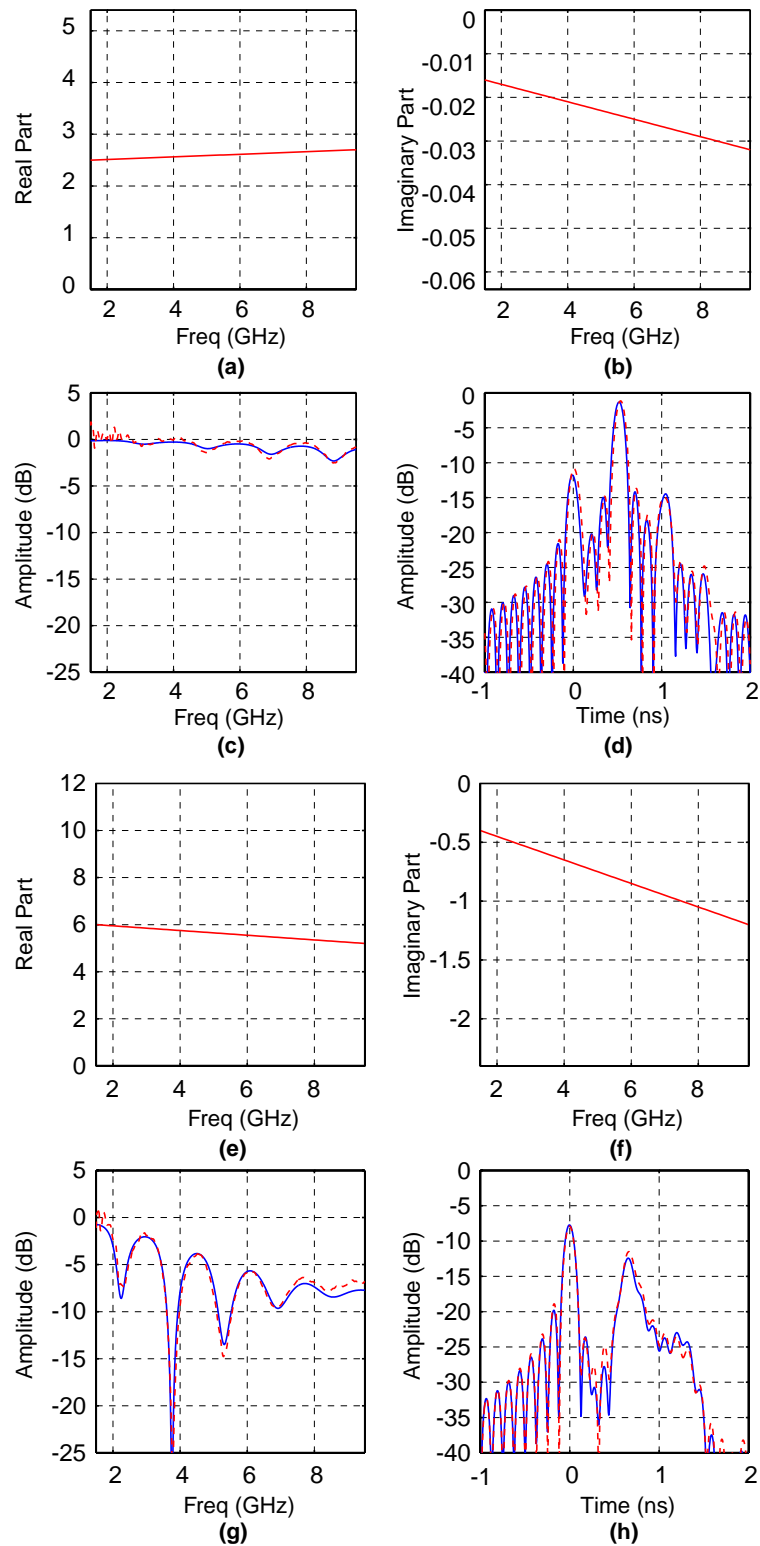
Figure 6.5. Characterization results with the sample of sandy soil (moisture level of 5%/10%): (a/e) real and (b/f) imaginary part of the complex permittivity, measured (red dashed line) and retrieved (blue solid line) reflection coefficient in the frequency domain (c/g) and time domain (d/h).
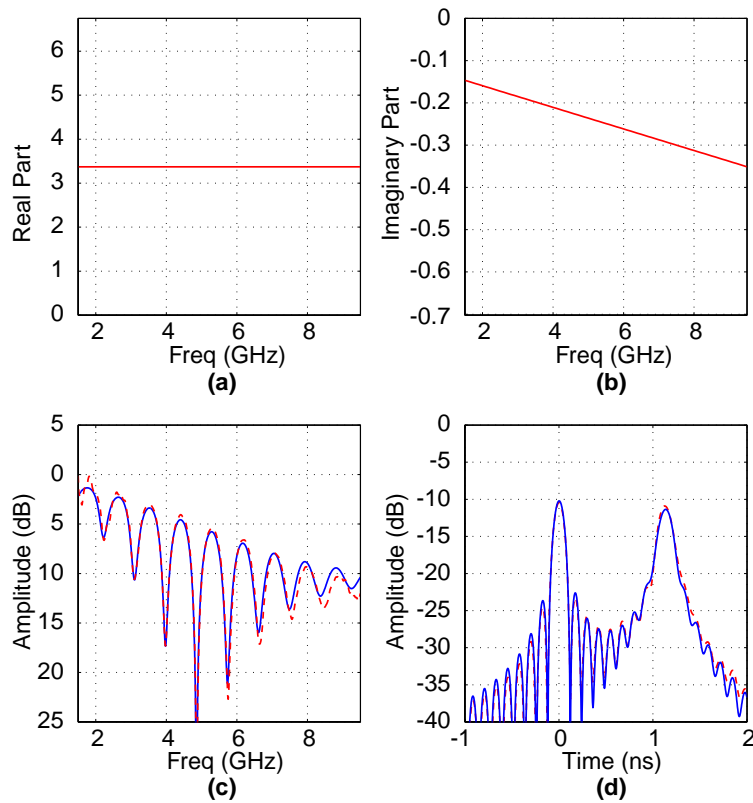
Figure 6.6. Characterization results with the mixture of gravel and sand: (a) real and (b) imaginary part of the complex permittivity, measured (red dashed line) and retrieved (blue solid line) reflection coefficient in the frequency domain (c) and time domain (d).

incident wavefield corresponding to these images was HH (i.e., electric field perpendicular to the plane of incidence). A Kaiser-Bessel ($\alpha = 2$) window [87] along the three dimensions of the frequency domain data set was applied prior to the formation of the image. It is seen that the eight spheres are reconstructed at their actual positions. This result indicates that the geometric distortion in the image due to the refraction and dispersion has been successfully corrected. As expected, the deeper spheres show a slightly lower reflectivity due to the propagation loss in the sandy soil. The processing time on a Sun workstation, equipped with a 64 bit processor and 384 MByte of internal memory, was about 4 hours.

In the second measurement, the same cylindrical container was again filled up with a sandy soil with moisture 5%. Seven mine-like objects were buried at the depth of 15 cm, as shown in Figure 6.9. The mine-like objects were three inert landmines provided by the Italian Army, a simulant mine provided by the US Army, a stone, a Coke can, and a wooden rod. The dimensions of the three Italian landmines, the US simulant, and the stone were about the same: 10 cm. The length of the wooden rod was 30 cm. The US simulant was filled with RTV-3110 silicon rubber, which presents a dielectric permittivity
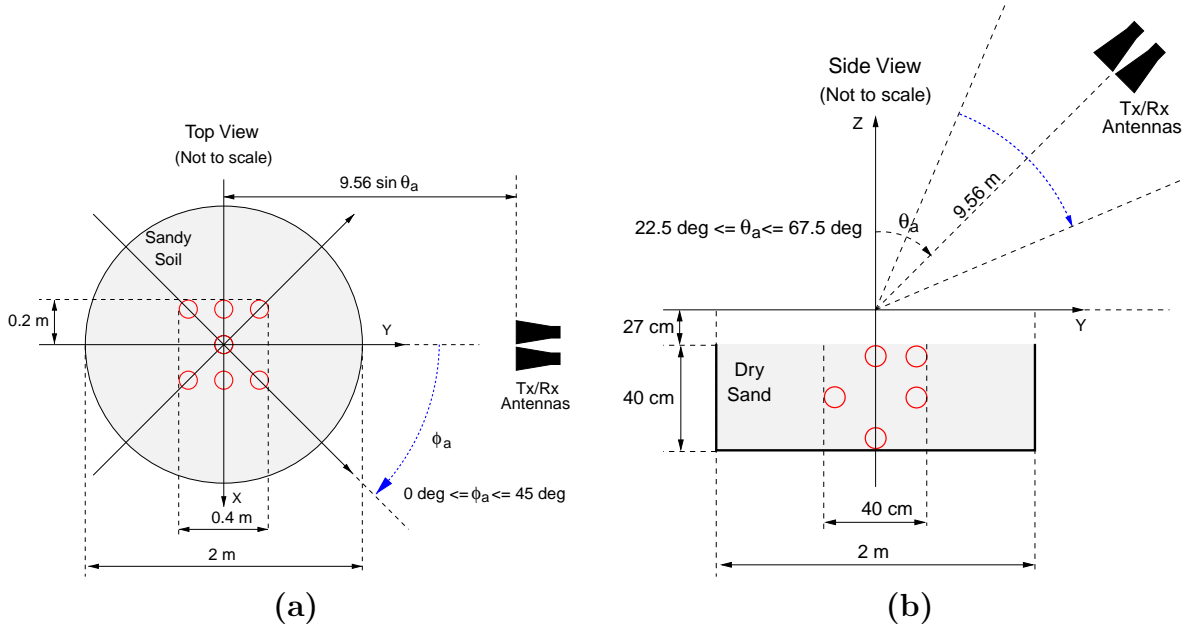
Figure 6.7. Sketch of the measurement set-up with the eight spheres buried in the sandy soil: (a) top view and (b) side view.

of about 2.9. The resulting dielectric contrast between this simulant and the sandy soil is therefore extremely low. The wooden rod is also expected to present a low dielectric contrast [132].

This measurement was performed within the frequency range 1.5 to 9.5 GHz, sampling a total of 801 points. Such a wide frequency range is only appropriate when the propagation losses in the ground are low. A 2-D spherical aperture with an angular spans of $12°$ both in azimuth and elevation was synthesized, as shown in Figure 6.9. The corresponding angular ranges were $-6° \leq \phi \leq +6°$ and $39° \leq \theta \leq 51°$. The angular steps in azimuth and elevation were both $0.25°$, resulting in a total of 2401 antenna positions uniformly distributed on the spherical aperture.

As in the previous measurement, a 3-D SAR image within the volume of the cylindrical container was reconstructed through (6.14). The dielectric permittivity used in the matched filter of (6.14) was that retrieved from the characterization of the sample of the sandy soil with moisture 5%. The 3-D image consisted of 10 horizontal slices uniformly spaced within the depth range $-70 \leq z \leq -20$ cm. On each horizontal slice, the reflectivity was estimated at points forming a polar raster with $N_\rho = 51$ and $N_\phi = 180$.

Figure 6.8 shows three horizontal slices at depths 5, 15, and 25 cm. The dynamic range shown in these images is 40 dB. The polarization of the incident wavefield corresponding to these images was VV (i.e., electric field parallel to the plane of incidence). A Kaiser-
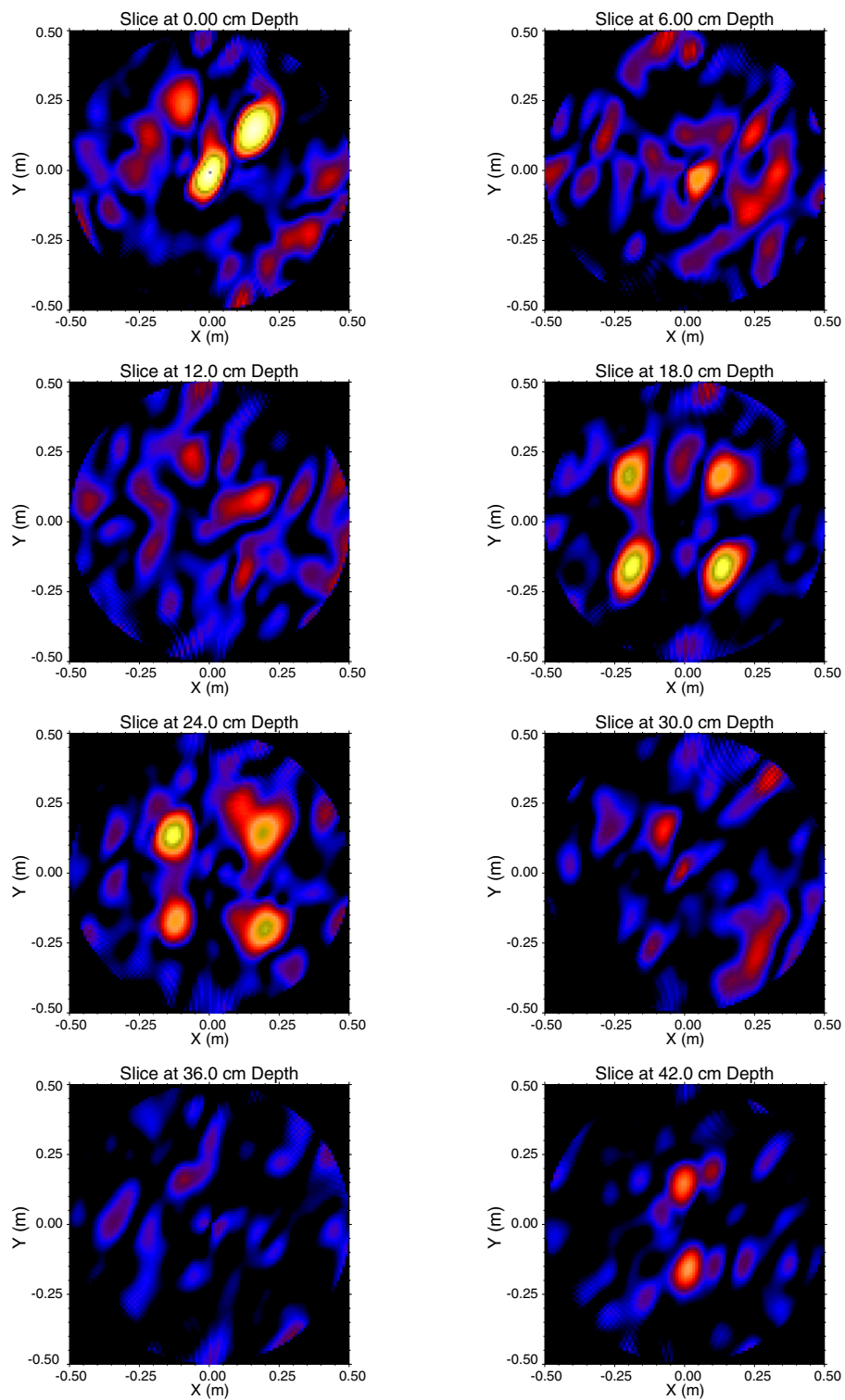
Figure 6.8. Eight horizontal slices out of the 3-D SAR image of the eight buried spheres within the depth range $-42 \leq z \leq 0$ cm.
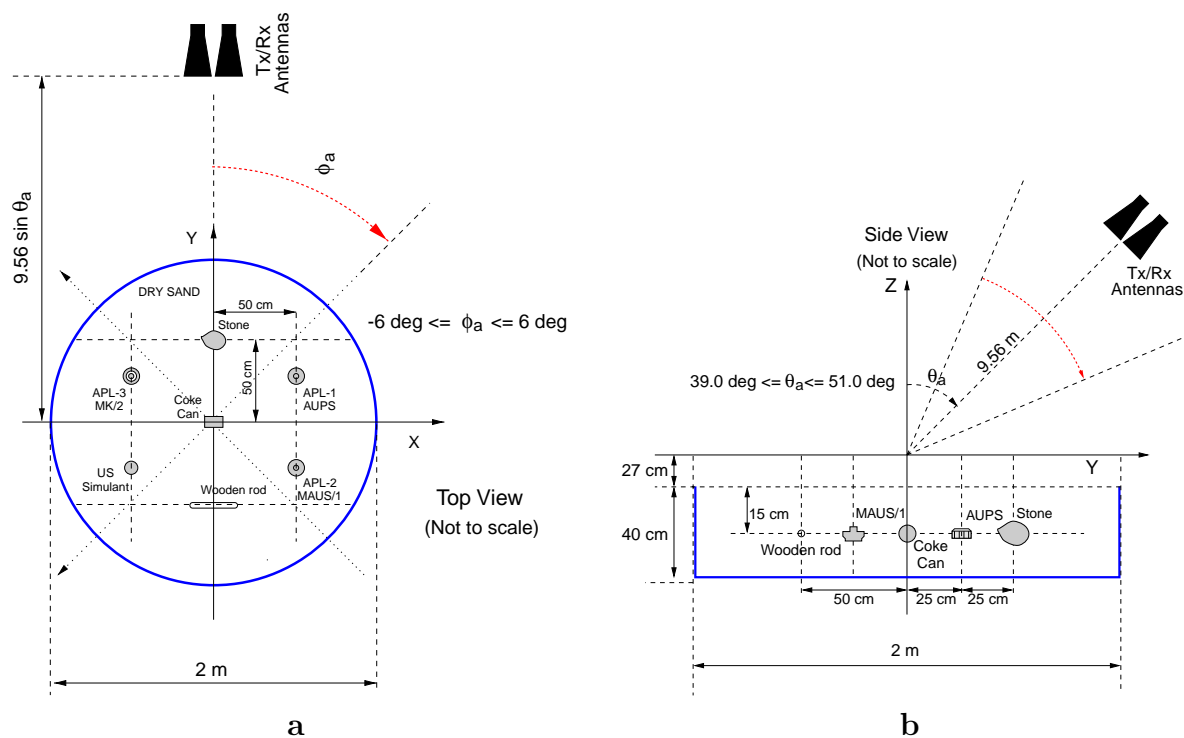
Figure 6.9. Sketch of the experimental set-up used in the 3-D SAR measurement: (a) top and (b) side view.

Bessel ($\alpha = 2$) window [87] along the three dimensions of the frequency domain data set was applied prior to the formation of the image. The slice at 15 cm depth shows five out of the seven buried objects imaged at their actual position. This result indicates that both the characterization of the soil and the image reconstruction can be combined to get high quality subsurface imagery. Neither the US simulant nor the wooden rod are visible due to their low dielectric contrast. The projection of the return from the far-range edge of the container is visible in the three slices because of the limited resolution in the direction perpendicular to the illumination direction.

In the last measurement the sandy soil in the cylindrical container was watered until a moisture level of 10% was reached. The collection of the backscatter data took place well after in order to have an homogenous distribution of the volumetric moisture. The propagation losses in this measurement are expected to be much higher than those in the previous case. Therefore it is advisable to reduce accordingly the span and center frequency of the frequency range. The adopted solution was to double the angular spans of the spherical aperture and halve the frequency range. This was found to be the optimum solution to get a resolution in the images comparable with those of the sandy soil with 5% moisture. Thus, the angular spans of the aperture in azimuth and elevation were,
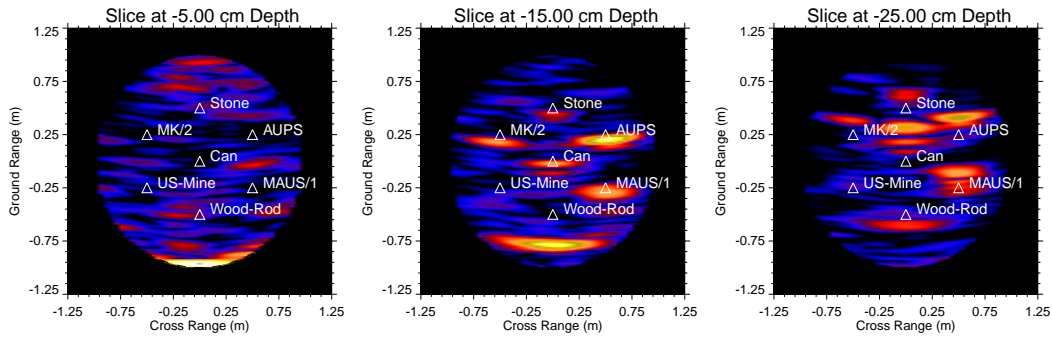
Figure 6.10. Set of horizontal subsurface slices out of the 3-D SAR image in the VV polarization (sandy soil with 5% moisture).
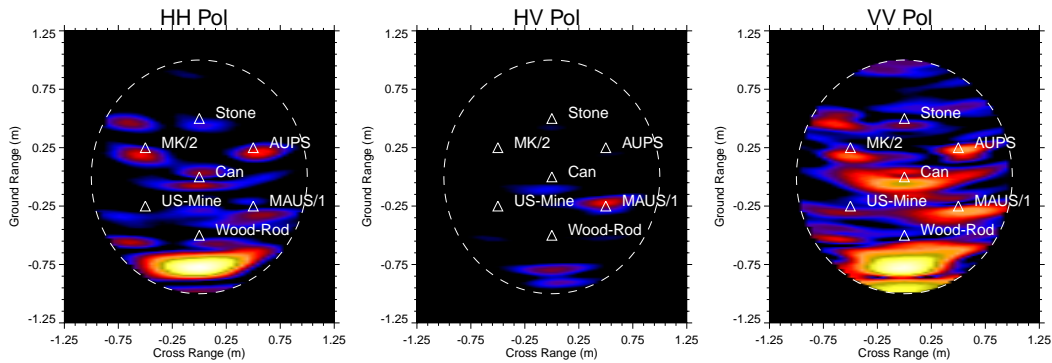
Figure 6.11. Horizontal slices at 15 cm depth in the HH, HV and VV polarizations (sandy soil with 10% moisture).

respectively, $-12° \leq \phi \leq +12°$ and $33° \leq \theta \leq 54°$. The angular steps in azimuth and elevation were both $0.5°$.

Figure 6.11 shows the reconstructed images at 15 cm depth for the three polarizations. The dielectric permittivity used in the matched filter of (6.14) was that retrieved from the characterization of the sample of the sandy soil with moisture 10% presented in Section 6.3. It is seen that all the objects except the US simulant and the wooden rod were again successfully imaged at their actual positions. As expected with axis-symmetric objects (i.e., bodies of revolution), the reconstructed reflectivity is much lower in the HV channel for all the buried objects apart from one of the APLs and the Coke can. It is seen that the objects reflectivity is clearly higher in the VV image because of the higher transmission coefficient when approaching Brewster's angle. The selection of an incidence angle close to that angle guarantees an optimum transmission of power into the ground.

Conclusion

The research conducted in this Thesis dealt with the development of a family of three-dimensional (3-D) near-field synthetic aperture radar (SAR) imaging algorithms, which have all been tested by means of numerical simulations and measurements. The main motivation in developing these algorithms was the formation of high quality radar imagery at the lowest computational cost. A total of five imaging algorithms were implemented, each satisfying different requirements in terms of computational cost, quality of the resulting imagery, type of the scanning geometry, and implementation complexity. These algorithms are:

RMA: The Range Migration Algorithm was introduced in Section 3.2. This algorithm is an extension of the two-dimensional (2-D) RMA. Its formulation has been justified by using of the method of stationary phase (MSP). The numerical simulations have shown the efficiency of the algorithm, which can be simply implemented by using FFT codes and a one-dimensional (1-D) Lagrange interpolator. An important feature of the proposed processing scheme is that, by applying a phase correction term, strip-map SAR measurements can be performed at the spotlight SAR sampling rate without introducing any degradation in the quality of the resulting imagery. The quality of the focused images is very high, and in the numerical simulations it has shown to reach dynamic ranges better than 100 dB. The algorithm has been also tested experimentally using a ground-based SAR system. These results have shown the high performance of the algorithm working with an experimental data set.

RMA-FT: A Range Migration Algorithm with Fields Translation from spherical and cylindrical apertures onto a planar aperture was presented in Sections 3.3 and 3.4. The use of the 3-D RMA was successfully extended to cylindrical and spherical scanning geometries by splitting the image formation into two steps. The frequency

domain backscatter data are first translated to a planar aperture in the vicinity of the measurement aperture. Then the 3-D range migration algorithm (RMA) is applied. Results showed that the presented backpropagation technique does not entail a significant increase of the computational cost. Furthermore, the proposed field translation does not degrade the quality of the imagery. The dynamic range of the images was shown to be basically identical to that obtained with the 3-D RMA without the fields translation.

SVMFIA: A Space-Variant Matched Filter Imaging Algorithm especially tailored for spherical scanning geometries was introduced in Section 4.2. This is a near-field imaging technique which accounts precisely for the wavefront curvature and the free space propagation loss. The core of the algorithm resides in the calculation of a near-field focusing operator, which is convoluted with the frequency-domain backscatter data in the azimuth domain. The algorithm makes use of an efficient computational procedure based on FFT codes and an asymptotic evaluation with the MSP. This asymptotic evaluation is optimized by using working matrices with the points of stationary phase and their second order derivatives. Experimental results showed a remarkable performance in terms of focusing capabilities and spatial stability of its impulse response.

The practical problem motivating the development of the SVMFIA algorithm was the formation of a 3-D near-field SAR image of a 5 m high Fir tree. This tree was measured in the anechoic chamber of the European Microwave Signature Laboratory (EMSL) using the spherical scanning geometry. The images focused with the SVMFIA were used to identify the major backscattering sources within the tree volume: the trunk in the top part of the tree; the needles and the branches in the middle and bottom part of the tree (where a significant anisotropic behavior has been observed). The overall shape of the resulting 3-D radar images of the tree were surprisingly close to that of the optical images. Eventhough the backscattering behavior of the tree at radar frequencies is by far more complicated and radically different from that in the visible range.

PFA-IR: A Polar Format Algorithm with Image Rectification was assessed in Section 4.3. This technique allows the use of FFT-based focusing algorithms normally used under the far-field condition. The resulting geometric distortion due to the short observation distance is successfully corrected by applying a rectification algorithm. A rectification algorithm especially designed for a near-field 3-D SAR processor was developed. Results on simulated and experimental data showed that this technique

is highly efficient and can be easily implemented using FFT codes and a 3-D Lagrange interpolator.

SVMF-SSA: A Space-Variant Matched Filter Subsurface Sensing Algorithm was outlined in Chapter 6. This imaging algorithm is especially tailored for 3-D subsurface radar imaging. A simple and effective characterization technique was used to retrieve the dielectric permittivity of the medium surrounding the subsurface objects was presented. The proposed soil characterization and subsurface imaging techniques were tested experimentally successfully. The measurements were carried out in an anechoic chamber using a stepped frequency radar which synthesized a spherical aperture. The resulting subsurface images show that the geometric distortion due to the refraction and dispersion of the wavefields is minimum both with lossless and lossy grounds.

Table 7.1. Main characteristics of the five near-field imaging algorithms.

Algorithm	Computational Cost	Scanning Geometry	Image Quality	Implementation Complexity
RMA	Minimum	Planar	High	Minimum
RMA-FT	Medium	Cylindrical/Spherical	High	Medium
SVMFIA	Medium to High	Spherical	High	High
PFA-IR	Minimum	Spherical	Medium	Minimum
SVMF-SSA	Medium to High	Cylindrical/Spherical	High	Medium

The main characteristics of the above-listed five imaging algorithms are summarized in Table 7.1.

As the overall conclusion, it can be said that a complete set of novel near-field imaging algorithms has been successfully developed. These algorithms have all been tested by means of numerical simulations and, most important, radar measurements in an anechoic chamber.

Formulation of the 3-D RMA using the MSP

The derivation of the 2-D Fourier Transform of the focusing function in (3.5) is based on the MSP. This method provides an analytical solution for the asymptotic expansion of an integral of the form

$$N(k) = \iint\limits_{R} f(x,y)\, e^{jk\mu(x,y)}\, dx\, dy \tag{A.1}$$

where R is a region in the xy plane and $\mu(x,y)$ is assumed to be twice-continuously differentiable in R. Then, the behavior of $N(k)$ for $k \to \infty$ can be determined by means of the MSP [73].

From now on the formulation is adapted in order to evaluate the following integral

$$I(k_x, k_z) = \iint e^{jk_r\sqrt{x^2+(y-y_a)^2+z^2}}\, e^{-jk_x x - jk_z z}\, dx\, dz \tag{A.2}$$

By comparing (A.2) with (A.1), it is seen that $f(x,z) = 1$, and the phase of the exponential term equals

$$\Phi(x,z) = k\mu(x,z) = k_r R - k_x x - k_z z \tag{A.3}$$

$$R = \sqrt{x^2 + (y-y_a)^2 + z^2} \tag{A.4}$$

The MSP states that the asymptotic expansion of $I(k_x, k_z)$ results

$$I(k_x, k_z) \simeq \frac{j2\pi}{\sqrt{\Phi_{xx}\Phi_{zz} - \Phi_{xz}^2}} e^{j\Phi(x_0,z_0)} \tag{A.5}$$

where Φ_{xx}, Φ_{zz} and Φ_{xz} denote the second partial derivatives of $\Phi(x,z)$ evaluated at the stationary point. The stationary point (x_0, z_0) is the point where the phase $\Phi(x,z)$ takes

an extreme value, i.e.,

$$\frac{\partial \Phi}{\partial x}\bigg|_{(x_0, z_0)} = 0 \tag{A.6}$$

$$\frac{\partial \Phi}{\partial z}\bigg|_{(x_0, z_0)} = 0 \tag{A.7}$$

and it is assumed that

$$\Phi_{xx}\Phi_{zz} - \Phi_{xz}^2 \neq 0 \qquad \Phi_{zz} \neq 0 \tag{A.8}$$

The first derivatives of the phase function are:

$$\Phi_x(x, z) = \frac{\partial \Phi}{\partial x} = -k_x + \frac{k_r x}{R} \tag{A.9}$$

$$\Phi_z(x, z) = \frac{\partial \Phi}{\partial z} = -k_z + \frac{k_r z}{R} \tag{A.10}$$

There is only one point were both first derivatives are simultaneously zero:

$$x_0 = \frac{k_x(y - y_a)}{\sqrt{k_r^2 - k_x^2 - k_z^2}} \tag{A.11}$$

$$z_0 = \frac{k_z(y - y_a)}{\sqrt{k_r^2 - k_x^2 - k_z^2}} \tag{A.12}$$

The second partial derivatives are:

$$\Phi_{xx}(x, z) = \frac{\partial^2 \Phi}{\partial x^2} = \frac{k_r \left[z^2 + (y - y_a)^2\right]}{R^3} \tag{A.13}$$

$$\Phi_{zz}(x, z) = \frac{\partial^2 \Phi}{\partial z^2} = \frac{k_r \left[x^2 + (y - y_a)^2\right]}{R^3} \tag{A.14}$$

$$\Phi_{xz}(x, z) = \frac{\partial^2 \Phi}{\partial x \partial z} = -\frac{k_r x z}{R^3} \tag{A.15}$$

which evaluated at the stationary point yield,

$$\Phi_{xx}(x_0, z_0) = \frac{(k_x^2 - k_r^2)\sqrt{k_r^2 - k_x^2 - k_z^2}}{k_r^2 (y - y_a)} \tag{A.16}$$

$$\Phi_{zz}(x_0, z_0) = \frac{(k_z^2 - k_r^2)\sqrt{k_r^2 - k_x^2 - k_z^2}}{k_r^2 (y - y_a)} \tag{A.17}$$

$$\Phi_{xz}(x_0, z_0) = \frac{k_x k_z \sqrt{k_r^2 - k_x^2 - k_z^2}}{k_r^2 (y - y_a)} \tag{A.18}$$

Moreover, the phase at the stationary point is

$$\Phi(x_0, z_0) = \sqrt{k_r^2 - k_x^2 - k_z^2} \, (y_a - y) \tag{A.19}$$

Finally, substituting (A.16)-(A.19) into (A.5) for evaluating (A.2), and calling $k_y = \sqrt{k_r^2 - k_x^2 - k_z^2}$, the 2-D FT results in the expression

$$I(k_x, k_z) \simeq \frac{j2\pi(y - y_a)k_r}{k_y^2} \, e^{jk_y(y_a - y)} \tag{A.20}$$

When applying (A.20) to the actual RMA implementation, the factor $(y - y_a)$ is not used because y is not defined in the $\omega - k$ domain. This omission does not produce any relevant effect on the final image quality. Anyway, as stated in Sect. 3.2.3, the final result is usually equalized along the slant-range direction, thus erasing the influence of this omission.

Accuracy of the translation of 2-D backscattered fields

Let's consider an ensemble of M identical line scatterers, parallel to the z-axis, randomly distributed inside a cylinder of radius $\rho_{\min}$, as shown in Figure B.1. For the sake of simplicity, all line scatterers are assumed to show the same reflectivity and that is equal to one.

Provided the interaction between the line scatterers can be neglected, the backscattered fields on the surface of a cylinder with radius ρ (with $\rho \geq a$) take the form

$$E_s(\rho, \phi) = \sum_{i=1}^{M} \left(\frac{j}{4} \, H_0^{(2)}(\frac{k_r}{2} \sqrt{\rho^2 + \rho_i^2 - 2\rho\rho_i \cos(\phi - \phi_i)}) \right)^2 \tag{B.1}$$

with $k_r = 4\pi f/c$, where k_r denotes the frequency wavenumber, f is the working frequency, c is the speed of light, $H_0^{(2)}(\cdot)$ is the zeroth order Hankel function of second kind, and (ρ_i, ϕ_i) are the cylindrical coordinates of the line scatterer ith. The fields given by (B.1) will be considered as the reference in the calculation of the error introduced in the fields translation.

At this point one makes use of the model of the "radiating reflectors". If the line scatterers are assumed to radiate simultaneously a wavefield which propagates at a velocity which is one half of the actual value, then the backscattered fields can be approximated as a solution of the 2-D Helmholtz equation. Thus, the backscattered fields on the surface of the cylinder of radius ρ can alternatively be expressed as

$$\hat{E}_s(\rho, \phi) = \sum_{n=-\infty}^{+\infty} a_n \, H_n^{(2)}(k_r \rho) \, e^{jn\phi} \tag{B.2}$$

In practice the summation in (B.2) will be always truncated at the limit $|n| \leq N$. The value of N depends on the radius of the minimum cylinder that encloses entirely the ensemble of line scatterers $\rho_{\min}$ as follows

$$N \simeq [k_r \rho_{\min}] + n_1, \tag{B.3}$$

where the square brackets denote the integer part of the number in between, and n_1 is an integer which depends on the accuracy required.

An estimate for the error introduced by the translation of 2-D backscattered fields has been obtained as follows. First, the exact backscattered fields given by (B.1) on the surface of a cylinder of radius ρ are calculated at a number of azimuth angles N_ϕ high enough to satisfy the Nyquist criterion (i.e., such that $N_\phi \geq 2N$). These fields are then used to obtain the amplitudes of the cylindrical modes a_n in (B.2). Note that these amplitudes can be readily calculated by means of a DFT as follows

$$a_n = \frac{\mathbf{DFT}[Es(\rho, \phi_i)]}{H_n^{(2)}(k_r \ \rho)} \tag{B.4}$$

with $n = -N, \dots, 0, \dots, N$, and $i = 0, \dots, N_\phi - 1$.

Once the amplitudes of the cylindrical modes are known, the fields can be backpropagated to the surface of a concentric cylinder of radius ρ', with $\rho, \ \rho' \geq \rho_{\min}$. The translated fields are given by

$$\hat{E}_s(\rho', \phi) = \sqrt{\frac{\rho'}{\rho}} \sum_{n=-N}^{+N} a_n \ H_n^{(2)}(k_r \rho') \ e^{jn\phi} \tag{B.5}$$

The amplitude factor $\sqrt{\rho'/\rho}$ is introduced to correct for the additional one-way propagation path not taken into account in the model.

The error introduced by the proposed field translation technique can be simply obtained as the difference between the exact backscattered fields, calculated by means of (B.1), and those given by (B.5). The translation error is defined as follows

$$\text{Error}(f, \rho, \rho') \ [\%] = 100 \times \frac{\sum\limits_{i=0}^{N_\phi - 1} |E_s(\rho', \phi_i) - \hat{E}_s(\rho', \phi_i)|^2}{\sum\limits_{i=0}^{N_\phi - 1} |E_s(\rho', \phi_i)|^2} \tag{B.6}$$

As an example, Figure (B.2) shows the fields translation error for an ensemble of $M = 9$ line scatterers enclosed in a cylinder of radius $\rho_{\min} = 1 \ m$ at the frequencies of 2,
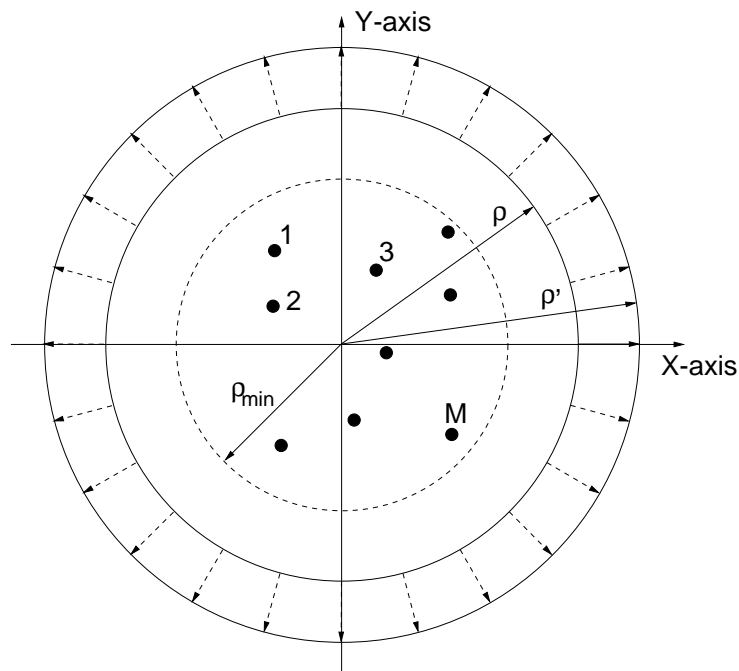
Figure B.1. Ensemble of M line scatterers.

6, 10, and 14 GHz. The considered radius of the measurement cylinders are $\rho =5$, 10 and 15 m. The corresponding radius where the fields have been translated range from 0.8ρ to 1.2ρ (i.e., the fields are translated both in the forward and backward direction). As expected, the translation error increases with a increasing distance from the measurement cylinder ρ. It is important to note that the magnitude of the error seems to be almost independent of the frequency. Further, the translation error in the backward direction is higher than that in the forward direction. As an example, with a measurement cylinder the radius used in the experiment, the error within the range of ρ' from 8 to 12 m is well below 1.5%, which is in practice negligible.
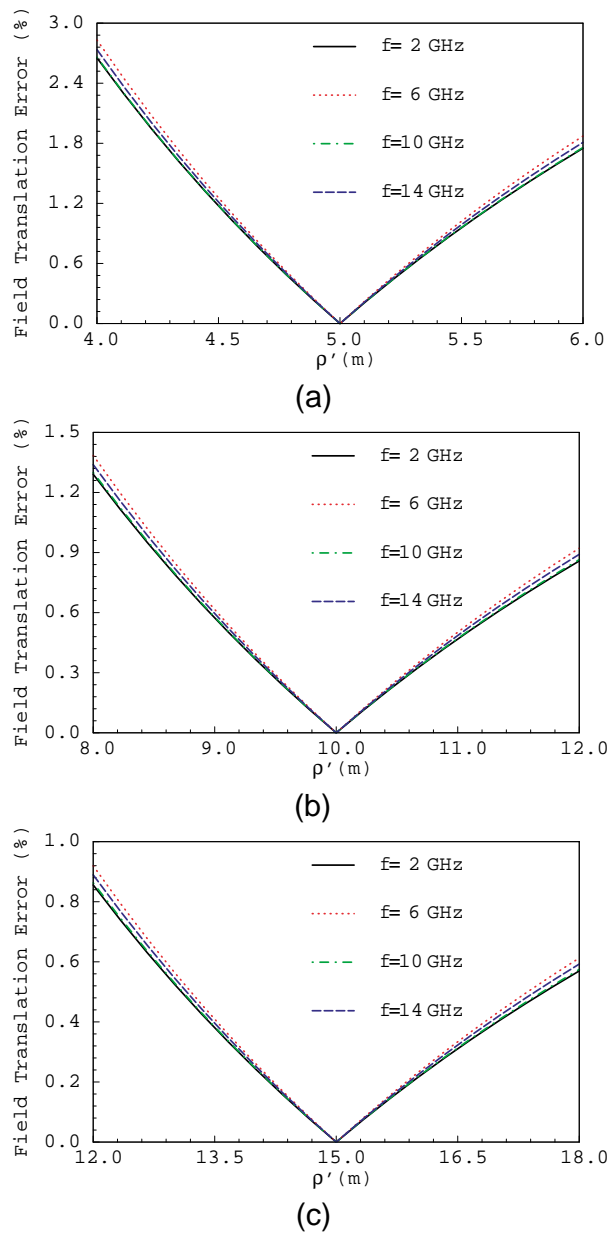
Figure B.2. Estimated errors with 9 line scatterers at 2, 6, 10 and 14 GHz for measurement cylinders of radius 5 m (a), 10 m (b) and 15 m (c).

Evaluation of the coefficients $c_{m,n}$

The analytical expressions for the evaluation of the amplitudes of the spherical harmonics $c_{m,n}$ in (3.32) were given in Section 3.4.1. From a computational viewpoint, the evaluation of the coefficients $c_{m,n}$ reduces to the calculation of the two integrals: the integral in ϕ of (3.39) and that in θ of (3.42):

$$c_m(r_a, \theta) = \frac{1}{2\pi} \int_0^{2\pi} \psi(r_a, \phi, \theta) e^{-jm\phi} \, d\phi \tag{C.1}$$

$$c_{m,n}(r_a) = \left(\frac{m}{|m|}\right)^m \int_0^{\pi} c_m(r_a, \theta) \, \overline{P}_n^m(\cos\theta) \sin\theta \, d\theta. \tag{C.2}$$

Let us assume that the backscattered fields are measured on the surface of radius $r = r_a$ at points forming a grid uniformly sampled in ϕ and θ, and the number of spherical harmonics used in the modal expansion of (3.32) is N. Thus, the resulting angular steps must satisfy the following inequalities:

$$\Delta\phi \leq \frac{2\pi}{2N+1} \tag{C.3}$$

$$\Delta\theta \leq \frac{2\pi}{2N+1}. \tag{C.4}$$

In its discrete form of (C.1), the evaluation of the integral becomes straightforward by means of a DFT, i.e.

$$c_m(r_a, \theta_l) = \text{DFT}\left[\psi(r_a, \phi_i, \theta_l)\right], \tag{C.5}$$

where $i = 0, 1, \ldots, 2N$ and $l = 0, 1, \ldots, 2N$ denote the indexes associated with the angles ϕ and θ, respectively. In practice the measured angular range in ϕ will be smaller than 2π. Consequently, the backscattered fields outside this window will have to be padded with zeroes prior to the computation of the DFT.

The discrete evaluation of the integral in θ in (C.2) is a bit trickier. Now the integral cannot be simply evaluated by means of a single DFT. Alternatively, the Fourier expansion property of the normalized associate Legendre functions is used to evaluate the discrete integral using DFT codes [91]. Thus, the normalized associate Legendre functions can be expanded into a Fourier series as follows

$$\overline{P}_n^m(\cos\theta) = j^m \sum_{p=-n}^{n} d_{m,p}\, e^{jp\theta} = j^{-m} \sum_{p=-n}^{n} d_{m,p}\, e^{-jp\theta}. \qquad (C.6)$$

The coefficients $d_{m,p}$ vanish for $(p+n)$ odd, and they satisfy the recurrence relation:

$$(n+p+2)(n-p-1)\, d_{m,p+2} - 2(n^2-p^2+n-2m^2)\, d_{m,p} + \dots$$
$$(n+p-1)(n-p+2)\, d_{m,p-2} = 0, \quad (C.7)$$

with the initial values being:

$$d_{m,n} = \frac{1}{2^{2n}}\frac{(2n)!}{n!}\sqrt{\frac{2n+1}{2}}\sqrt{\frac{1}{(n+m)!(n-m)!}} \qquad (C.8)$$

$$d_{m,n-2} = \frac{n-2m^2}{2n-1}\, d_{m,n}. \qquad (C.9)$$

For $m = 0$, the recurrence in (C.7) takes the form

$$(n+p)(n-p+1)\, d_{0,p} - (n+p-1)(n-p+2)\, d_{0,p-2} = 0. \qquad (C.10)$$

At this point, there is an important aspect to consider: the domain of the angle θ must be within the range $(0,\pi)$, as opposed to the range $(0,2\pi)$ in ϕ. The dependence on θ of the backscattered fields is extended to the range $(0,2\pi)$ as follows. Noting that $(m/|m|)^m \overline{P}_n^m(\cos\theta)$ is periodic in θ with period 2π, and that its parity about $\theta = \pi$ is the same as m (odd if m is odd, and even if m is even), the θ dependence is extended in the following way

$$\hat{c}_m(r_a,\theta) = \begin{cases} c_m(r_a,\theta), & 0 \le \theta \le \pi \\ (-1)^m\, c_m(r_a, 2\pi-\theta), & \pi < \theta < 2\pi \end{cases} \qquad (C.11)$$

The coefficients $\hat{c}_m(r_a,\theta)$ are then expanded into a finite Fourier series as follows

$$\hat{c}_m(r_a,\theta) = \sum_{l=-N}^{N} b_{m,l}\, e^{jl\theta}. \qquad (C.12)$$

By substituting (C.6) and (C.12) in (C.2), the coefficients $c_{m,n}(r_a)$ take the form:

$$c_{m,n}(r_a) = \int_{\theta=0}^{\pi} \sum_{l=-N}^{N} b_{m,l}\, e^{jl\theta}\, j^{-m} \sum_{p=-n}^{n} d_{m,p}\, e^{-jp\theta} \sin\theta\, d\theta \qquad (C.13)$$

$$= j^{-m} \sum_{l=-N}^{N} b_{m,l} \sum_{p=-n}^{n} d_{m,p} \int_{\theta=0}^{\pi} e^{j(l-p)\theta} \sin\theta\, d\theta. \qquad (C.14)$$

The integral in (C.14) can be denoted as $G(l-p)$, and has an analytical solution

$$G(l-p) = \begin{cases} \pm j\frac{\pi}{2}, & (l-p) = \pm 1 \\ 0, & |l-p| = 3, 5, 7, \ldots \\ \dfrac{2}{1-(l-p)^2}, & |l-p| = 0, 2, 4, \ldots \end{cases} \qquad (C.15)$$

The resulting expression for the coefficients $c_{m,n}(r_a)$ becomes

$$c_{m,n}(r_a) = j^{-m} \sum_{l=-N}^{N} b_{m,l} \sum_{p=-n}^{n} d_{m,p}\, G(l-p), \qquad (C.16)$$

where the only unknowns on the right-hand side are now the Fourier coefficients $b_{m,l}$, which can be simply evaluated through a DFT.

A further analysis of the elements in (C.16) yields an additional simplification. From their definition, it can be observed that

$$b_{m,l} = (-1)^m b_{m,-l} \qquad (C.17)$$
$$d_{m,p} = (-1)^m d_{m,-p}, \qquad (C.18)$$

and therefore,

$$b_{m,l}\, d_{m,p} = b_{m,-l}\, d_{m,-p}. \qquad (C.19)$$

Since

$$G(l-p) = -G(p-l), \quad (l-p) = \pm 1, \qquad (C.20)$$

the terms with $(l-p) = \pm 1$ cancel out, and the final expression for the coefficients $c_{m,n}(r_a)$ becomes

$$c_{m,n}(r_a) = j^{-m} \sum_{p=-n}^{n} d_{m,p} \sum_{l=-N}^{N} \prod(l-p) b_{m,l}, \qquad (C.21)$$

where

$$\prod(l-p) = \begin{cases} 0, & (l-p) \text{ odd} \\ \dfrac{2}{1-(l-p)^2}, & (l-p) \text{ even} \end{cases} \qquad (C.22)$$
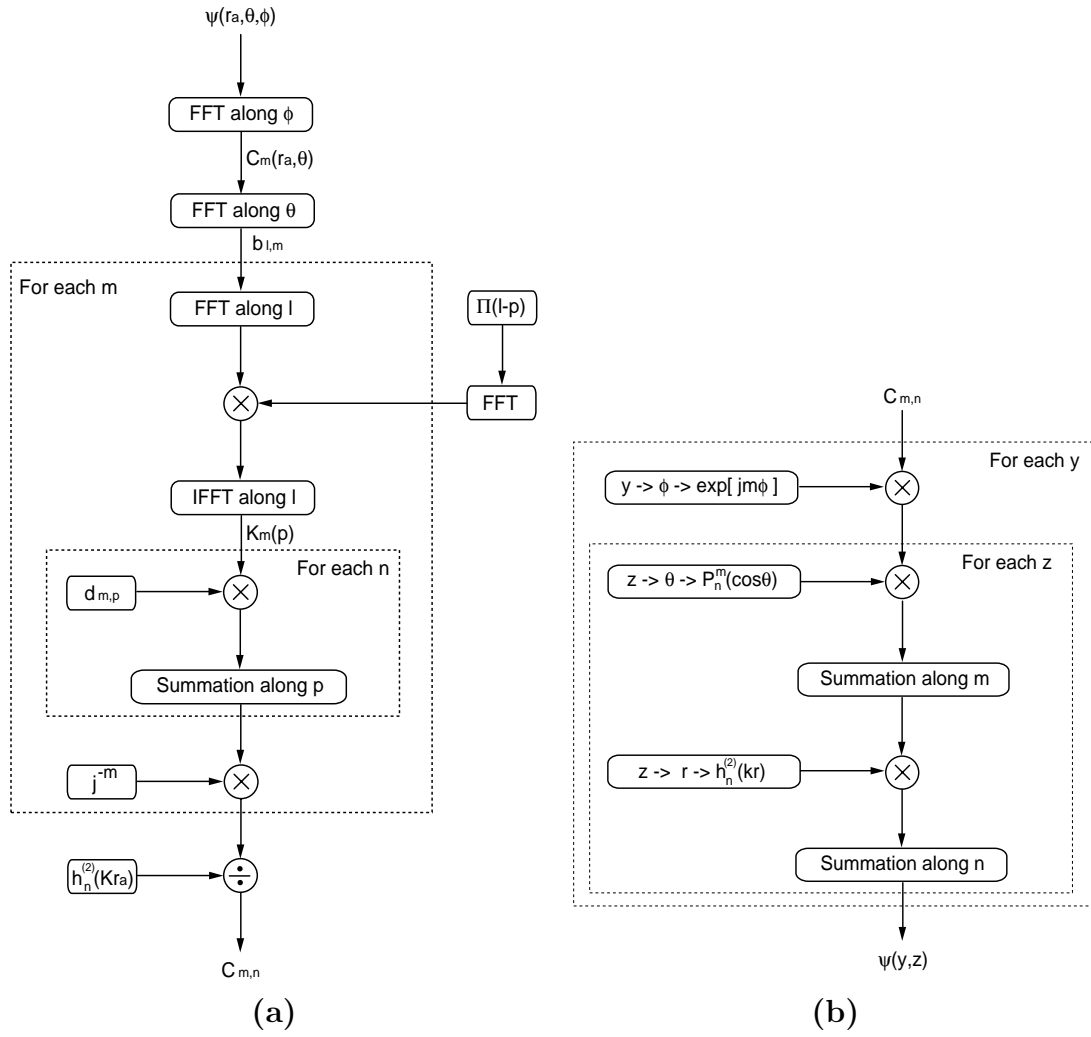
Figure C.1.   (a) Flow chart of the computation of the coefficients from the backscatter data
measured on a spherical aperture; (b) Flow chart of the computation of the backscattered
fields from the coefficients $c_{m,n}$.

and $\prod(l-p) = \prod(p-l)$.

The l-summation in (C.21) resembles, for each value of p, a convolution between two
sequences. Hence, it can be evaluated efficiently by means of DFTs. If the result is named
$K_m(p)$, the final expression of the coefficients is

$$c_{m,n}(r_a) = j^{-m} \sum_{p=-n}^{n} d_{m,p} \, K_m(p). \tag{C.23}$$

The procedure to evaluate the amplitudes of the spherical harmonics is summarized in
the flow chart in Figure C.1 (a). The rectangles with dashed lines indicate a loop. Note
that the coefficients are explicitly available at the end of this process. This was not the case

in the translation from the cylindrical to the planar apertures because they were reused for each n immediately after their calculation. The subsequent evaluation of backscatter fields once the spherical harmonics amplitudes are known is illustrated in Figure C.1 (b).

Solution of the Fourier integral in Eq. (4.5) using the MSP

Solution of the Fourier integral in (4.5) using the MSP [95] takes the form

$$\mathcal{F}(\rho, k_\phi, z; f, \theta) \simeq \frac{\sqrt{j\,2\pi}}{R_a^2} \left\{ \frac{R^2(\phi_-)}{\sqrt{p''(\phi_-)}} \, \exp\left[j\,p(\phi_-)\right] + \frac{R^2(\phi_+)}{\sqrt{p''(\phi_+)}} \, \exp\left[j\,p(\phi_+)\right] \right\} \quad \text{(D.1)}$$

where ϕ_- and ϕ_- are two stationary phase points determined by the equations,

$$p'(\phi_-) = \left.\frac{\partial p(\phi)}{\partial \phi}\right|_{\phi_-} = A\,\frac{C\sin\phi_-}{2\sqrt{B - C\cos\phi_-}} - k_\phi = 0 \quad \text{(D.2)}$$

$$p'(\phi_+) = \left.\frac{\partial p(\phi)}{\partial \phi}\right|_{\phi_+} = A\,\frac{C\sin\phi_+}{2\sqrt{B - C\cos\phi_+}} - k_\phi = 0 \quad \text{(D.3)}$$

which, after some algebraical manipulations, result in

$$\phi_\pm = \arccos\left[\frac{2\,\alpha^2 \pm \sqrt{\beta^2 - 4\,\alpha^2(1 - \alpha^2)}}{\beta}\right] \quad \text{(D.4)}$$

$$p(\phi_\pm) = \gamma\left[\sqrt{1 - [2\,\alpha^2 \pm \sqrt{\beta^2 - 4\,\alpha^2(1 - \alpha^2)}]} - \alpha\,\phi_\pm\right] - 2kR_a \quad \text{(D.5)}$$

$$p''(\phi_\pm) = \pm\gamma\,\frac{\sqrt{\beta^2 - 4\,\alpha^2(1 - \alpha^2)}}{2\sqrt{1 - [2\,\alpha^2 \pm \sqrt{\beta^2 - 4\,\alpha^2(1 - \alpha^2)}]}} \quad \text{(D.6)}$$

$$R(\phi_\pm) = \frac{\gamma}{A}\,\sqrt{1 - [2\,\alpha^2 \pm \sqrt{\beta^2 - 4\,\alpha^2(1 - \alpha^2)}]} \quad \text{(D.7)}$$

with

$$\alpha = \frac{k_\phi}{\gamma}, \qquad \beta = \frac{C}{B}, \qquad \text{and} \qquad \gamma = A\sqrt{B} \tag{D.8}$$

The approximation in (D.1) is satisfactory if the function $p''(\cdot)$ does not vanish at the stationary phase points. From (D.2) and (D.3), it can be shown that the two stationary phase points converge to a single point as k_ϕ increases, which is given by

$$\phi_o = \arccos\left[\frac{1 - \sqrt{1 - \beta^2}}{\beta}\right] \tag{D.9}$$

As in any asymptotic expansion, it is difficult to give precise conditions for the validity of (D.1). However, the following gives some indication of the range of k_ϕ where the error is small compared to $\mathcal{F}(\cdot)$,

$$0 \leq k_\phi \leq \hat{k}_\phi = |p'''(\phi_o)| - \left(\frac{|p'''(\phi_o)|}{2}\right)^{(1/3)} \tag{D.10}$$

If $k_\phi > \hat{k}_\phi$, then the major contribution to the integral (4.5) comes from a small neighborhood near the point $\phi = \phi_o$. In this neighborhood, $p''(\phi)$ vanishes and the following higher order series expansion

$$p(\phi) \simeq p(\phi_o) + p'(\phi_o)\,(\phi - \phi_o) + p'''(\phi_o)\,\frac{(\phi - \phi_o)^3}{3!} \tag{D.11}$$

must be used in the asymptotic evaluation of (4.5), leading to

$$\mathcal{F}(\rho, k_\phi, z; f, \theta) \simeq 2\pi \left(\frac{R(\phi_o)}{R_a}\right)^2 \exp\left[jp(\phi_o)\right] \left(\frac{2}{|p'''(\phi_o)|}\right)^{(1/3)}$$
$$\times \; Ai\left(-\left[\frac{2}{|p'''(\phi_o)|}\right]^{(1/3)} p'(\phi_o)\right) \tag{D.12}$$

wherein $Ai(\cdot)$ denotes the Airy function [92], and

$$p(\phi_o) \;=\; \gamma\left[\left(1 - \beta^2\right)^{(1/4)} - \alpha\,\phi_o\right] - 2kR_a \tag{D.13}$$

$$p'(\phi_o) \;=\; \gamma\left[-\alpha + \sqrt{\frac{1 - \sqrt{1 - \beta^2}}{2}}\right] \tag{D.14}$$

$$p'''(\phi_o) \;=\; -\gamma\sqrt{\frac{1 - \sqrt{1 - \beta^2}}{2}} \tag{D.15}$$

$$\phi_o \;=\; \arccos\left[\frac{1 - \sqrt{1 - \beta^2}}{\beta}\right] \tag{D.16}$$

$$R(\phi_o) \;=\; \frac{\gamma}{A}\,(1 - \beta^2)^{(1/4)} \tag{D.17}$$

provided that

$$\hat{k}_\phi < k_\phi \leq \frac{N_\phi}{2} \tag{D.18}$$

List of Publications

1. J. Fortuny and A. J. Sieber, "Fast algorithm for a near field synthetic aperture radar processor," *IEEE Trans. on Antennas and Propagation*, vol. 42, pp. 1458–1460, October 1994.

2. P. Nardone, J. Fortuny, and A. J. Sieber, "Initial conditions, reflection and transmission coefficients revisited," *Journal of Electromagnetic Waves and Applications*, vol. 10, pp. 1527–1542, November 1996.

3. G. Nesti, J. Fortuny, and A. J. Sieber, "Comparison of backscattered signal statistics as derived from indoor scatterometric and SAR experiments," *IEEE Trans. on Geoscience and Remote Sensing*, vol. 34, pp. 1074–1083, September 1996.

4. J. Fortuny, "An efficient three-dimensional near field ISAR algorithm using the method of stationary phase," *IEEE Trans. on Aerospace and Electronic Systems*, vol. 34, pp. 1261–1270, October 1998.

5. J. Fortuny and A. J. Sieber, "Three-dimensional synthetic aperture radar imaging of a Fir tree: First results," *IEEE Trans. on Geoscience and Remote Sensing*, vol. 37, pp. 1006–1014, March 1999.

6. J. M. López-Sánchez, H. Esteban-González, M. Baquero-Escudero, and J. Fortuny, "An electromagnetic scattering model for multiple tree trunks above a tilted rough ground plane," *IEEE Trans. on Geoscience and Remote Sensing*, vol. 37, pp. 659–667, March 1999.

7. T. Kottos, U. Smilansky, J. Fortuny, and G. Nesti, "Chaotic scattering of microwaves," *Radio Science*, vol. 34, pp. 747–758, July 1999.

8. S. R. Cloude, J. Fortuny, J. M. López-Sánchez, and A. J. Sieber, "Wideband polarimetric radar inversion studies for vegetation layers," *IEEE Trans. on Geoscience and Remote Sensing*, vol. 37, pp. 2430–2441, September 1999.

9. J. M. Lopez, J. Fortuny, S. R. Cloude, and A. J. Sieber, "Indoor polarimetric radar measurements on vegetation samples at L, C, S, and X-Band," *Journal of Electromagnetic Waves and Applications*, vol. 14, pp. 205–232, February 2000.

10. L. Sagués, J. M. López-Sánchez, J. Fortuny, X. Fàbregas, A. Broquetas, and A. J. Sieber, "Indoor experiments on polarimetric SAR interferometry," *IEEE Trans. on Geoscience and Remote Sensing*, vol. 38, pp. 670–684, March 2000.

11. J. M. López-Sánchez and J. Fortuny, "3-D Radar imaging using range migration techniques," *IEEE Trans. on Antennas and Propagation*, vol. 48, pp. 728–737, May 2000.

12. R. L. Eigel, P. J. Collins, A. J. Terzuoli, Jr., G. Nesti, and J. Fortuny, "Bistatic scattering characterization of complex objects," *IEEE Trans. on Geoscience and Remote Sensing*, vol. 38, pp. 2078–2092, September 2000.

13. J. Fortuny and J. M. López-Sánchez, "Extension of the 3-D range migration algorithm to cylindrical and spherical scanning geometries," *IEEE Trans. on Antennas and Propagation*, vol. 49, pp. 1434–1444, October 2001.

14. J. Fortuny, "A novel three-dimensional near-field subsurface radar imaging technique," *IEEE Trans. on Geoscience and Remote Sensing*. Submitted for publication in January 2001.

Bibliography

[1] W. M. Brown, "Synthetic aperture radar," *IEEE Trans. on Aerospace and Electronic Systems*, vol. 3, pp. 217–229, March 1967.

[2] C. A. Wiley, "Pulsed Doppler radar methods and apparatus." US Patent 3,196,436 filed in 1954.

[3] J. L. Walker, "Range-Doppler imaging of rotating objects," *IEEE Trans. on Aerospace and Electronic Systems*, vol. 16, pp. 23–52, January 1980.

[4] N. N. Bojarski, "K-space formulation of the electromagnetic scattering problems," Tech. Rep. AFAL-TR-71-75, US Air Force Avionic Lab, 1971.

[5] D. L. Mensa, G. Heidbreder, and G. Wade, "Aperture synthesis by object rotation in coherent imaging," *IEEE Trans. on Nuclear Science*, vol. 27, pp. 989–998, April 1980.

[6] D. R. Wehner, M. J. Prickett, R. G. Rock, and C. C. Chen, "Stepped frequency radar target imagery, theoretical concept and preliminary results," Tech. Rep. 490, Naval Ocean Systems Center, San Diego (CA), November 1979.

[7] C. C. Chen and H. C. Andrews, "Multifrequency imaging of radar turntable data," *IEEE Trans. on Aerospace and Electronic Systems*, vol. 16, pp. 15–22, January 1980.

[8] D. A. Ausherman, A. Kozma, J. L. Walker, H. M. Jones, and E. C. Poggio, "Developments in radar imaging," *IEEE Trans. on Aerospace and Electronic Systems*, vol. 20, pp. 363–400, October 1984.

[9] N. H. Farhat, C. L. Werner, and T. H. Chu, "Prospects for three-dimensional projective and tomographic imaging radar networks," *Radio Science*, vol. 19, pp. 1347–1355, September 1984.

[10] C. L. Werner, *Three Dimensional Imaging of Coherent and Incoherent Sources Utilizing Wavevector Diversity*. PhD thesis, University of Pennsylvania, Pennsylvania (PA), 1985.

[11] D. L. Mensa, S. Halevy, and G. Wade, "Coherent Doppler tomography for microwave imaging," *Proceedings of the IEEE*, vol. 71, pp. 254–261, February 1983.

[12] D. L. Mensa, "Wideband radar cross section diagnostic measurements," *IEEE Trans. on Instrumentation and Measurement*, vol. 33, pp. 206–214, September 1984.

[13] D. C. Munson, Jr. and R. L. Visentin, "A tomographic formulation of spotlight-mode synthetic aperture radar," *Proceedings of the IEEE*, vol. 71, pp. 917–925, August 1983.

[14] C. V. Jakowatz and P. A. Thompson, "A new look at spotlight mode synthetic aperture radar as tomography: Imaging 3-D targets," *IEEE Trans. on Image Processing*, vol. 4, pp. 699–703, May 1995.

[15] C. V. Jakowatz, *Spotlight-Mode Synthetic Aperture Radar: A Signal Processing Approach*. Dordrecht, The Netherlands: Kluwer Academic Publishers, 1996.

[16] W. Lawton, "A new polar Fourier transform for computer-aided tomography and spotlight synthetic aperture radar," *IEEE Trans. on Acoustics, Speech, and Signal Processing*, vol. 36, pp. 931–933, June 1988.

[17] D. C. Munson, Jr. and R. L. Visentin, "A signal processing view of strip-mapping synthetic aperture radar," *IEEE Trans. on Acoustics, Speech, and Signal Processing*, vol. 37, pp. 2131–2147, December 1989.

[18] F. Rocca, "Synthetic aperture radar: A new application for wave equation techniques," Tech. Rep. SEP-56, Stanford University, 1987.

[19] C. Cafforio, C. Prati, and E. Rocca, "SAR data focusing using seismic migration techniques," *IEEE Trans. on Aerospace and Electronic Systems*, vol. 27, pp. 194–207, April 1991.

[20] C. Prati, A. Monti Guarnieri, and F. Rocca, "Spot mode SAR focusing with the $\omega - k$ technique," in *Proc. of the IEEE International Geoscience and Remote Sensing Symposium (IGARSS)*, Helsinki, IEEE, pp. 631–634, 1991.

[21] R. Stolt, "Migration by Fourier transform techniques," *Geophysics*, no. 43, pp. 49–76, 1978.

[22] R. Bamler, "A comparison of range-Doppler and wavenumber domain SAR focusing algorithms," *IEEE Trans. on Geoscience and Remote Sensing*, vol. 30, pp. 706–713, July 1992.

[23] H. Choi and D. C. Munson, Jr., "On the optimality and exactness of the wavenumber-domain SAR data processing," in *Proc. of the IEEE International Conference on Image Processing*, Austin (TX), IEEE, pp. 456–460, November 1994.

[24] J. A. Lee and D. C. Munson, Jr., "Effect of a non-planar wavefront in spotlight-mode synthetic aperture radar," in *Proc. of the IEEE International Conference on Image Processing*, Austin (TX), IEEE, pp. 481–485, November 1994.

[25] A. Reigber and A. Moreira, "First demonstration of airborne SAR tomography using multibaseline L-band data," *IEEE Trans. on Geoscience and Remote Sensing*, vol. 38, pp. 2142–2152, September 2000.

[26] S. E. Assad, I. Lakkis, and J. Saillard, "Holographic SAR image formation by coherent summation of impulse response derivatives," *IEEE Trans. on Antennas and Propagation*, vol. 41, pp. 620–624, May 1993.

[27] C. U. S. Larsson, R. Erickson, and O. Lundén, "3-D processing and imaging of near field ISAR data in an arbitrary measurement geometry," in *Proc. of the AMTA Seventeenth Meeting and Symposium*, Williamsburg (VA), Antenna Measurements and Techniques Association, pp. 106–110, November 1995.

[28] J. Bredow, K. Xie, R. Porco, and M. Shah, "An experimental study on the use of multistatic imaging for investigating wave-object interaction," *Journal of Electromagnetic Waves and Applications*, vol. 7, pp. 811–831, June 1993.

[29] L. Carin, R. Kapoor, and C. E. Baum, "Polarimetric SAR imaging of buried landmines," *IEEE Trans. on Geoscience and Remote Sensing*, vol. 36, pp. 1985–1988, November 1998.

[30] L. Carin, N. Geng, M. McClure, J. Sichina, and L. Nguyen, "Ultra-wideband synthetic-aperture radar for mine-field detection," *IEEE Antennas and Propagation Magazine*, vol. 41, pp. 18–33, January 1999.

[31] N. C. Currie, *Radar Reflectivity Measurement: Techniques and Applications.* Norwood (MA), USA: Artech House, 1989.

[32] H. Kim, J. T. Johnson, and B. A. Baertlein, "High resolution Ka-band images of a small tree: Measurements and models," *IEEE Trans. on Geoscience and Remote Sensing*, vol. 38, pp. 899–910, March 2000.

[33] R. L. Harris, B. E. Freburger, M. E. Lewis, and C. F. Zappala, "Three-dimensional radar cross section imaging," in *Proc. of the AMTA Sixteenth Meeting and Symposium*, Long Beach (CA), Antenna Measurements and Techniques Association, pp. 443–448, October 1994.

[34] B. Scheers, *Ultra-Wideband Ground Penetrating Radar, with Applicattion to the Detection of Anti Personnel Landmines*. PhD thesis, Royal Military Academy, Brussels, Belgium, March 2001.

[35] A. Broquetas, L. Jofre, and A. Cardama, "A near field spherical wave inverse synthetic aperture radar technique," in *Proc. of the IEEE Antennas and Propagation Society International Symposium*, Chicago (IL), IEEE, vol. 2, pp. 114–117, July 1992.

[36] S. C. M. Brown and J. C. Bennett, "High-resolution microwave polarimetric imaging of small trees," *IEEE Trans. on Geoscience and Remote Sensing*, vol. 37, pp. 48–53, January 1999.

[37] C. Fischer, J. Fortuny, and W. Wiesbeck, "3-D imaging for near-range ground penetrating radar based on $w - k$ migration," in *Proc. of the 3rd European Conference on Synthetic Aperture Radar (EUSAR)*, Munich, VGE, pp. 841–844, May 2000.

[38] C. Fischer and W. Wiesbeck, "Laboratory verification for a forward-looking multi-receiver mine-detection GPR," in *Proc. of the IEEE International Geoscience and Remote Sensing Symposium (IGARSS)*, Honolulu (HI), IEEE, vol. IV, pp. 1643–1645, July 2000.

[39] D. G. Falconer, "Extrapolation of near-field RCS measurements to the far zone," *IEEE Trans. on Antennas and Propagation*, vol. 36, pp. 822–829, June 1988.

[40] J. W. Odendaal and J. Joubert, "Radar cross section measurements using near-field radar imaging," *IEEE Trans. on Antennas and Propagation*, vol. 45, pp. 948–954, December 1996.

[41] A. Broquetas, J. Palau, L. Jofre, and A. Cardama, "Spherical wave near-field imaging and radar cross-section measurement," *IEEE Trans. on Antennas and Propagation*, vol. 46, pp. 730–735, May 1998.

[42] A. Boag, Y. Bresler, and E. Michielssen, "A multilevel domain decomposition algorithm for fast $O(N^2 \log N)$ reprojection of tomographic images," *IEEE Trans. on Image Processing*, vol. 9, pp. 1573–1582, September 2000.

[43] A. Boag, "A fast multilevel domain decomposition algorithm for radar imaging," *IEEE Trans. on Antennas and Propagation*, vol. 49, pp. 666–671, April 2001.

[44] K. J. Langenberg, "Introduction to the special issue on inverse problems," *Wave Motion*, no. 11, pp. 99–112, 1989.

[45] K. J. Langenberg, P. Fellinger, R. Marklein, P. Zanger, K. Mayer, and T. Kreutter, *Evaluation of Materials and Structures by Quantitative Ultrasonics*, ch. 5, pp. 317–398. Vienna, Austria: Springer-Verlag, Ed. J. D. Achenbach, 1993.

[46] K. J. Langenberg, M. Brandfaß, P. Fellinger, T. Gurke, and T. Kreutter, *Radar Target Imaging*, ch. 3, pp. 113–151. Berlin, Germany: Springer-Verlag, Eds. H. Überall and W. M. Boerner, 1994.

[47] G. S. Smith and L. E. Petersson, "On the use of evanescent electromagnetic waves in the identification and of objects buried in lossy soil," *IEEE Trans. on Antennas and Propagation*, vol. 48, pp. 1295–1300, September 2000.

[48] W. G. Carrara, R. S. Goodman, and R. M. Majewski, *Spotlight Synthetic Aperture Radar: Signal Processing Algorithms*. Norwood (MA), USA: Artech House, 1995.

[49] D. L. Mensa, *High Resolution Radar Cross Section Imaging*. Norwood (MA), USA: Artech House, 2nd ed., 1991.

[50] C. Elachi, *Introduction to the Physics and Techniques of Remote Sensing*. New York, USA: John Wiley and Sons, 1987.

[51] A. Golden, S. C. Wei, K. K. Ellis, and S. Tummala, "Migration processing of spotlight SAR data," in *SPIE, Algorithms for Synthetic Aperture Radar Imagery I*, Orlando (FL), SPIE, vol. 2230, pp. 25–35, 1994.

[52] C. Prati and F. Rocca, "Focusing SAR data with time-varying Doppler centroid," *IEEE Trans. on Geoscience and Remote Sensing*, vol. 30, pp. 550–559, May 1992.

[53] J. Fortuny, E. Ohlmer, A. J. Sieber, P. Pasquali, C. Prati, and F. Rocca, "Validating SAR interferometry applications by using EMSL," in *Proc. of the IEEE International Geoscience and Remote Sensing Symposium (IGARSS)*, Pasadena, IEEE, vol. 2, pp. 736–738, 1994.

[54] V. K. Madisetti and D. G. Messerschmitt, "Seismic migration algorithms on parallel computers," *IEEE Trans. on Signal Processing*, vol. 39, pp. 1642–1654, July 1991.

[55] C. Yerkes and E. Webster, "Implementation of $w-k$ synthetic aperture radar imaging algorithm on a massively parallel supercomputer," in *SPIE, Algorithms for Synthetic Aperture Radar Imagery I*, Orlando (FL), SPIE, vol. 2230, pp. 171–178, 1994.

[56] R. K. Raney, H. Runge, R. Bamler, I. G. Cumming, and F. H. Wong, "Precision SAR processing using chirp scaling," *IEEE Trans. on Geoscience and Remote Sensing*, vol. 32, pp. 786–799, July 1994.

[57] J. Fortuny and A. J. Sieber, "Fast algorithm for a near field synthetic aperture radar processor," *IEEE Trans. on Antennas and Propagation*, vol. 42, pp. 1458–1460, October 1994.

[58] J. Fortuny, "An efficient three-dimensional near field ISAR algorithm using the method of stationary phase," *IEEE Trans. on Aerospace and Electronic Systems*, vol. 34, pp. 1261–1270, October 1998.

[59] J. Fortuny, "A novel three-dimensional near-field subsurface radar imaging technique," *IEEE Trans. on Geoscience and Remote Sensing*. Submitted for publication in January 2001.

[60] A. J. Sieber, "The European Microwave Signature Laboratory," *EARSel Advances in Remote Sensing*, vol. 2, pp. 195–204, January 1993.

[61] W. Tabbara, B. Duchene, C. Pichot, D. Lesselier, L. Chommeloux, and N. Joachimowicz, "Diffraction tomography: Contribution to the analysis of some applications in microwaves and ultrasonics," *Inverse Problems*, vol. 4, pp. 305–331, 1988.

[62] A. J. Devaney, "Geophysical diffraction tomography," *IEEE Trans. on Geoscience and Remote Sensing*, vol. 22, no. 1, pp. 3–13, 1984.

[63] N. Joachimowicz, C. Pichot, and J. P. Hugonin, "Inverse scattering: An iterative numerical method for electromagnetic imaging," *IEEE Trans. on Antennas and Propagation*, vol. 39, pp. 1742–1751, 1991.

[64] C. Fischer, J. Fortuny, and W. Wiesbeck, "Fundamental limitations for the resolution of SAR sensors," in *Proc. of the 3rd European Conference on Synthetic Aperture Radar (EUSAR)*, Munich, VGE, pp. 467–470, May 2000.

[65] J. M. López-Sánchez and J. Fortuny, "3-D Radar imaging using range migration techniques," *IEEE Trans. on Antennas and Propagation*, vol. 48, pp. 728–737, May 2000.

[66] J. Fortuny and J. M. López-Sánchez, "Extension of the 3-D range migration algorithm to cylindrical and spherical scanning geometries," *IEEE Trans. on Antennas and Propagation*, vol. 49, pp. 1434–1444, October 2001.

[67] J. Fortuny and A. J. Sieber, "Three-dimensional synthetic aperture radar imaging of a Fir tree: First results," *IEEE Trans. on Geoscience and Remote Sensing*, vol. 37, pp. 1006–1014, March 1999.

[68] R. N. Bracewell, *The Fourier Transform and its Applications*. New York, USA: McGraw Hill, 1986.

[69] A. V. Oppenheim and R. W. Schafer, *Discrete-Time Signal Processing*. Englewood Cliffs (NJ), USA: Prentice Hall, 1989.

[70] W. Wiesbeck and D. Kähny, "Single reference, three target calibration and error correction for monostatic, polarimetric free space measurements," *Proceedings of the IEEE*, vol. 79, pp. 1551–1558, October 1991.

[71] C. A. Balanis, *Antenna Theory*. New York, USA: John Wiley and Sons, 1982.

[72] J. P. Fitch, *Synthetic Aperture Radar*. Berlin, Germany: Springer-Verlag, 1987.

[73] A. Papoulis, *Systems and Transforms with Applications in Optics*. New York, USA: McGraw-Hill, 1968.

[74] K. Mayer, R. Marklein, K. J. Langenberg, and T. Kreutter, "Three-dimensional imaging system based on Fourier synthetic aperture focusing technique," *Ultrasonics*, vol. 28, pp. 241–255, July 1990.

[75] L. J. Busse, "Three-dimensional imaging using a frequency-domain synthetic aperture focusing technique," *IEEE Trans. on Ultrasonics, Ferroelectrics and Frequency Control*, vol. 39, pp. 174–179, March 1992.

[76] A. Yamani, "Three-dimensional imaging using a new synthetic aperture focusing technique," *IEEE Trans. on Ultrasonics, Ferroelectrics and Frequency Control*, vol. 44, pp. 943–947, July 1997.

[77] A. Yamani, "A novel pulse-echo technique for medical three-dimensional imaging," *IEEE Trans. on Medical Imaging*, vol. 16, pp. 958–942, December 1997.

[78] M. Fink, "Time reversal of ultrasonic fields - Part I: Basic principles," *IEEE Trans. on Ultrasonics, Ferroelectrics and Frequency Control*, vol. 39, pp. 555–566, September 1992.

[79] F. Wu, J. L. Thomas, and M. Fink, "Time reversal of ultrasonic fields - Part II: Experimental results," *IEEE Trans. on Ultrasonics, Ferroelectrics and Frequency Control*, vol. 39, pp. 567–578, September 1992.

[80] D. Cassereau and M. Fink, "Time reversal of ultrasonic fields - Part III: Theory of the closed time-reversal cavity," *IEEE Trans. on Ultrasonics, Ferroelectrics and Frequency Control*, vol. 39, pp. 579–592, September 1992.

[81] O. M. Bucci and C. Gennarelli, "Use of sampling expansions in near-field-far-field transformations: The cylindrical case," *IEEE Trans. on Antennas and Propagation*, vol. 36, pp. 830–835, June 1988.

[82] O. M. Bucci, C. Gennarelli, and C. Savarese, "Fast and accurate near-field-far-field transformation by sampling interpolation of plane-polar measurements," *IEEE Trans. on Antennas and Propagation*, vol. 39, pp. 48–55, January 1991.

[83] O. M. Bucci, G. D'Elia, and M. D. Migliore, "Near-field far-field transformation in time domain from optimal plane-polar samples," *IEEE Trans. on Antennas and Propagation*, vol. 46, pp. 1084–1088, July 1998.

[84] A. Taaghol and T. K. Sarkar, "Near-field to near/far-field transformation for arbitrary near-field geometry, utilizing an equivalent magnetic current," *IEEE Trans. on Electromagnetic Compatibility*, vol. 38, pp. 536–542, August 1996.

[85] T. K. Sarkar and A. Taaghol, "Near-field to near/far-field transformation for arbitrary near-field geometry utilizing an equivalent electric current and MoM," *IEEE Trans. on Antennas and Propagation*, vol. 47, pp. 566–573, March 1999.

[86] A. C. Kak, *Principles of Computerized Tomographic Imaging.* Piscataway (NJ), USA: IEEE Press, 1987.

[87] F. J. Harris, "On the use of windows for harmonic analysis with the discrete Fourier transform," *Proceedings of the IEEE*, vol. 66, pp. 172–204, January 1978.

[88] G. T. Ruck, D. E. Barrick, C. K. Kirchbaum, and W. D. Stuart, *Radar Cross Section Handbook*, vol. I. Plenum Press, 1970.

[89] R. F. Harrington, *Time-Harmonic Electromagnetic Fields.* New York, USA: McGraw-Hill, 1961.

[90] J. M. López-Sánchez, *Analysis and Estimation of Biophysical Parameters of Vegetation by Radar Polarimetry.* PhD thesis, Universidad Politécnica de Valencia, Valencia, Spain, 1999. JRC SPI.0071.

[91] J. E. Hansen, *Spherical Near-Field Antenna Measurements.* London, UK: Peter Peregrinus Ltd., 1988.

[92] M. Abramowitz and I. A. Stegun, *Handbook of Mathematical Functions.* New York, USA: Dover Publications Inc., 1970.

[93] W. H. Press, S. A. Teukolsky, W. T. Vetterling, and B. P. Flannery, *Numerical Recipes in C.* Cambridge, UK: Cambridge University Press, 1992.

[94] J. C. Curlander and R. N. McDonough, *Synthetic Aperture Radar: Systems and Signal Processing.* New York, USA: John Wiley and Sons, 1992.

[95] A. Papoulis, *Signal Analysis.* New York, USA: McGraw-Hill, 1977.

[96] J. D. O'Sullivan, "A fast sinc function gridding algorithm for Fourier inversion in computer tomography," *IEEE Trans. on Medical Imaging*, vol. 4, pp. 200–207, December 1985.

[97] R. N. Bracewell, *Two-Dimensional Image Processing.* Englewood Cliffs (NJ): Prentice Hall International, 1995.

[98] P. M. Prenter, *Splines and Variational Methods.* New York, USA: Wiley-Interscience, 1975. ch. 5.

[99] G. Graf and B. Röde, "Radar scattering from a solitary Fir tree," in *Proc. of the IEEE International Geoscience and Remote Sensing Symposium (IGARSS)*, Munich, IEEE, 1982.

[100] A. J. Sieber, "Forest signatures in imaging and non-imaging microwave scatterometer data," *ESA Journal*, vol. 9, pp. 431–448, April 1985.

[101] H. Hirosawa, Y. Matsuzaka, M. Daito, and H. Nakamura, "Measurement of backscatter from conifers in the C and X bands," *International Journal of Remote Sensing*, vol. 11, no. 8, pp. 1687–1694, 1987.

[102] H. Hirosawa, Y. Matsuzaka, and O. Kobayashi, "Measurements of microwave backscatter from cypress with and without leaves," *IEEE Trans. on Geoscience and Remote Sensing*, vol. 27, pp. 698–701, November 1989.

[103] M. A. Karam and A. K. Fung, "Leaf-shape effects in electromagnetic wave scattering from vegetation," *IEEE Trans. on Geoscience and Remote Sensing*, vol. 27, pp. 687–697, November 1989.

[104] A. Lopes and E. Mougin, "Microwave coherent propagation in cylindrical shaped forest components: Interpretation of attenuation observations," *IEEE Trans. on Geoscience and Remote Sensing*, vol. 28, pp. 315–324, May 1990.

[105] S. Riegger and W. Wiesbeck, "Coherent polarimetric RCS mesurements on trees," in *Proc. of the IEEE International Geoscience and Remote Sensing Symposium (IGARSS)*, Zurich, IEEE, vol. SP-254, pp. 883–887, 1986.

[106] S. R. Cloude and E. Pottier, "An entropy based classification scheme for land applications of polarimetric sar," *IEEE Trans. on Geoscience and Remote Sensing*, vol. 35, pp. 68–78, January 1997.

[107] G. Nesti, A. J. Sieber, G. de Grandi, J. Fortuny, and E. Ohlmer, "Recent advances at the European Microwave Signature Laboratory," in *SPIE, Microwave Instrumentation and Satellite Photogrammetry for Remote Sensing of the Earth* (J. B. Lurie, ed.), Roma, Italy, SPIE, vol. 2313, pp. 56–67, 1994.

[108] A. Franchois, R. Lang, Y. Piñeiro, and R. H. Lang, "Complex permittivity measurements of two conifers," *IEEE Trans. on Geoscience and Remote Sensing*, vol. 36, pp. 1384–1395, September 1998.

[109] S. R. Cloude, J. Fortuny, J. M. López-Sánchez, and A. J. Sieber, "Wideband polarimetric radar inversion studies for vegetation layers," *IEEE Trans. on Geoscience and Remote Sensing*, vol. 37, pp. 2430–2441, September 1999.

[110] E. Mougin, A. Lopes, M. A. Karam, and A. K. Fung, "Effect of tree structure on X band microwave signature of conifers," *IEEE Trans. on Geoscience and Remote Sensing*, vol. 31, pp. 655–667, May 1993.

[111] D. J. Daniels, *Surface Penetrating Radar*. London, UK: IEE Press, 1996.

[112] D. J. Daniels, D. J. Gunton, and H. F. Scott, "Introduction to subsurface radar," *Proc. IEE Pt. F*, vol. 135, pp. 278–320, 1988.

[113] C. E. Baum, *Detection and Identification of Visually Obscured Targets*. Philadelphia, USA: Taylor and Francis, 1999.

[114] L. Peters, Jr., J. D. Daniels, and J. D. Young, "Ground penetrating radar as a subsurface environmental sensing tool," *Proceedings of the IEEE*, vol. 82, pp. 1802–1822, December 1994.

[115] L. C. Chan, D. L. Moffatt, and L. Peters, "A characterization of subsurface radar targets," *Proceedings of the IEEE*, vol. 67, pp. 991–1000, July 1979.

[116] S. Roy, T. Kim, R. S. Berkowitz, and D. Carlson, "Subsurface radar for detection of buried targets," in *Proc. of the IEEE International Radar Conference*, Arlington (VA), IEEE, pp. 129–133, 1990.

[117] T. Ozdemir, S. Roy, and R. Berkowitz, "Imaging of shallow subsurface objects: An experimental investigation," *IEEE Trans. on Geoscience and Remote Sensing*, vol. 30, pp. 472–481, May 1992.

[118] J. I. Halman, K. A. Shubert, and G. T. Ruck, "SAR processing of ground-penetrating radar data for buried UXO detection: Results from a surface-based system," *IEEE Trans. on Antennas and Propagation*, vol. 46, pp. 1023–1027, July 1998.

[119] S. Vitebskiy, L. Carin, M. A. Ressler, and F. H. Le, "Ultra-wideband short-pulse ground-penetrating radar: Simulation and measurement," *IEEE Trans. on Geoscience and Remote Sensing*, vol. 35, pp. 762–772, May 1997.

[120] D. Wong and L. Carin, "Analysis and processing of ultra wideband SAR imagery for buried landmine detection," *IEEE Trans. on Antennas and Propagation*, vol. 46, pp. 1747–1748, November 1998.

[121] A. J. Sieber, ed., *Proceedings of the Demining Technology, International Exhibition, Workshop and Training Courses*, Ispra, Italy, JRC-EC, September 1998. EUR 18682 EN.

[122] N. Geng and L. Carin, "Short-pulse electromagnetic scattering from arbitrarily oriented subsurface ordnance," *IEEE Trans. on Geoscience and Remote Sensing*, vol. 37, pp. 2111–2113, July 1999.

[123] N. Geng and L. Carin, "Wideband electromagnetic scattering from a dielectric body of revolution buried in a layered lossy dispersive medium," *IEEE Trans. on Antennas and Propagation*, vol. 47, pp. 610–619, April 1999.

[124] N. Geng, D. R. Jackson, and L. Carin, "On the resonances of a dielectric BOR buried in a dispersive layered medium," *IEEE Trans. on Antennas and Propagation*, vol. 47, pp. 1305–1313, August 1999.

[125] N. Geng, A. Sullivan, and L. Carin, "Multilevel fast-multipole algorithm for scattering from conducting targets above or embedded in a lossy half space," *IEEE Trans. on Geoscience and Remote Sensing*, vol. 38, pp. 1561–1573, July 2000.

[126] T. J. Cui, W. Wiesbeck, and A. Herschlein, "Electromagnetic scattering by multiple three-dimensional scatterers buried under multilayered media. I. Theory," *IEEE Trans. on Geoscience and Remote Sensing*, vol. 36, pp. 526–534, March 1998.

[127] T. J. Cui, W. Wiesbeck, and A. Herschlein, "Electromagnetic scattering by multiple three-dimensional scatterers buried under multilayered media. II. Numerical implementations and results," *IEEE Trans. on Geoscience and Remote Sensing*, vol. 36, pp. 535–546, March 1998.

[128] T. J. Cui and W. C. Chew, "Fast algorithm for electromagnetic scattering by buried conducting plates of large size," *IEEE Trans. on Antennas and Propagation*, vol. 47, pp. 1116–1121, June 1999.

[129] T. J. Cui and W. C. Chew, "Fast algorithm for electromagnetic scattering by buried 3-D dielectric objects of large size," *IEEE Trans. on Geoscience and Remote Sensing*, vol. 37, pp. 2597–2608, September 1999.

[130] C. A. Balanis, *Advanced Engineering Electromagnetics*. New York, USA: John Wiley and Sons, 1989.

[131] J. A. Stratton, *Electromagnetic Theory*. New York, USA: McGraw-Hill, 1941.

[132] A. von Hippel, *Dielectric Materials and Applications*. Norwood (MA), USA: Artech House, 2nd edition ed., 1995.

Curriculum Vitae

Personal Data

Date of Birth:	December 30th, 1964
Place of Birth:	Tarragona, Spain
Marital Status:	Married (2 children)
Citizenship:	Spanish

Education

1978–1981	La Romànica High School, Barcelona, Spain
1982–1987	Telecommunications Engineering Degree, Polytechnic University of Catalonia, Barcelona, Spain

Professional Experience

1988–1989	Research assistant at the Signal Theory and Communications Department, Polytechnic University of Catalonia
1990–1991	Research assistant at the RF Systems Division, European Space and Technology Center, European Space Agency, The Netherlands
1992	Payload engineer at the Satellite Control Center of Hispasat, Spain
Since 1993	Scientific officer at the Humanitarian Security Unit, Institute for the Protection and Security of the Citizen, DG Joint Research Centre of the European Commission, Ispra, Italy